

RESTORING SENSATION OF GRAVITOINERTIAL
ACCELERATION THROUGH PROSTHETIC STIMULATION OF
THE UTRICLE AND SACCCULE

by
Kristin N. Hageman

A dissertation submitted to Johns Hopkins University in conformity
with the requirements for the degree of Doctor of Philosophy

Baltimore, Maryland
December, 2017

Abstract

Individuals with bilateral vestibular hypofunction suffer reduced quality of life due to loss of postural and ocular reflexes essential to maintaining balance and visual acuity during head movements. Vestibular stimulation has demonstrated success in restoring sensation of angular head rotations using electrical stimulation of the semi-circular canals (SCCs). Efforts toward utricle and saccule stimulation to restore sensation of gravito-inertial acceleration have been limited due to the complexity of the otolith end organs and otolith-ocular reflexes (OORs). Four key pieces of technology were developed to extend prosthetic stimulation to the utricle and saccule: a low-noise scleral coil system to record binocular 3D eye movements; a motion platform control system for automated presentation of rotational and translational stimuli; custom electrode arrays with fifty contacts targeting the SCCs, utricle and saccule; and a general-purpose neuroelectronic stimulator for vestibular and other neuromodulation applications.

Using these new technologies, OORs were first characterized in six chinchillas to establish OOR norms during translations and static tilts. Results led to creation of a model that infers the axis of head tilt from measured binocular eye movements and thereby provides a context and means to assess the selectivity of prosthetic utricle and saccule stimulation. The model confirms the expectation that excitation of the left utricle and saccule primarily encodes tilts that bring the left ear down.

Three of the chinchillas were implanted with electrode arrays in the left ear. Step changes in pulse rate were delivered to utricle and saccule electrodes near the maculae while measuring 3D binocular eye movements with the animal stationary in darkness. These stimuli elicited sustained ocular counter-roll responses that increased in magnitude as pulse rate or amplitude increased. Bipolar stimulation via neighboring electrodes elicited slow-rising or delayed onset of ocular counter-rolls (consistent with normal translational OOR low-pass filter behavior). Two chinchillas showed different direction of electrically-evoked ocular counter-roll between utricle versus saccule

stimulation. Only near-neighbor bipolar electrode combinations elicited eye responses compensatory for tilts other than the ‘usual’ left ear down, suggesting the need for distributing multiple bipolar electrode pairs across the maculae to achieve selective stimulation and restore 3D sensation of gravito-inertial acceleration.

Primary reader: Charles C. Della Santina, PhD, MD

Secondary reader: Gene Y. Fridman, PhD

*To my boyfriend, Mark, for keeping me balanced
through every twist and turn of this journey.*

Acknowledgements

First and foremost, I would like to thank to my advisor, Dr. Charley Della Santina, who always went above and beyond as my teacher, mentor, and friend. Your encouragement through every surgery, every bug in the code, and every experiment helped me tackle all of the challenges that came my way. I am truly grateful for your guidance and unwavering support through these years. To Dr. Gene Fridman, who taught me the art of debugging a system, whether it was figuring out the broken Lasker system, or helping me navigate the MVP's firmware design; thank you for your engineering guidance throughout my PhD. To Dr. Mark Shelhamer and Dr. Nitish Thakor, thank you for all of your time and advice as part of my thesis committee.

I would like to thank my many collaborators, who truly made this project possible. Dr. Angela Tooker, Dr. Satinderpall Pannu, Dr. Vanessa Tolosa, Dr. Sarah Felix, and Dr. Razi Haque from Lawrence Livermore National Labs, thank you for your assistance in electrode design and fabrication which was absolutely invaluable to my project. To Dr. Zaven Kalayjian, Dr. Philippe Pouliquen and Dr. Andreas Andreou from the Johns Hopkins Electrical and Computer Engineering Department, thank you for all your hard work with the ASIC design. And to Dr. Francisco Tejada, thank you for working with me in my PhD infancy to teach me the inner workings of ASIC testing. For Kai Yuen Lim and Dr. Xiaoqin Wang, thank you for the opportunity to adapt our circuitry for applications beyond my dissertation, it taught me valuable skills that will continue to assist me in my future career. I would also like to thank Dr. Taek-Soo Lee and Dr. Ben Tsui for all of their assistance with the microCT scans of my specimens.

Thank you to all the members of the Vestibular NeuroEngineering Lab, who have become my second family over the years. To Meg Chow, for coming in and taking on anything and everything that I threw her way. Your help and friendship were truly instrumental in my PhD and I couldn't wish for anyone better to carry on my dissertation work. To Peter Boutros, for always lending a

hand when needed and for bouncing around ideas when data analysis got messy. To Kelly Lane, for being the best “lab mom” any grad student could ever ask for. Thank you for assisting me with your cat-like reflexes when chinchillas got feisty and for always keeping me young with another round or two of margaritas. To Dale Roberts, for being my walking, talking ‘Art of Electronics’ book over the years, your mentorship has taught me so much. I can only hope to someday master the art of tinkering as you have. To Dr. Chenkai Dai and Dr. Pengyu Ren, thank you both for your help with animal surgeries and experiments. To Dr. Mohammed Lehar, thank you for helping at a moment’s notice whenever solutions were needed. I would like to thank Lani Swarthout for being my sole fellow female in the lab when I joined, and to Nicolas Valentin and Mehdi Rahman for answering my incessant questions when I was the new one in lab. And to the latest newbies, Brian Morris and Andrianna Ayiotis, thank you for joining the VNEL family to carry on the amazing work of the lab.

Last but not least, to my friends and family, your immense support has helped me surmount every hurdle over the years. To my closest friend, Katy, thank you for cheering me on at every step of the way. To my boyfriend Mark, who made it through six and a half years of long distance with me, I am truly grateful for your love and support through this journey. Thank you for listening to me go on and on and on about chinchilla this and chinchilla that, and thank you for riding this roller coaster of a PhD with me. And finally, to my family, words cannot express how much you all mean to me. To my four siblings, my best friends, how you all rally to support and encourage me means more than you will ever know. And to my parents, my most dependable cheerleaders through life. The foundation you built for me has gotten me to where I am today and I am so grateful for your constant, unwavering love and support.

The research reported in this dissertation was supported by the National Institute on Deafness and Other Communication Disorders of the National Institutes of Health under Award Number R01DC009255, R01DC013536. 2T32DC000023-31 through the Johns Hopkins Center for Hearing and Balance, and R01DC014503. Polyimide microelectrode arrays were designed and fabricated

with funding from NIDCD contract Y1-DC-8002-01 and under the auspices of the U.S. Department of Energy by the Lawrence Livermore National Laboratory, Contract number DE-AC52-07NA27344.

Table of Contents

Abstract.....	ii
Acknowledgements	v
Table of Contents	viii
List of Tables	xi
List of Figures.....	xii
Chapter 1 Introduction.....	1
1.1 Significance	1
1.2 Background.....	2
1.2.1 Vestibular System Anatomy and Physiology.....	2
1.2.2 Bilateral Vestibular Hypofunction	4
1.2.3 Restorative Therapy Options	5
1.2.4 Semicircular Canal Stimulation	5
1.2.5 Utricle and Saccule Stimulation.....	12
1.3 General Methods.....	13
Chapter 2 Technology Development	15
2.1 Eye Movement Measurement - Scleral Coil System	15
2.1.1 Introduction.....	15
2.1.2 Methods.....	18
2.1.3 Results.....	22
2.1.4 Discussion.....	28
2.2 Motion Stimulus.....	31
2.2.1 Introduction.....	31
2.2.2 Methods and Results	32
2.2.3 Discussion.....	35
2.3 Electrode Design.....	36
2.3.1 Introduction.....	36
2.3.2 Methods and Results	37
2.3.3 Discussion.....	38
2.4 Prosthesis Development: Hardware, Firmware, and Software	40
2.4.1 Introduction.....	40
2.4.2 Methods and Results	42
2.4.3 Discussion.....	61
Chapter 3 Normal 3D Binocular Otolith Ocular Reflexes in the Chinchilla	65

3.1 Introduction.....	65
3.2 Methods	67
3.2.1 Surgical Methods	67
3.2.2 Eye Movement Recording	68
3.2.3 Motion Stimulus.....	69
3.2.4 Data Analysis	71
3.3 Results.....	72
3.3.1 Angular Vestibulo-Ocular Reflex	72
3.3.2 Ocular Counter-Roll Response to Static Tilts.....	73
3.3.3 Translational VOR Response to Linear Translations.....	79
3.3.4 Tilt-Translation Comparison.....	88
3.3.5 Reverse Model: Predicting Tilt Axis from Ocular Counter-Roll.....	90
Chapter 4 Electrically-Evoked Eye Movements from Utricle and Saccule Stimulation	99
4.1 Introduction.....	99
4.2 Methods	100
4.2.1 Surgery.....	100
4.2.2 Eye Movement Recording	101
4.2.3 Electrical Stimulation Paradigm	102
4.2.4 Data Analysis	103
4.2.5 Imaging of Electrode Placement.....	104
4.3 Results.....	105
4.3.1 Electrically-Evoked Angular VOR	105
4.3.2 Electrically-Evoked Ocular Counter-Roll.....	108
4.3.3 Temporal Dynamics of SCC versus Otolith Stimulation.....	109
4.3.4 Spatial Selectivity of Ocular Response from Otolith Stimulation	112
4.3.5 Tilt Axis Model Output.....	114
4.4 Discussion.....	117
Chapter 5 Conclusions.....	122
5.1 Implications and Limitations	122
5.2 Future Directions	125
5.3 Conclusions.....	126
Chapter 6 Appendix.....	128
6.1 Toward a General Purpose Stimulator: Cochlear Stimulation	128
6.2 Normal Otolith-Ocular Reflex Model Parameters	129
6.3 Animal Data Files Included in Figures	131

Chapter 7 References.....	136
Curriculum Vitae.....	148

List of Tables

Table 1. A summary of the scleral coil system characteristics.	23
Table 2. Results measured from the ASIC-Neural Interface.	49
Table 3. Frequency and peak acceleration of sinusoidal translations.	71
Table 4. Trends in the ocular counter-roll data grouped by tilt axis.	92
Table 5. Model parameters to predict eye movements from tilt or translation axis.	129
Table 6. Model parameters to predict axis of tilt/translation based on grouped OORs.	130
Table 7. Model parametersto predict tilt axis from binocular eye movements.	130
Table 8. Data files used for creation of figures with chinchilla data.	135

List of Figures

Figure 1. First generation multichannel vestibular prosthesis.	8
Figure 2. Normal and electrically-evoked aVOR in chinchillas.	9
Figure 3. The 2nd generation Multichannel Vestibular Prosthesis	10
Figure 4. Normal and electrically-evoked aVOR in monkeys.	11
Figure 5. Block diagram of the scleral coil system architecture.	20
Figure 6. Voltages recorded at different stages in the scleral coil system.	24
Figure 7. Noise floor comparison of old and new scleral coil systems.	25
Figure 8. Induced voltage of scleral coil in the magnetic fields.	25
Figure 9. Step response of two different scleral coil systems.	26
Figure 10. Homogeneity of the coil system’s magnetic fields.	28
Figure 11. Linearity measurements of demodulated scleral coil signals.	29
Figure 12. Image of the motion platform and scleral coil system.	32
Figure 13. Graphical user interface for motion platform control.	34
Figure 14. Custom polyimide electrode array design.	37
Figure 15. Cross-sectional view of the microfabrication process for polyimide electrodes.	39
Figure 16. Vestibular prosthesis architecture required for extending the MVP.	40
Figure 17. Design progression of the MVP.	42
Figure 18. New multichannel vestibular prosthesis system design,	43
Figure 19. Pulsatile stimulation from rotations and translations.	44
Figure 20. High voltage current steering schematic for the ASIC-NI.	48
Figure 21. Representative DAC output from one ASIC-NI channel.	49
Figure 22. Current output from ASIC-Neural Interface at varying compliance voltages.	51
Figure 23. Example multipolar stimulation using the ASIC-Neural Interface.	53
Figure 24. Comparison of electrically-evoked eye movements from the MVP2 versus the ASIC-based MVP stimulator circuitry (MVP2A).	57
Figure 25. Gain of electrically-evoked aVOR responses in monkeys using the MVP2 and MVP2A.	58
Figure 26. Hardware of the new MVP system designed for stimulation of the three SCCs and the utricle and saccule.	59
Figure 27. Custom C# graphical user interface (GUI) used to wirelessly program the prosthesis via Bluetooth.	61
Figure 28. Axes of sinusoidal translations for characterization of the 3D translational vestibulo-ocular reflex.	70
Figure 29. Axes of whole-body static tilts.	71
Figure 30. Normal chinchilla angular VOR.	74
Figure 31. Example ocular counter-roll responses recorded during 20° from horizontal tilts.	76
Figure 32. Ocular counter-roll responses recorded from six chinchillas during static tilts.	78
Figure 33. Example binocular tVOR position and velocity traces during translations.	80
Figure 34. Gain and phase of the chinchilla tVOR during lateral and surge translations.	82
Figure 35. Comparison of monkey and chinchilla tVOR frequency response during lateral translation.	83
Figure 36. Translational VOR elicited during translations along axes in the <i>horizontal plane</i>	86
Figure 37. Translational VOR elicited during translations along axes in the <i>coronal plane</i>	87
Figure 38. Translational VOR elicited during translations along axes in the <i>sagittal plane</i>	88

Figure 39. Comparison of tilt versus translation eye movement data.....	91
Figure 40. Model output to predict tilt axis using binocular eye movement data.....	94
Figure 41. The surgical view during the polyimide vestibular electrode implant procedure.....	102
Figure 42. Polyimide electrode array contact numbering scheme.....	104
Figure 43. Post-mortem microCT scans for each of the three implanted chinchillas.....	106
Figure 44. Electrically-evoked aVOR from three chinchillas.....	107
Figure 45. Electrically-evoked ocular counter-roll with stimulation of increasing pulse amplitude.	108
Figure 46. Electrically-evoked ocular counter-roll with stimulation of increasing pulse rate.....	109
Figure 47. Electrically-evoked ocular counter-roll using different reference electrodes.....	111
Figure 48. Analysis of electrically-evoked ocular counter roll rise time grouped by reference type.	112
Figure 49. All results from utricle and saccule pulse train stimulation for the three chinchillas.	115
Figure 50. Spatial selectivity of utricle and saccule stimulation.....	116
Figure 51. Model output to infer electrically-encoded tilt axis from electrically-evoked eye movements.....	117

Chapter 1 Introduction

1.1 Significance

The vestibular system provides sensation of *rotational* and *translational* head movements to drive essential reflexes that help maintain stable vision, a sense of balance, steady gait, and spatial orientation. Individuals with bilateral vestibular loss suffer blurry vision, illusory movement of the visual field and loss of balance, all leading to a significantly decreased quality of life. An analysis of 2008 US National Health Interview Survey data found over 64,000 Americans reported avoidance of social activities, reduced ability to drive, a 31-fold increase in the likelihood of falling, and an increased socio-economic burden, all due to symptoms of bilateral vestibular loss [1,2].

Research toward a multichannel vestibular prosthesis intended to treat individuals disabled by vestibular loss has focused on restoring sensation of *rotational* motion and the *angular* vestibulo-ocular reflex via stimulation of the semicircular canals. In contrast, prosthetic stimulation of the utricle and saccule, which normally sense *translational* accelerations and changes in head orientation (gravito-inertial acceleration), has been relatively unexplored, in part because of the significant technical challenges posed by their anatomy. Extending this stimulation paradigm to also target the utricle and saccule is necessary to develop a vestibular prosthesis that restores not only sensation of angular head rotation but also changes to gravito-inertial acceleration.

The research in this dissertation first focused on technical development to create a system to extend the prosthesis to electrically stimulate both the rotational and translational end organs of the vestibular system. Experiments using that system then explored the capability of selectively stimulating the utricle and saccule in chinchillas, yielding results that can advance both the science of vestibular physiology and translation of that knowledge toward clinical application. The research described in this dissertation is a first step toward a more *complete* vestibular prosthesis to help restore the utricular and saccular reflexes in individuals with profound vestibular loss.

1.2 Background

1.2.1 Vestibular System Anatomy and Physiology

The vestibular system comprises two classes of motion sensors in each ear: (1) three semicircular canals (SCCs: anterior, posterior and horizontal) and (2) two otoconial, or otolith end organs (the utricle and saccule). Input from the vestibular labyrinths' inertial sensors drives ocular (vestibulo-ocular reflex, VOR), postural and autonomic reflexes that help maintain stable vision, posture, spatial perception and cerebral perfusion during head motion and reorientation encountered during every day activities [3].

Vestibular sensation relies on mechano-transduction of head movements via hair cells, named for the bundle of hair-like structures called stereocilia that protrude from each hair cell's apical membrane surface. Deflection of the mechano-sensitive stereocilia bundles toward the tallest stereocilium (the kinocilium) leads to cellular depolarization (excitation) and an increase in the firing rate of primary afferent neurons associated with that hair cell. Deflection away from the kinocilium drives cellular hyperpolarization (inhibition) and a decrease in afferent neuron firing rate. When the head is at rest, each afferent neuron discharges spontaneously at a nonzero mean baseline firing rate. Hair cell depolarization and hyperpolarization increase or decrease the neuronal firing rate around that baseline rate to encode head movements sensed by the five vestibular end organs in each labyrinth [3, 4].

The SCCs encode rotational head movements and drive compensatory eye movements with equal and opposite direction. The three mutually orthogonal, fluid-filled SCCs in one ear form coplanar pairs with the SCCs in the opposite ear: left-anterior/right-posterior (LARP), right-anterior/left-posterior (RALP) and left-horizontal/right-horizontal (LHRH). During a head rotation about the axis of a given SCC, the hair cell stereocilia in that SCC's ampulla are deflected due to inertial loading by the fluid in the canal. This deflection induces changes in firing rates of the afferent neurons in the SCC's *ampullary nerve*. Hair cells on a SCC's *crista* (neuro-epithelium) are all oriented in the same direction. Rotation about a given axis therefore causes afferent excitation

in one ear's SCC and inhibition in the other ear's coplanar SCC. The difference between those complementary inputs drives a compensatory *angular* VOR (aVOR). The SCCs decompose 3D head rotations into vector components about the LARP, RALP and LHRH axes [3,4].

The utricle and saccule sense linear accelerations and drive the *translational* VOR (tVOR) and sense changes in the gravitoinertial acceleration vector (GIA, the summed vector of gravity and translational accelerations acting on the head) during head tilts to drive the compensatory ocular counter-roll response. The term tVOR will be used to indicate the resultant eye movement due to linear translations. Ocular counter-roll will signify eye movement responses to whole-body reorientation due to a static tilt; it is assumed that the long duration of the tilt minimizes any persistent aVOR effects from the initial head rotation to reach the tilt position. The term OOR (otolith-ocular reflex) will be used to denote both the tVOR and ocular counter-roll.

The utricular macula (neuro-epithelium) lies approximately in the horizontal SCC plane, sensing linear forces along any translation axis in that 2D plane. The saccular macula is approximately oriented in a parasagittal plane and encodes components of gravitoinertial acceleration in that plane. The hair cells of the utricle and saccule are sensitive to shear forces imparted on hair cell stereocilia by an overlying composite mass of calcium carbonate crystals in a gelatinous medium called the otoconial membrane. During linear accelerations or changes in the GIA during static head tilt, loading by this mass causes displacement of the otoconial membrane, deflecting stereocilia of the hair cells and driving changes in firing rates of the macular nerve afferents, which subsequently drive OOR eye movements [5]. The hair cells across each macula are not uniformly oriented, so a single head movement elicits a complex pattern of excitation and inhibition in each macular nerve [3].

In addition to canal-mediated aVOR and otolith-mediated OOR responses, oculomotor reflexes dependent on visual feedback, such as optokinetic nystagmus (eye response to optic flow of a visual scene) and smooth pursuit (tracking an image to keep it fixed on the retina), also assist in maintaining visual acuity. However, these vision-dependent responses have dynamic limitations

that make them inadequate to stabilize the eyes during quick head movements. The long latency of these reflexes (~100 ms) causes them to be insufficient for head movements at modestly high velocities and frequencies (such as those encountered during walking, running and driving). The vestibular system drives aVOR responses with only a ~7 ms latency to maintain visual acuity during high acceleration, high velocity, and high frequency head rotations [6]. In contrast, the response dynamics of the OOR show a low-pass filter behavior, with highest gains (eye position / head acceleration) at very low frequencies and static tilts [7]. The differences in dynamics between the various systems illustrate that sensory systems operate at an optimal range of frequencies, so failure of one system can be partly compensated for by supporting systems, but are not sufficient to fully overcome the drop in performance caused by the loss.

1.2.2 Bilateral Vestibular Hypofunction

Bilateral vestibular hypofunction (BVH) causes a significantly reduced quality of life due to the failure of the vestibular reflexes. Loss of the VOR results in decreased visual acuity and blurred vision. While the aVOR compensates for quick head *rotations*, individuals also rely on the tVOR to maintain stable visual during linear *translations*. Additionally, utricle and saccule input drive perception of earth vertical, provide input for proper orientation in space, especially in situations with limited visual input, and drive postural reflexes to maintain balance. Individuals with BVH no longer have vestibular input to drive these reflexes, and thus suffer from decreased visual acuity, loss of balance, and lack of spatial orientation.

One of the most common causes of BVH in adults is ototoxic injury due to aminoglycoside antibiotic treatment; others include Ménière's disease, genetic abnormalities, labyrinthitis and trauma [1,2,8]. As reported in Ward, et al., responses from the US National Health Interview Survey indicate 28 per 100,000 adults in the United States suffer from BVH related symptoms. Of the individuals with BVH, 55% missed work or school, 44% had to change their driving habits, 56% decreased participation in social activities, and 58% reported difficulty with daily life activities,

and a 31-fold increase in the risk of fall, all due to their BVH symptoms [1]. In addition to reduced quality of life, the economic burden for BVH averaged \$13,019 per individual [2].

1.2.3 Restorative Therapy Options

There is currently no treatment to correct chronic BVH, although rehabilitation exercises often help BVH patients better compensate by using visual and proprioceptive cues [1,2,8,9]. These cues are especially helpful in assisting with ocular and postural reflexes during active movements, but they are not fast enough to fully compensate for the VOR during quick, unpredictable movements. Research on using sensory substitution methods to encode balance have used sound [10,11], tactile feedback to the torso [12,13], and electrical stimulation of the tongue [14,15]. Although sensory substitution showed some improvement in posture and balance in patients with BVH, it is not fast enough to substitute for the VOR and does not have the 3D spatial ability of the VOR.

1.2.4 Semicircular Canal Stimulation

Electrical stimulation of the SCCs has been studied and implemented as a promising approach to restore the aVOR. Vestibular prosthesis development has so far focused on the study of the VOR instead of the postural and autonomic reflexes that are also driven by the vestibular system. Several reasons account for this focus on the VOR. First, postural and autonomic responses to changes of vestibular input can be difficult to study in rodents and other animal models, which require extensive training and are generally poor models of human bipedal posture and gait. Second, the VOR is reflexive and occurs even in darkness, eliminating the need for animal training, active animal cooperation, and visual stimuli. Third, the eye has low inertia and is limited to rotational movements about a head-fixed center of rotation within the ocular orbit, obviating consideration of the complex mechanical aspects of limb and trunk movement. Fourth, eye movements can be measured in 3D with high temporal and angular resolution. Fifth, mathematic representations of 3D rotational kinematics are well established and uniquely determine eye angular position, making eye movement analysis simpler to interpret than postural movements [16]. Finally, electrically-

evoked eye movements in response to SCC stimulation have been described and quantified in numerous studies since the initial work by Cohen, Suzuki *et al.* in the 1960s [17–21] inspired the idea of using electrical stimulation not only as a way to study normal physiology but also as a possible treatment for loss of SCC function. That body of SCC stimulation literature has revealed that the SCC-mediated aVOR is conjugate (i.e., approximately the same for both eyes) and can be reasonably approximated as a one-to-one mapping from a 3D head rotational velocity stimulus to an approximately equal and opposite 3D eye rotational velocity response. This mapping is approximately linear and invertible [22]. Consequently, one can readily invert that mapping to infer the pattern of ampullary nerve excitation (and the corresponding head rotation) that occurred during natural or prosthetic stimulation to elicit an observed eye movement response.

Gong, Merfeld, Lewis *et al.* made the first head-mounted, single-channel vestibular prosthesis. It delivered biphasic pulses to one SCC ampullary nerve of guinea pigs [23,24] and later monkeys [25–28]. That device used a motion sensor to modulate the pulse frequency of stimuli based on sensed angular head velocity, demonstrating the ability to partially restore eye movement reflexes during single-axis head movements with electrical stimulation. Working along similar lines, the Johns Hopkins Vestibular NeuroEngineering Lab developed a multichannel vestibular prosthesis (MVP) to target all three of the SCCs and extensively characterized its performance in chinchillas (Section 1.2.4.1) [22,29,30] and rhesus monkeys (Section 1.2.4.2) [31–34]. SCC stimulation has since been extended to three different first-in-human trials [35–37] conducted by three different groups. Those on-going studies are discussed in Section 1.2.4.3.

1.2.4.1 Normal and Electrically-Evoked Chinchilla Angular VOR

Normal chinchilla eye movements were characterized by Migliaccio *et al.* to first determine whether chinchillas, which have laterally-oriented eyes without retinal foveae, can be a useful model for the VOR of the frontal-eyed, foveate monkeys and humans [38]. That study quantified eye movements from 11 chinchillas in darkness during static tilts, sinusoidal rotations at frequencies of 0.05-15 Hz, ranging in amplitude from 20-100°/s, and acceleration steps up to 3000

deg/s². Results demonstrate conjugate, compensatory aVOR responses where gain (eye rotational velocity / head rotational velocity) was 0.39 ± 0.08 for peak head velocity 20°/s at 1Hz and fell for frequencies below 0.1 Hz. Equivalent gains were reported for rotations about the three SCC axes and responses were approximately isotropic. Additionally, the static tilt response compensated for the direction of the tilt, similar to that seen in primates and humans. In conclusion, this study showed that the chinchilla aVOR was comparable to primate and human with regard to conjugacy, frequency and temporal responses, but with lower gain and greater isotropy [38]. Despite these quantitative differences, the chinchilla VOR is qualitatively similar enough to humans that chinchillas are an appropriate *in vivo* animal model for vestibular implant development.

The Johns Hopkins MVP was designed to mimic the normal encoding scheme of the vestibular nerve and modulate pulse frequency and/or amplitude around a nonzero baseline stimulation rate to encode 3D head rotational velocity. The sensed rotational motion is decomposed about each axis of rotation to determine the pulse frequency of modulated pulse trains delivered to each SCC. The first version of the MVP (MVP1 [29]), shown in Figure 1 used three single axis gyroscopes to sense 3D head velocity. The prosthesis microcontroller employed a sigmoidal map, shown in Figure 1A, to convert head velocity to pulse rate (similar to natural encoding of head movements [5,39,40]). Each pulse was delivered via an electrodes implanted in each SCC. The electrodes were created from a twisted pair of 75 μ m diameter Pt/Ir wire (AS169-40, Cooner Wire, Chatsworth, CA) stripped 0.2 mm. The change in instantaneous pulse rate due to head velocity is pictured in Figure 1C. Figure 1B and C were adapted from Della Santina et al. [29].

Responses to rotational stimuli and prosthetic stimuli recorded from a chinchilla are shown in Figure 2, adapted from Della Santina et al. [29]. The first column illustrates normal chinchilla aVOR of the left and right eye during 2 Hz, 50°/s sinusoidal rotation completed in the dark. The average gain (eye velocity/head velocity) was approximately 0.43 ± 0.28 with the eyes moving primarily about the axis of rotation. After ablating bilateral vestibular function with gentamicin (second column), the same rotations elicited no eye movements. Finally, after the prosthesis was

turned on, the animal was rotated again with the prosthesis encoding head velocity to a sinusoidally modulated pulse rate delivered to the appropriate SCC. This stimulation elicited partial restoration of the aVOR, with the maximum component of eye movement about the same axis of the head rotation and SCC stimulation. Misalignment of the axis of eye rotation can be seen, but further studies in chinchillas developed methods to prove linearity and superposition hold for the aVOR, and thus a 3D transformation matrix can be used to better align electrically-evoked eye movements to the appropriate SCC axis [22]. Additional studies optimized stimulation parameters [41,42], showed improved locomotion with electrical stimulation [43], and minimized misalignment with chronic stimulation [30].

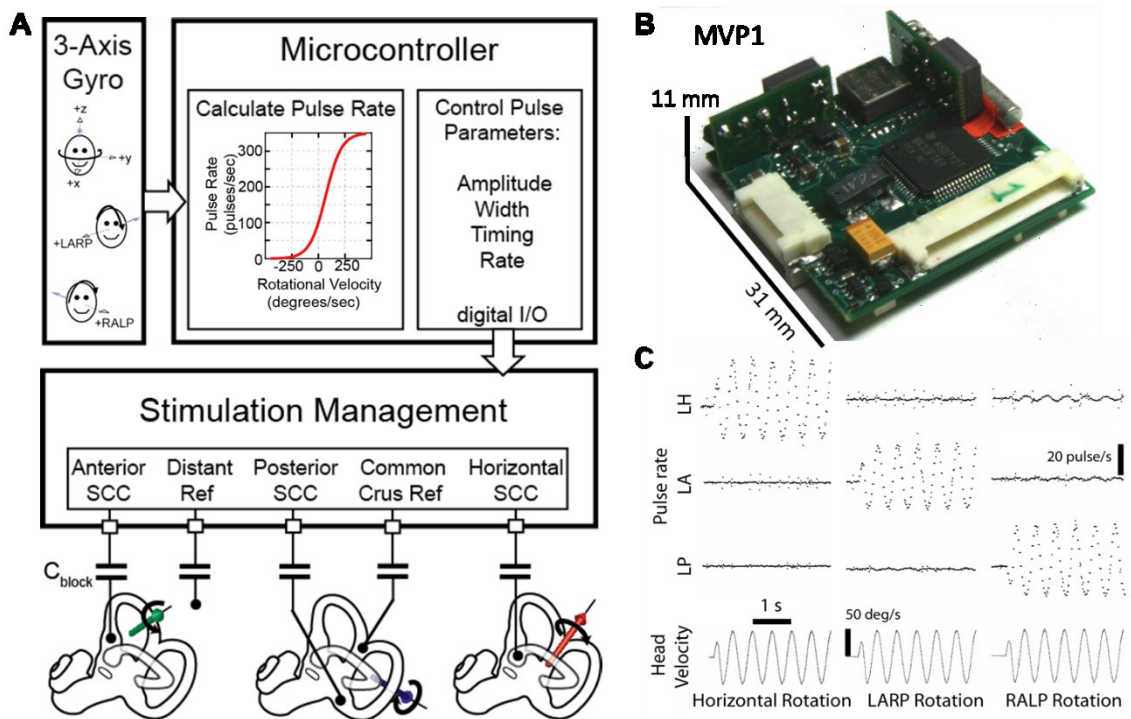


Figure 1. First generation multichannel vestibular prosthesis. Panel A illustrates the basic architecture for the MVP design. A gyroscope sensed 3D rotational head velocities which are converted to pulse rate using a sigmoidal map in the microcontroller. The microcontroller sends all pulse information to the stimulation management circuitry which delivers the pulsatile stimulation to each SCC via coupling capacitors. The MVP1, pictured in B, uses three single axis gyroscopes for sensing head rotations. Changes in pulse rate delivered to each SCC (left horizontal=LH, left anterior=LA, left posterior=LP) due to a rotation about that SCC's axis are shown in C, where instantaneous pulse frequency is shown with dots in the top three rows.

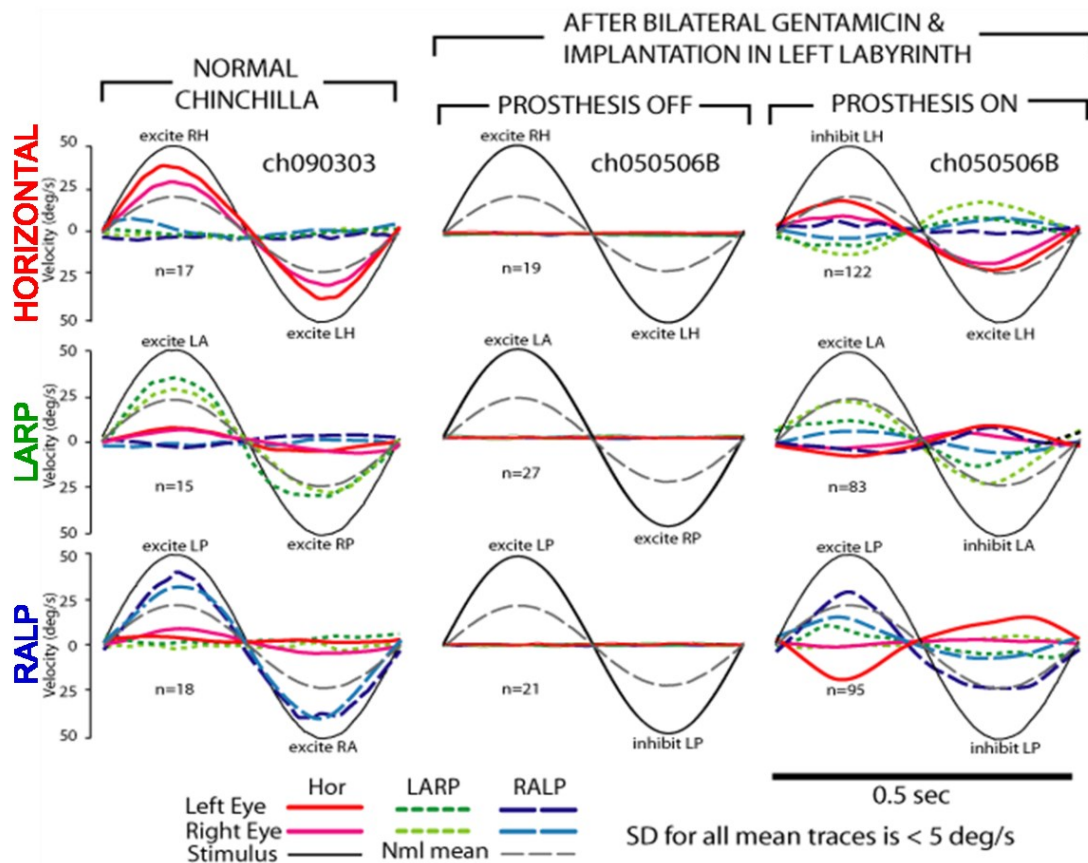


Figure 2. Normal and electrically-evoked aVOR in chinchillas. Mean head rotation and eye rotations of a normal chinchilla during a 2 Hz, 50°/s head rotation (in the dark) about the horizontal (top), LARP (middle), and RALP (bottom) axes in the first column. The rotation stimulus is shown in black, with the right and left eye velocities during the rotation as indicated. Head or eye velocity are inverted for visual comparison with the stimulus. The average across all 5 normal animals is shown in gray in the first column. The second column, showed no eye movements elicited during a rotation about the three SCC axes after bilateral gentamicin treatment. The final column illustrates the response after electrode implantation and 3.5 hours of baseline rate adaptation. The animal was rotated about each SCC axis while the prosthesis encoded the motion and stimulated the appropriate SCC. This image was adapted from [29].

1.2.4.2 Non-Human Primate Electrically-Evoked Angular VOR

Based on the promising results from electrically-evoked aVOR in chinchillas, this work was extended to Rhesus monkeys. A new prosthesis was designed by Chiang et al. to minimize circuitry size, reduce the power consumption, and interface with a new electrode array, all shown in Figure 3, adapted from [32]. This 2nd generation MVP (MVP2) elicited similar restoration of the aVOR in monkeys, Figure 4 with electrically-evoked eye movements primarily aligned with the axis of the

stimulated SCC. The asymmetry (larger amplitudes in the excitatory eye movement direction than the inhibitory) is common based on the limitation of modulation around the ~100 pulses per second (pps) baseline rate. Continued studies by Dai, et al. showed further aVOR restoration [31]. Misalignment was minimized with adaptation to chronic stimulation [33], stimulation parameters were optimized [44], and Dai et al. reported small, insignificant changes in hearing were caused by the vestibular electrode implant in monkeys [34]. These findings show that SCC stimulation can restore aVOR in monkeys and thus became a promising path toward human vestibular stimulation.

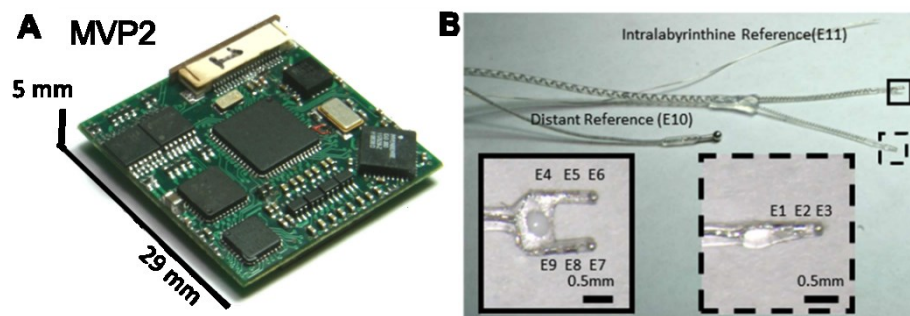


Figure 3. The 2nd generation Multichannel Vestibular Prosthesis (MVP2, shown in A). This 2nd generation prosthesis was developed with the same general architecture as pictured in Figure 1A, but with updated technologies. The custom designed electrode array (B) offered three electrode contacts per SCC (E1-E3 for the posterior SCC, and E4-E6 and E7-E9 for either the horizontal or anterior SCCs). During experiments, the best of the three electrodes per SCC was used for stimulation. Images adapted from Chiang et al. [32].

1.2.4.3 Human Electrically-Evoked Angular VOR

Vestibular stimulation in humans has been studied by groups from University of Washington, University of Geneva/Maastricht University, and Johns Hopkins University. Each study used a stimulator adapted from various cochlear implants with custom electrode arrays. Results from Washington and Geneva/Maastricht's acute vestibular stimulation experiments showed modest electrically-evoked eye movements elicited from stimulation of the three SCCs. The eye movements reported by these groups were recorded in 2D, and thus there is difficulty in ascertaining the alignment with the SCCs [35,36].

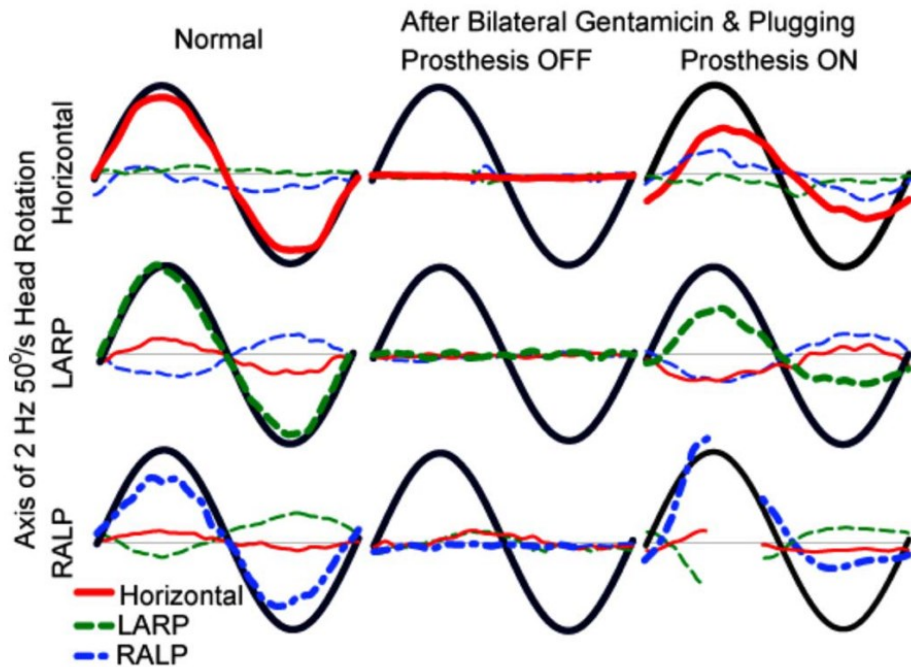


Figure 4. Normal and electrically-evoked aVOR in monkeys. Results of normal and electrically-evoked angular VOR during 2 Hz, peak 50°/s sinusoidal rotations about the horizontal SCC (top row), the LARP axis (middle row), and RALP axis (bottom row). The first column shows normal results as the animal is rotated (black line), where the major component of eye velocity is compensatory for the axis of rotation. After bilateral gentamicin and canal plugging to eliminate all SCC function, the same rotations showed no aVOR response (2nd column). And finally, after the prosthesis was activated and the monkey adapted to baseline rate stimulation, partial restoration of the aVOR was achieved (3rd column). Image adapted from Chiang et al. [32].

Based on findings from Valentin et al., a modified cochlear implant approach for vestibular stimulation can elicit promising aVOR results in monkeys [45]. Labyrinth Devices, LLC (Baltimore, MD) developed a Multichannel Vestibular Implant™ (MVI™) in collaboration with MED-EL GmbH (Innsbruck, Austria) for an ongoing human clinical trial at Johns Hopkins University. This device provides continuous stimulation to all three SCCs based on measured head motion. Results from the first three implanted subjects showed compensation to baseline stimulation within ~ 35 minutes of device activation. The electrically-evoked aVOR data reported for that study to date suggests that (1) the MVI™ successfully activates VOR neural pathways to elicit eye movements and (2) central nervous system compensation to prosthetic stimuli result in a

small but systematic and significant increase of eye movement amplitudes over the first 8 weeks of chronic MVI™ stimulation [37,46].

1.2.5 Utricle and Saccule Stimulation

Vestibular prosthesis research has so far mainly focused on electrical stimulation of the SCCs rather than the otolith end organs, because the relationships between 3D head rotational velocity, the normal patterns of activity in SCC hair cells and SCC branches of the vestibular nerves, and the 3D angular VOR (aVOR) eye movements that occur in response to SCC stimulation are all relatively straightforward [17–21]. The relatively simple, approximately one to one mapping from angular head velocity to angular VOR can be reversed by simple reversal of arithmetic sign. Therefore, one can use electrically-evoked eye movements as an assay to determine the pattern of relative ampullary nerve activation or inhibition, which in turn approximates the axis and speed of the head movement that normally elicits the observed eye movement response. The ability to infer an equivalent head movement facilitated optimization of electrode arrays and stimulation parameters to more selectively encode each head movement, as shown in guinea pigs [23,24], chinchillas [22,29,30,41–43], non-human primates [25–28,32,33,44], and humans [35,37,47,48]. Analogously, extension of the vestibular prosthesis to also target the utricle and saccule requires an understanding of otolith-driven 3D eye movements to interpret electrically-evoked otolith-ocular reflexes.

Comparatively little literature exists regarding electrically-evoked 3D OORs. Attempts to selectively stimulate the utricular and saccular nerves by Suzuki *et al.*[49] and Goto *et al.* [50,51] and stimulation of the maculae by Fluor and Mellström [52–54] evoked eye movements in cats, but the eye movements observed in those studies were inconsistent and some were poorly aligned with the orientation of hair cell stereocilia at the presumed stimulation site. Curthoys [55] explored electrical stimulation of the utricular and saccular maculae in guinea pigs with very fine electrodes, expected to result in less current spread and more selective stimulation. However, Curthoys

reported that electrically-evoked OOR responses were always upward or upward and torsional (in reference to the ocular orbit), independent of the location of stimulation on the maculae. Additionally, utricular stimulation in humans was reported to show neural responses during recording of electrically-evoked compound action potentials (eCAPS) and ocular vestibular evoked myogenic potentials (oVEMPs) [56]. These neural response of utricular fibers to stimulation showed the presence of activation but did not investigate the level of specificity that can be achieved with utricular stimulation or the effects on the VOR response. These discrepancies between studies indicate the need for further investigation to clarify whether it is possible to achieve spatially selective and therapeutically effective macular nerve stimulation.

1.3 General Methods

The research of this dissertation was initiated with extensive technical development of systems used throughout all studies to characterize normal OORs in chinchillas and electrically stimulate the utricle and saccule to analyze electrically-evoked OORs. This development included new systems to record eye movements (section 2.1), provide translation and static tilt stimuli (section 2.2), and deliver pulsatile stimulation to the utricle and saccule (sections 2.3 and 2.4).

All experiments were completed in adult, wild-type chinchillas (*Chinchilla lanigera*, 400-650 g) in accordance with a protocol approved by the Johns Hopkins Animal Care and Use Committee, which is accredited by the Association for the Assessment and Accreditation of Laboratory Animal Care, and consistent with European Community Directive 86/609/EEC. Detailed surgical and experimental methods are included in the appropriate chapters for each experiment type (sections 3.2 and 4.2). As a brief summary, each chinchilla was implanted with a head cap/post and scleral eye coils for measuring 3D binocular eye movements. The chinchilla recovered for 10-14 days before beginning collection of normal OOR during linear translations along various 3D axes and static tilts about many axes in the horizontal plane. All normal data were collected with the animal head-fixed, in the dark. After collection and analysis of normal OORs, a second surgery was

completed to implant the left ear with a custom electrode array for stimulation of all three SCCs and the utricle and saccule. After 5-7 days of post-operative recovery, electrically-evoked eye movements were recorded during stimulation of the utricle and saccule while the animal was stationary, in the dark. All eye movements were recorded using custom C and C# software (sections 2.1.2.3, 2.1.2.4), motion platform feedback using custom C# software (section 2.2.2.4), and prosthesis C# software (section 2.4.2.4). All data files were analyzed using custom MATLAB code (sections 3.2.4 and 4.2.4).

Chapter 2 Technology Development

2.1 Eye Movement Measurement - Scleral Coil System

2.1.1 Introduction

Precise and accurate high-speed measurement of three dimensional (3D) eye movements is an essential technique for the study of vestibular and oculomotor reflexes [57], which constitute an important system for the study of sensorimotor integration and central nervous system plasticity. Eye movements are a useful tool for scientists and clinicians, offering insight to the central nervous system and clues to diagnose underlying oculomotor diseases, including vestibular loss [16]. Driven by the need for stable vision, the VOR drives quick eye movements to compensate for head movements with a latency around 7 ms [6]. This low-latency, compensatory relationship between head and eye movements offers a direct method to interpret vestibular sensation and disease and therefore demands a fast, precise and accurate system for measurement of eye movements.

Three methods are commonly used for measurement of eye movements: (1) electrical-oculography (EOG, also called electronystagmography, ENG), (2) video-oculography (VOG, also called video-nystagmography, VNG), and (3) the scleral search coil technique. Each method has strengths and weaknesses for use in clinical and research settings.

EOG uses surface electrodes placed on the face above, below and beside each eye to measure changes in the projection of the corneo-retinal dipole onto the axis of the electrodes [58]. Although this method is simple and noninvasive, it has a low accuracy for measurement of small eye movements due to high noise levels, drift, and artifacts from blinks and facial muscle electromyographic activity. Additionally, eye rotation about the optic axis does not cause a detectable EOG signal, so EOG can only measure eye movements in two dimensions (horizontal and vertical) [58–60].

Technological advancements in image acquisition equipment have increased the use of VOG over the past couple decades [59–70]. The majority of VOG systems track movement of the cornea,

pupil, or landmarks in the iris coloration [60,62,67], corneal reflections and Purkinje images [60,61], or an added eye marker or fluorescent dye [66,70]. In a clinical setting, VOG without an eye marker is common due to its noninvasive nature, and relies on instruction to the patient to keep their eyes open. Additionally, VOG recordings often contain artifacts due to blinking and head-mounted camera slippage during quick head movements. For research labs, VOG can be used as long as the animal is alert and awake with eyes open at all times; however, this can be difficult to do with an animal kept in darkness for vestibular testing, where any eye closure causes loss of data collection. VOG recording in 3D can also be difficult in animals that do not have readily visible iral striations. Markers placed temporarily on the eye's surface or permanent markers implanted beneath the conjunctiva can overcome this problem [66,70,71]; however, closure of the lid obscures the camera's view of the marker, and artifacts from a marker hitting the lid or falling off can limit the duration of experiments and repeatability of experiments.

The “gold standard” scleral search coil method, first described by Robinson in 1963, provides a method for research studies of eye movements with high spatial and temporal resolution [57]. The original system used an alternating magnetic field to induce a voltage in a scleral search coil that moves with the eye. Robinson showed that with two orthogonal alternating magnetic fields operating 90° out of phase with each other, the induced coil voltages can be demodulated with a pair of phase detectors to determine the scleral coil's orientation with respect to the frame coils generating the magnetic fields. With the addition of a second scleral coil, 3D eye movements (horizontal, vertical, and torsional) were recorded [57].

Since Robinson's original description, multiple other groups have developed systems using similar concepts but differing in number of magnetic fields and the analog demodulation method employed [72–74]. A commercially available system (Primelec, D. Florin, Switzerland) creates three magnetic fields alternating at different frequencies and uses two scleral coils to obtain 3D eye movements. In Primelec's system, all demodulation is completed in the digital domain based on

the spectral components of the induced coil current found using real-time Fast Fourier Transform (FFT) [75].

When using scleral coils with animals, pairs of coils can either be temporarily affixed to the surface of the eye or permanently implanted on the sclera beneath the conjunctiva [66,76–83]. Affixing to the surface of the eye is expedient for one-time experiments but suffers from artifacts whenever the coils touch the eye lids. Scleral coil implantation is the technique of choice when repeated experiments demanding high resolution eye movement recording are required. However, design and fabrication of implanted coils requires special attention to the need to withstand the *in vivo* environment without breaking from repeated bending during eye movements. In addition, the surgical implantation procedure can be technically challenging in small rodents [63], in which it is important to avoid extraocular muscle damage and restriction of eye movement by scar tissue. Therefore, we designed new small, robust, implantable scleral coils for use in chinchillas that have proven to last for several months after implantation (detailed below in 2.1.2.1). With careful surgical technique, ocular movement limitations are mitigated. However, the new scleral coils yielded insufficient signal to noise ratio in our existing system (existing scleral coil system detailed in Migliaccio *et al.* [66] which follows the Rimmel design [73]). This prompted the need for a new system to measure eye movements.

The work presented in this section is a new implementation of the scleral coil system concepts driven by the need for high resolution eye movement recordings in repeated experiments. Based on Robinson's foundation [57], we describe a system using three magnetic fields alternating at three different frequencies. Induced voltage in a scleral coil is demodulated in the digital domain using a field programmable gate array (FPGA). The system provides a precise and accurate means to obtain 3D eye movements from small scleral coils required for experiments involving small research animals and offers flexibility to customize, extend, and expand the technology for future experiments.

2.1.2 Methods

This system comprises two major parts: the magnetic field driver circuitry and signal demodulation circuitry, as shown in Figure 5 and can operate with up to twelve connected scleral coils. The system's *field coils* refer to the coil frame itself (seen in Figure 12 in section 2.2.2.1 on top of the motion platform), where each field coil pair, +X/-X (front/back), +Y/-Y (left/right), and +Z/-Z (up/down), are wired in pairs to make up the three orthogonal magnetic fields, X, Y and Z (following the right-hand rule). Each magnetic field oscillates at a unique frequency and induces a voltage on a small, multi-turn scleral coil, where *scleral coil* refers to the implanted coil sutured to sclera used to track the eye movements. The magnitude of each component of frequency of the induced voltage on the scleral coil depends on the coil's orientation with respect to the fields. Voltage from the scleral coil is demodulated to determine the scleral coil orientation. With a set of two coils orthogonally attached to the sclera, the 3D VOR can be recorded and analyzed with 3D rotational kinematics equations as described by Haslwanter and Migliaccio [84,85]. These methods detail the hardware, firmware, and software required for this system in addition to the scleral coil design.

2.1.2.1 Scleral Coil Design

Scleral coils of 3-4 mm diameter were custom made using 20 turns of 42 awg copper magnet wire, resulting in a torus with inner diameter ~ 2 mm, outer diameter ~ 4 mm, and height ~ 1 mm. Two pieces of multistranded stainless steel wire (A-M SystemsTM 793200) were soldered to each end of the magnet wire coil. Stainless steel leads were wrapped once around the perimeter of the copper coil so the point of flexion as the coil moves is purely stainless steel wire, to mitigate chances of magnet wire breaking due to repeated flexing during eye movements. The two stainless steel wires were then tightly twisted to minimize artifacts due to magnetic field flux passing between the leads anywhere other than at the copper coil. After implantation, connectors were soldered to the stainless steel wire leads to connect to the scleral coil system for eye movements recording.

2.1.2.2 Coil System Hardware

2.1.2.2.1 Magnetic Field Frame

The magnetic field frame is a cube, 30.5 cm on each edge, and made of single turn solid aluminum square rods (1x1 cm cross section, shown in Figure 12 in section 2.2.2.1). Each field coil pair, +X/-X (front/back), +Y/-Y (left/right), and +Z/-Z (up/down), is wired in series to make a two-turn inductor. Although previous designs [57,73,86] use multi-turn field coils to create a larger magnetic field, this single turn frame and the circuitry described below are more than sufficient for driving a large magnetic field.

2.1.2.2.2 Magnetic Field Driver Circuitry

The magnetic field for each of the three field coil pairs is driven by a MOSFET switching circuit operating at the three field frequencies, X: 245 kHz, Y: 498 kHz, Z: 763 kHz. The circuit uses a high-speed MOSFET driver (Texas Instruments, TPS28225), driven by a pulse width modulated (PWM) digital input from a FPGA (Xilinx Virtex-4 XC4VFX12-ST363), as the basis to control the switching of two N-MOSFETS (Texas Instruments, CSD18503KCS) at the resonant frequency of each field's capacitor/inductor pair. The capacitor for each field coil pair was determined based on the desired field component frequency and the field coil pair's inductance. A polypropylene film capacitor (KEMET Corporation) was used to set the resonance frequency based on the field coil inductance to allow ring up of the generated magnetic field. Optoisolation is provided between the FPGA and field driver using high-speed optocouplers (Vishay SFH6702) to prevent noise from ground loops.

2.1.2.2.3 Scleral Coil Signal Processing Circuitry

The induced scleral coil voltage is filtered and amplified via an ultra-low noise amplifier (Analog Devices, AD8331) before digitizing and demodulating the signal. The AD8331 includes a single-ended pre-amplifier followed by a variable gain amplifier (VGA) and a selectable gain post-amplifier. A user input command from a PC sets the VGA gain using a digital-to-analog converter (Texas Instruments, DAC7574) and can be easily customized to support scleral coils of varying

size. For the scleral coil design described above, the overall amplification is configured to provide ~100x gain for the raw scleral coil signal. Band pass filters are located at three stages throughout the amplification circuitry, with overall cutoff frequencies between 24 kHz and 1.5 MHz. After amplification, each scleral coil's amplified signal is digitized using a 12-bit, high-performance analog-to-digital converter (ADC, Texas Instruments, ADS5242). A 25 MHz clock from the FPGA drives 25 Msamples/sec simultaneously for up to twelve connected scleral coils. Each digitized scleral coil input is sent to the FPGA for demodulation.

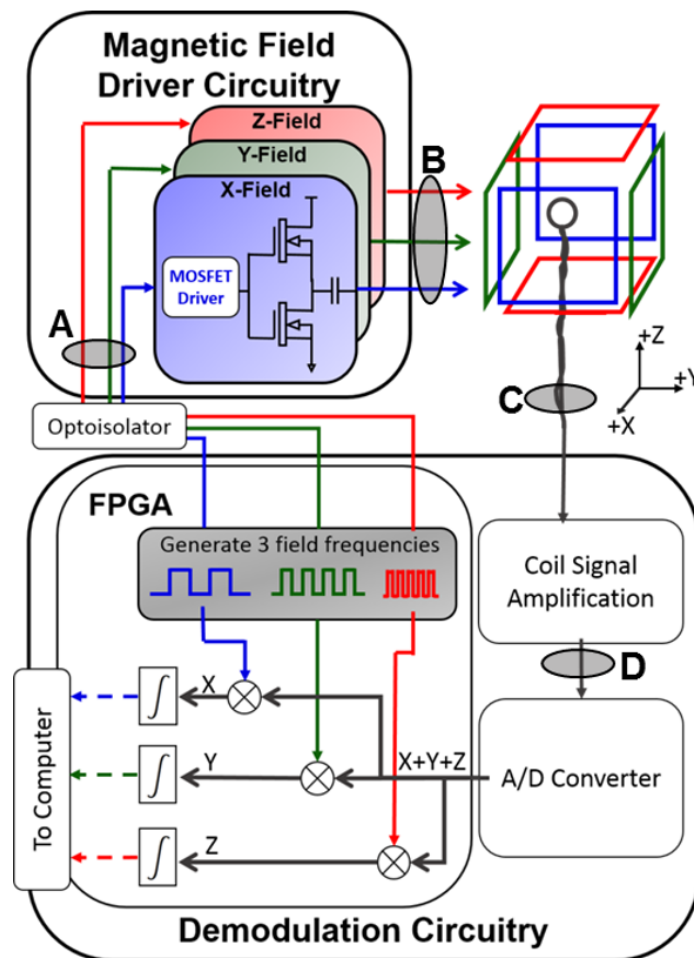


Figure 5. Block diagram of the scleral coil system architecture. FPGA outputs drive MOSFET switches in the magnetic field driver circuitry at three different resonant frequencies for the X, Y, and Z magnetic fields. The induced eye coil current is the sum of three components at different frequencies, plus their harmonics, with relative magnitudes dependent on the coil's orientation relative to each of the three fields. After amplification and analog-to-digital conversion, the FPGA demodulates the coil signal into the individual X, Y, and Z components required for 3D rotational kinematics analysis. The circles labeled A-D refer to test points shown in Figure 6.

2.1.2.3 Coil System Firmware and Software

The FPGA acquires the digitized 12-bit, 25 Msamples/sec signal from the scleral coils and then demodulates the signals using a multiply accumulate (MAC) unit. Each digitized scleral coil signal is separately multiplied with three different digital pseudo-sinusoids at each field's frequency, in-phase with the generated magnetic field to extract each component of the eye movement. As the accumulation occurs, it is summed over every 25 kSamples to provide three demodulated signals sampled at 1 kHz per scleral coil. Custom PC software, developed in C, acquires the demodulated signal at 1 kHz via a serial-to-USB interface (Future Technology Devices International Limited, UM232H-B-NC).

The FPGA also provides the digital driving signal for the magnetic fields mentioned above in section 2.1.2.2.2 which operates at the three field frequencies. These pulsatile driving signals operate at 60% duty cycle to reduce the high-current load on the MOSFET circuitry while still allowing for large enough field strength to obtain the desired induced signal. This duty cycle is easily programmable to increase the intensity of the fields if needed to use with even smaller scleral coils than those discussed. An additional digital pulse is delivered to the motion sensor (discussed in 2.2.2.3) for synchronization of motion and eye movement data.

2.1.2.4 Scleral Coil Data Analysis Procedures

The demodulated X, Y, and Z components from all connected scleral coils were analyzed using custom software in Matlab (Mathworks, Natick, Massachusetts), which uses 3D rotational kinematics to convert the three components from each set of scleral coils into rotation vectors that represent 3D movements. The pair of scleral coils from each eye was first mathematically orthogonalized to account for variation in surgical placement. All signal processing of the scleral coil signals is detailed in [84,85,87].

2.1.3 Results

2.1.3.1 System Characteristics and Bench Test Results

Bench-test results below were collected using the scleral coil of the design described in 2.1.2.1, unless otherwise specified. All system characteristics are summarized in Table 1.

The voltage traces in Figure 6 were measured at test points throughout the system (as labeled in Figure 5) to show the general progression of the signal that generates the magnetic field. Each of these system test points are shown in Figure 5. Each column was recorded with only one axis of the magnetic field on at a time. The PWM signal leaving the FPGA (Figure 6, top row) drives the MOSFET switch at the resonant frequencies of 245.3 kHz, 497.8 kHz, and 762.9 kHz for the X, Y, and Z fields respectively. At these relative resonant frequencies, the voltage at each field's capacitor rings up to 30.8 V, 42.4 V, and 48.8 V respectively (Figure 6, 2nd row). The quality factor (Q) measured at 100 kHz is 20, 24, and 25 for the X, Y, and Z fields respectively. The 3rd row of Figure 6 shows the raw, unfiltered voltage induced on the scleral coil when placed in the center of the magnetic field frame facing directly into the X-, Y-, and Z-field. At this stage, the high frequency switching noise from the MOSFET switch is very apparent in the raw signal. However, after filtering and demodulation, this noise is minimized and does not corrupt the signal which can be seen at the output of the amplifiers, bottom row of Figure 6. The final signal sent to be digitized and demodulated is approximately 100 times larger and the band pass filters eliminate the majority of the switching noise seen in the raw signal.

With all three fields turned on, the ring up voltage at the capacitor output for each field is shown in the top panel of Figure 8. The voltage induced in a small scleral coil placed at an angle partially facing into all three fields contains components of all three field frequencies shown in the bottom panel of Figure 8. As coil angular position changes, the proportion of the coil signal at the different frequencies changes. Thus, after demodulation, the change in position of the coil is determined based on the spectral components of the scleral coil signal.

Characteristic	X-Field	Y-Field	Z-Field
<i>System Design</i>			
Size of Frame (cm)	30.5 x 30.5 x 30.5		
Frame Inductance (μH , @100 kHz)	2.00	2.23	2.02
Capacitor for Resonant Circuit (nF @100 kHz)	222.4	47.2	22.3
Field Frequencies (kHz)	245.3	497.8	762.9
Q-Factor (@ 100 kHz)	20	24	25
Field Duty Cycle	60%		
Typical Scleral Coil Size	21 turns, 3-4 mm diameter		
Scleral Coil Channels	4		
Typical Scleral Coil DC Resistance ¹	100 – 200 Ohm		
Sampling Frequency	1 kHz on each of 4 Channels simultaneously		
<i>Power Consumption</i>			
Driver Board (W) ²	4.35	2.65	2.1
Optoisolator Board (W)	0.825		
Amplifiers + Demodulator (W) ³	7.15		
<i>Demodulated Scleral Coil Signal</i>			
Maximum Induced Coil Voltage	9.6 mV	11.1 mV	19.13 mV
Input Referred Noise (Pk-Pk) (amplifier input shorted)	5.0 μV 0.0056°	4.7 μV 0.0050°	5.0 μV 0.0046°
Facing Field Noise (Pk-Pk) ⁴	12.7 μV 0.014°	12.9 μV 0.014°	26.0 μV 0.024°
Perpendicular Field Noise (Pk-Pk) ⁵	9.8 μV 0.011°	5.8 μV 0.0063°	6.4 μV 0.0059°
Worst Case Linearity Error	Roll: 0.099°	Pitch: 0.099°	Yaw: 0.088°
Amplifier Channel Crosstalk	0.0085%	0.012%	0.0099%
Demodulated Field Crosstalk	Y: 0.60% Z: 0.12%	X: 0.10% Z:0.058%	X: 0.070% Y: 0.0015%

Table 1. A summary of the scleral coil system characteristics. ¹Use of stainless steel wire is required for chronic implantation of scleral coils to avoid breaking due to repetitive bending during eye movements. Therefore, the DC resistance is primarily due to the stainless steel leads from the coil. This value is not a limit to system, but the typical value. ²Measured using a 5 V power supply. ³Measured using a 12 V power supply. ⁴Measured with the scleral coil oriented so maximum coil area is parallel to field being measured, and thus maximum signal is obtained. ⁵Measured with the scleral coil oriented so minimum coil area is parallel to field being measured, i.e. scleral coil area is perpendicular to the field, and thus minimum signal is obtained.

The input referred noise of the amplifiers was measured without the coil frame's magnetic field turned on and the input to the amplifier shorted. The worst case noise floor of 5 μV peak-to-peak represents less than 0.005° of noise from the amplification/demodulation circuitry. With the fields

turned on and a scleral coil connected to the amplifier input, each demodulated component's noise floor increases to X: 12.7 μV , Y: 12.9 μV , and Z: 26.0 μV peak-to-peak when the coil is facing directly into each field to achieve maximum signal. Converted to degrees, this amounts to X: 0.014°, Y: 0.014°, Z: 0.024° of noise, shown in comparison with the old coil system in Figure 7. With the plane of the scleral coil perpendicular to each field, i.e. to eliminate induced voltage from that field, the noise floor of that component decreases. The peak-to-peak maximum induced voltage on the scleral coil when facing into the X, Y, and Z fields is 9.6 mV, 11.1 mV, and 19.13 mV respectively, producing a signal to noise ratio (SNR_X : 756, SNR_Y : 860, SNR_Z : 736) to allow recording of small eye movements.

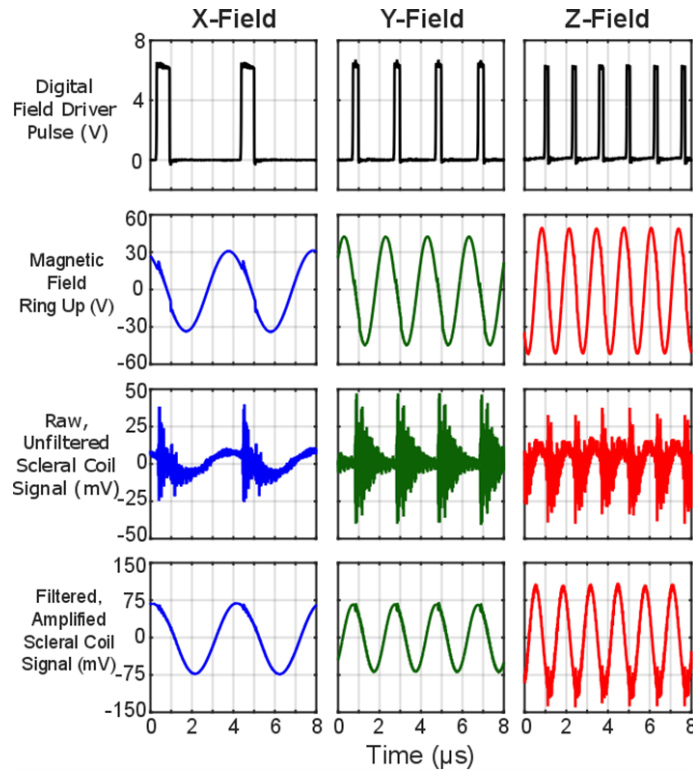


Figure 6. Voltages recorded at different stages in the scleral coil system. Example signals recorded at four different stages in the system with *only one field on* at a time. The signals in each row are recorded from the four test points labeled in Figure 5. The FPGA produces a digital pulse to control the frequency of each directional magnetic field (first row, test point A in Figure 5). The selected channel's resonant circuit creates a magnetic field that rings up to create a sinusoidal magnetic field (driving signal ring up in second row, test point B in Figure 5) at a different frequency for each axis. The raw, unfiltered signal of a scleral coil facing directly into the X, Y, and Z fields (third row, test point C in Figure 5). The high frequency noise is caused by the switching of the MOSFET driver. However, after the raw signal is amplified and filtered (bottom row, test point D in Figure 5) the high frequency noise is attenuated before digitization and demodulation.

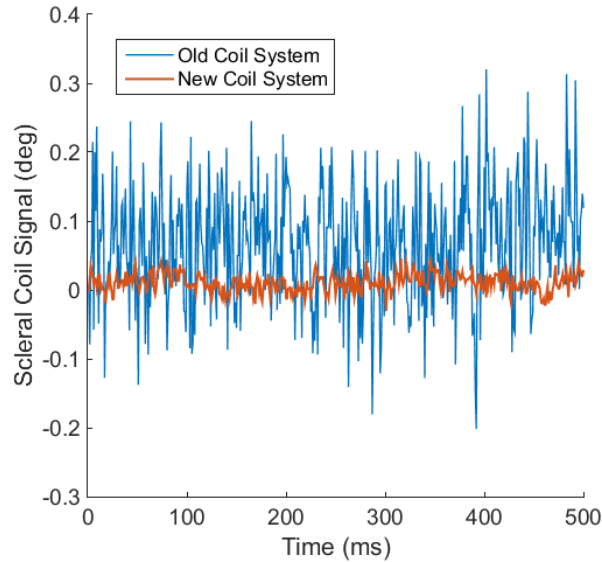


Figure 7. Noise floor comparison of old and new scleral coil systems. The noise floor of the old coil system (as discussed in [38]) using a new scleral coil design (discussed in section 2.1.2.1) was around 0.3° peak-to-peak, shown in blue. The new system offers over ten-fold smaller noise floor using the same coil, with a peak-to-peak noise floor less than 0.02° (shown in red). Each trace shows the Z-component of the demodulated scleral coil signal.

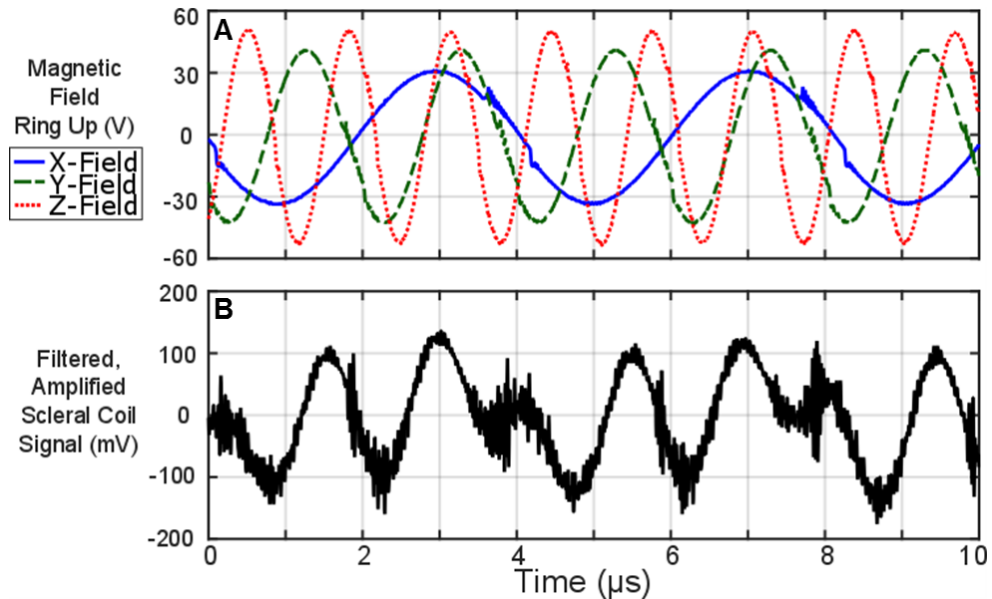


Figure 8. Induced voltage of scleral coil in the magnetic fields. The three sinusoidal magnetic field voltages all turned on simultaneously (panel A). With a scleral eye coil sitting still in the field facing approximately equal into the three fields, the filtered, amplified scleral coil signal (before demodulation, as measured from point D in Fig. 1) contains frequency components of each field (panel B). This signal is then digitized and demodulated to determine the three individual components of the 3D eye movement. Although high frequency switching noise from the MOSFET driving circuit is apparent, the demodulation of the signal is still sufficient to achieve the noise level reported in Table 1. A scleral coil moving in the frame would show a change in the frequency content of the induced voltage.

The step response of two different coil systems is shown in Figure 9. For both panels, each data point represents a sample from the demodulated signal with the scleral coil positioned to face approximately equally into each of the magnetic fields. In the top panel's coil system [66], which followed the design of Remmel [73], a monkey scleral coil (5 turns, 13 mm diameter) was used and the induced scleral coil voltage passes through an eight-pole Butterworth anti-aliasing filter with a 100 Hz corner frequency, detailed in [66]. Similar to the step response shown for the original Robinson design [57], there is ringing before the signal settles. In our new design, Figure 9 panel B, based on the high A/D input sampling rate and subsequent multiply and accumulate operation of the FPGA firmware (integrating and therefore effectively averaging over 25,000 ADC samples to produce each output sample), there is only one demodulated output data point during the transition from shorted to un-shortened input, thus eliminating any ringing of the signal after the step input.

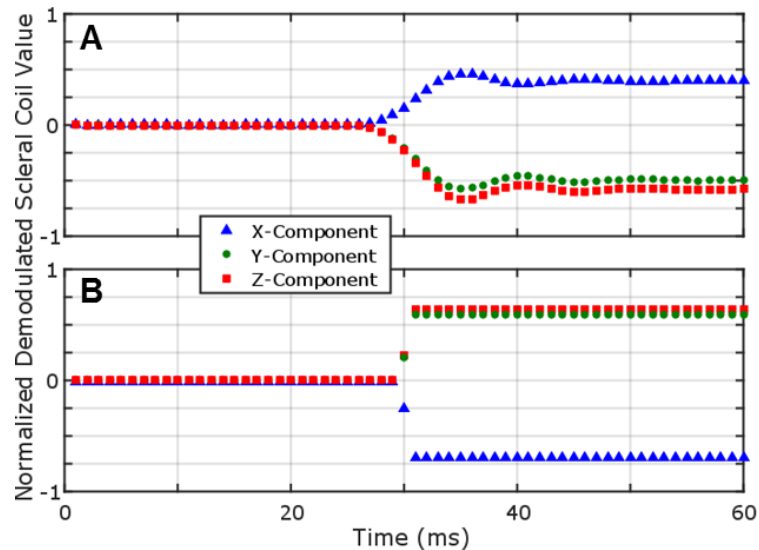


Figure 9. Step response of two different scleral coil systems. Comparison of the step response of an analog coil system [38] (A) and the step response of the new digitally demodulated coil system described in this report (B). For each example, the demodulated value recorded from a scleral coil is shown after being normalized to the maximum magnetic field strength for each axis of the magnetic field. The scleral coil was connected to the amplifier/demodulation circuitry facing approximately equally into each of the three fields. The file was started with the input shorted and then released to the coil input to show the step response dynamics of the system. The response of the analog system shown in the top panel illustrates ringing due to filtering of the analog demodulated signals (also shown in [57]). In the new system, due to the sampling rate of the coil signal (25 Msamples/sec) and digital domain averaging over 25kSamples to produce each independent 1 kHz output sample, further filtering of the demodulated signals is unnecessary, and the step response rises to the final value in just 2 samples with no overshoot or ringing.

The crosstalk between demodulated field components for a scleral coil signal was measured with one field on at a time and is reported as a percentage of the intended demodulated signal. For example, with only the X-field on, a scleral coil was pointed directly into the +X and -X direction. The ratio of undesired Y and Z demodulation is presented as percentage of the total magnitude of the X demodulated value. Measurements were repeated with each of the three fields on and crosstalk remained under 0.6%. Details can be found in Table 1.

The scleral coil channel-to-channel crosstalk between the four scleral coil amplifier channels was measured with three of channel inputs short-circuited, while a scleral coil was connected to the fourth channel. The scleral coil was moved to face into each of the three magnetic fields and any measurable crosstalk on the shorted out channels was presented as a percentage of the maximum value. While the majority of potential crosstalk between amplifier channels was below the noise floor, the maximum measurable crosstalk between scleral coil channels was 0.012%.

The variation in field strength as a coil is moved along the center of each field is shown in Figure 10. The voltage induced in a large coil (11 turns, 2 cm diameter) was measured at every 2.54 cm along each field's center axis. This large coil was used here to obtain high induced voltage for simplicity in mapping the field since the general homogeneity is characteristic of the magnetic field and not the specific scleral coil used.

To test the nonlinearity of the system, a rotary motion stage (Zaber LMR39, resolution of 0.000234 deg) rotated two roughly orthogonal scleral coils in 1.5° steps for a total 345° rotation (motor limitations prevented the full 360°) around three axes: roll (X), pitch (Y), and yaw (Z). The motor itself was located outside of the field so the metal would not distort the field. The demodulated X, Y, and Z components on a single coil rotating through roll, pitch, and yaw are shown in the top row of Figure 11. This normalized data from the single coil shows a representation of the proportionality of each magnetic field induced during a pure rotation in the indicated direction. The zoomed in portion within each window of Figure 11 shows the detail of the 1.5° steps of the motor. Using the second coil that was held orthogonal to the first during the rotation,

the coil system's measurement of the 3D rotational movement of the motor was found using rotational kinematics (detailed in [84,85]), shown in middle row of Figure 11. The residuals, bottom row of Figure 11, were calculated by the measured step size in the middle row versus the ideal 1.5° step, indicating the error in linearity. Nonlinearity remained less than 0.1° for all three rotations for the entire 345° rotated which is less than the reported nonlinearity of 0.3° in Primelec's commercially available system [75].

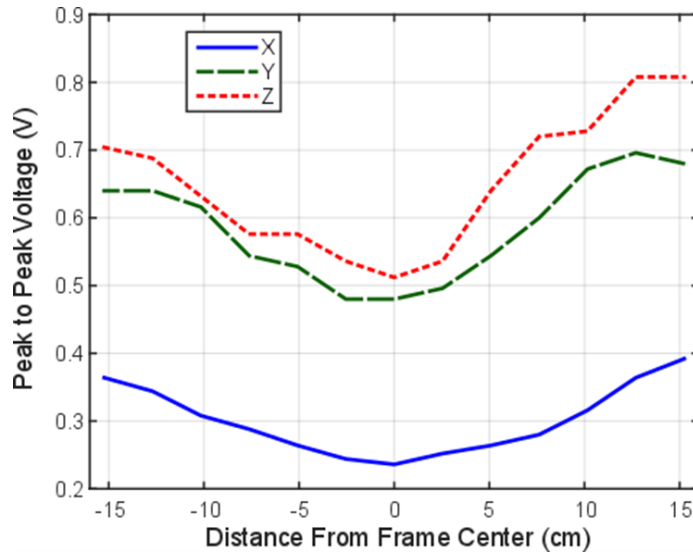


Figure 10. Homogeneity of the coil system's magnetic fields. Changes in magnetic field strength measured at different points within the field using a large test coil (11 turns, 2 cm diameter). With only one field on at a time, the field strength was measured from one frame face to the other along the center of the field where +X is to the front, +Y is out the left ear, and +Z is up. For example, the X trace shows values recorded from -X frame (-6, 0, 0) to +X frame (6, 0, 0), where (0, 0, 0) is the center. As expected, the strength is highest at the edges, where the scleral coil is sitting in the face of the frame coil that is creating the magnetic field. The asymmetry seen between the -Z and +Z frames are due to the presence of a metal motion platform that is located below -Z.

2.1.4 Discussion

In laboratory based vestibular research, it is important to be able to record precise eye movements from small animal models. Each method of eye movement recording, from EOG, VOG, and scleral search coil has its strengths and weaknesses for use in an animal model. With the “gold standard” of the scleral coil system [57] and its ability to record repeatable eye movements from the same animal over time, robust small coils were developed to work with such a system. To keep these

coils small while also using stainless steel wire to prevent breaking after implantation, the number of turns and diameter were minimized to 21 turns at 3-4 mm diameter. These smaller scleral coils do not provide a sufficient signal to noise ratio for measuring small eye movements in our previous system which was typically used with larger diameter implanted coils in non-human primates or 80 turn glue on scleral coils for smaller animals. The new system was developed with a simple magnetic field driver scheme and a straight-forward demodulation methods to give a low noise floor and high linearity and the ability to customize many features for other applications.

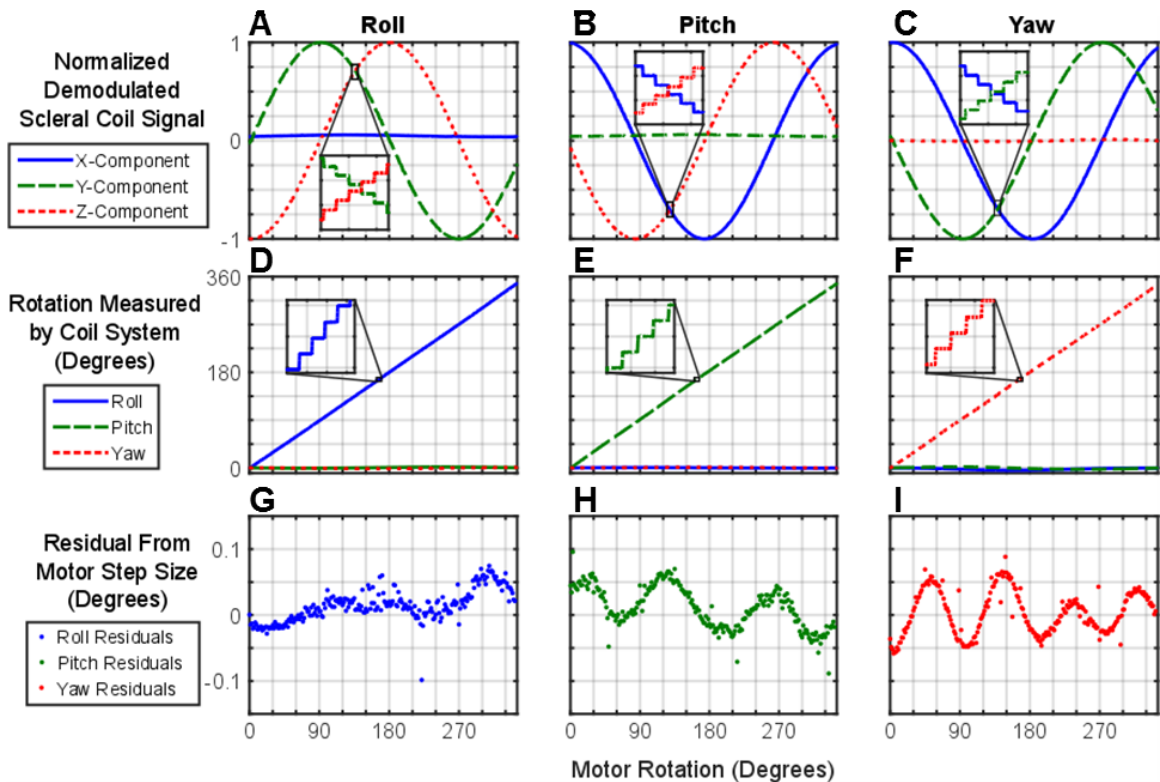


Figure 11. Linearity measurements of demodulated scleral coil signals. To measure the linearity error of the system, two mutually orthogonal scleral coils were centered in the middle of the frame. A precise motor (Zaber LMR39, resolution of 0.000234°) was programmed to rotate in 1.5° steps and hold for 3 seconds. The motor rotated 345° (motor limitations prevented full 360° rotation) about the X (roll), Y (pitch) and Z (yaw) axes, starting with one scleral coil's axis aligned with the Z, X and X axes, respectively. ABC: Demodulated components of the normalized raw signal collected from one of the two scleral coils during each rotation. Insets show the change in the recorded coil signal as the motor rotated through 5 steps. DEF: Post-processing of the demodulated data recorded from both coils gives the 3D rotation. GHI: Error residuals for coil system measurement compared to 1.5° step rotation commands to the motor. Worst case linearity error is $< 0.1^\circ$ for all directions.

The design of the magnetic field driver circuitry uses a simple digitally driven pulse to drive the entire resonant circuit that provides for a magnetic field ring up. The switching noise could be fully eliminated by changing the driving source to a sinusoidal input, but that would require more complex circuitry. With this design, not only does the circuitry remain simple with off the shelf components, but the high frequency switching noise is mostly eliminated from bandpass filters before amplification, as shown in Figure 6. In addition, since the switching noise is an artifact of the generated magnetic fields, any effect on the demodulator can be eliminated by demodulating the scleral coil signal with a signal from a reference coil placed near the animal's eye instead of comparing the measured coil signal to the pseudo-sinusoid (i.e. square wave at field frequency) in the FPGA.

The inhomogeneity of the field is as expected using the cube field design with higher field strength closer to the six faces of the cube. For experiments with a head-fixed animal, the inhomogeneity is not a problem because each eye rotates about a fixed point. To further mitigate effects of field inhomogeneity without changing the design of the magnetic fields as described in [88], a reference coil placed near the animal's eyes can be used instead of comparing the measured coil signal to the pseudo-sinusoid in the FPGA. This would help reduce all influences of inhomogeneity within the field and allow for experimental set-ups with a freely moving animal inside the frame.

The use of a single-ended amplifier for the raw scleral coil signal for amplification of the scleral coil signal requires the measurement of coil offsets at the beginning of each experiment due to capacitive influences coupled into the single-ended input. This offset must be subtracted from each demodulated value before completing rotational kinematics calculations. Future development should investigate using a differential amplifier to avoid the need to measure offsets of implanted scleral coils.

The new coil system presented in this section provides the ability to record 3D eye movements with a much lower noise floor than our previous system when using these new scleral coils (0.024°

vs 0.2° respectively). The low noise floor was achieved by using a strong magnetic field and by oversampling the raw scleral coil signal at 25 Msamples/sec, then averaging over 25 kSamples to give 1 kHz scleral coil sample. Due to this sampling method, the sample rate could be increased or decreased based on the needs of the experiment. Here, a 1 kHz sample rate was chosen since it is sufficient for recording saccades or quick phases of eye movements while still providing a low noise floor (since an increased sampling rate also increases the signal noise). The overall signal to noise ratio could also be increased by using larger scleral coils scaled for larger animals' eyes. With these scleral coils and the new coil system, small eye movements have been measured in a chinchilla model, with the scleral coils lasting 3 months on average for continued data collection in the same animal. For the scope of our research, this system allowed us to capture eye movements that we would not have been able to extract with previous systems.

In conclusion, with the low noise floor, linearity, and precision of our system, we can record smaller eye movements elicited by the vestibulo-ocular reflex. Overall performance improved our ability to record small eye movements in a repeatable manner with implanted scleral coils in a chinchilla. The system design remains simple, using off-the-shelf components. Customization of amplification level, resonant frequency, or sampling frequency can be completed by changing programmed FPGA settings and the resonant capacitors. This coil system design gives a worst-case noise floor of $12.6 \mu\text{V}$ (equivalent to $\sim 0.024^\circ$ of eye movements) and nonlinearity $< 0.1^\circ$ using a robust, small scleral coil design sufficient for rodent animal models such as the chinchilla.

2.2 Motion Stimulus

2.2.1 Introduction

Data collection in the Johns Hopkins Vestibular NeuroEngineering Lab has historically focused on the angular VOR and thus only required a rotational motor for rotations. As the prosthesis technology is extended to investigate electrical stimulation of the utricle and saccule and the translational VOR and ocular counter-roll, a different tool is required to provide a translational

acceleration stimulus and whole-body static tilts about any axis. Although a linear acceleration can be achieved using off-vertical axis rotations [77,89–93], the ocular movements elicited from this method have shown differences compared to those elicited from pure linear acceleration [94]. Therefore, a new system to rotate and translate the animal through six degrees-of-freedom (DOF) was created to deliver a motion stimulus to characterize the OORs of lateral-eyed animals.

2.2.2 Methods and Results

2.2.2.1 Motion Platform Overview

A six DOF motion platform (6DOF2000E, Moog, Inc.) was programmed to provide rotations, translations, and whole-body static tilts. The motion platform (shown in Figure 12) is designed using six electro-mechanical actuators that control the position of the platform. Internal control over the linear motion of each actuator coordinates the 6 DOF as follows: Pitch (rotation about Y axis), Roll (rotation about X axis), Yaw (rotation about Z axis), Heave (up-down), Surge (fore-aft), and Lateral (left-right).

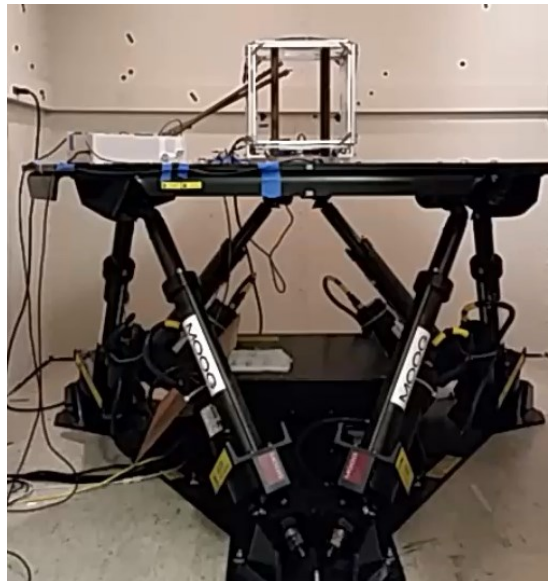


Figure 12. Image of the motion platform and scleral coil system. The 6 degree-of-freedom motion platform (6DOF2000E, Moog, Inc.) delivered controlled rotations about any axis, translations along any axis, and whole-body static tilts. The scleral coil system (metal cube on the top of the platform, discussed in section 2.1) measured the chinchilla's eye movements during motion.

2.2.2.2 Communication Protocol

Movements of the motion platform are commanded with User Datagram Protocol (UDP) Ethernet communication protocol. With Ethernet protocol, a sequence of commands is delivered to complete each full motion profile. Each command to the platform's internal computer contains information for the six actuators in one of three different forms: 1) length of the actuators, 2) degrees of freedom, or 3) acceleration rates. For the purposes of this project, the second method, commands in degrees of freedom context, was used for all implementation. Each data packet sent to the motion platform contained positional values for the six DOF: Pitch, Roll, Yaw, Heave, Surge, and Lateral. The protocol operates at a maximum of 60 frames/sec, meaning calculated motion profiles send each packet of information at 60 Hz.

To monitor the commanded movement, the motion platform can respond with the current orientation of the platform, also at a rate of 60 Hz. This response can be synchronized with each incoming packet to ensure proper timing between packets with 'Reverse' mode enabled on the motion platform. However, since 60 Hz is slower than ideal for synchronizing eye movements with the physical movement of the platform, a motion sensor was integrated into this system as discussed in the next section, 2.2.2.3.

2.2.2.3 Motion Sensor for Feedback

Since the VOR is a fast, compensatory reflex, the time delay between eye movement and head movement (only 7 ms [6]) requires temporally precise measurement of the animal's head movements to easily synchronize the eye and head movement data files. Due to the slow 60 Hz response time (~17 ms delay) of the motion platform's location, a motion sensor was integrated into the system to offer a higher sample rate tracking of the motion (offering head movement measurement with ~2.9 msec delay).

An inertial sensor (MPU9250, Invensense) was mounted in the middle of the platform and aligned with the appropriate coordinate system (+X nasal, +Y left ear, +Z up) to measure rotations and translations at 1 kHz for all 6 DOF. The sensor was connected to a high-speed serial to USB

converter (FT232H via the UM232H-B breakout module, Future Technology Devices International Ltd., FTDI). This breakout module transferred the serial data from the digital sensor to the PC using Serial Peripheral Interface bus (SPI) communication protocol.

To synchronize eye movement recordings with data recorded from the motion sensor, a digital sync pulse, created by the coil system (as discussed in 2.1.2.3) is recorded with the motion sensor data via the FSYNC input to the MPU9250. This digital pulse is used to time-align the motion and eye movements during post-processing.

2.2.2.4 Software Design

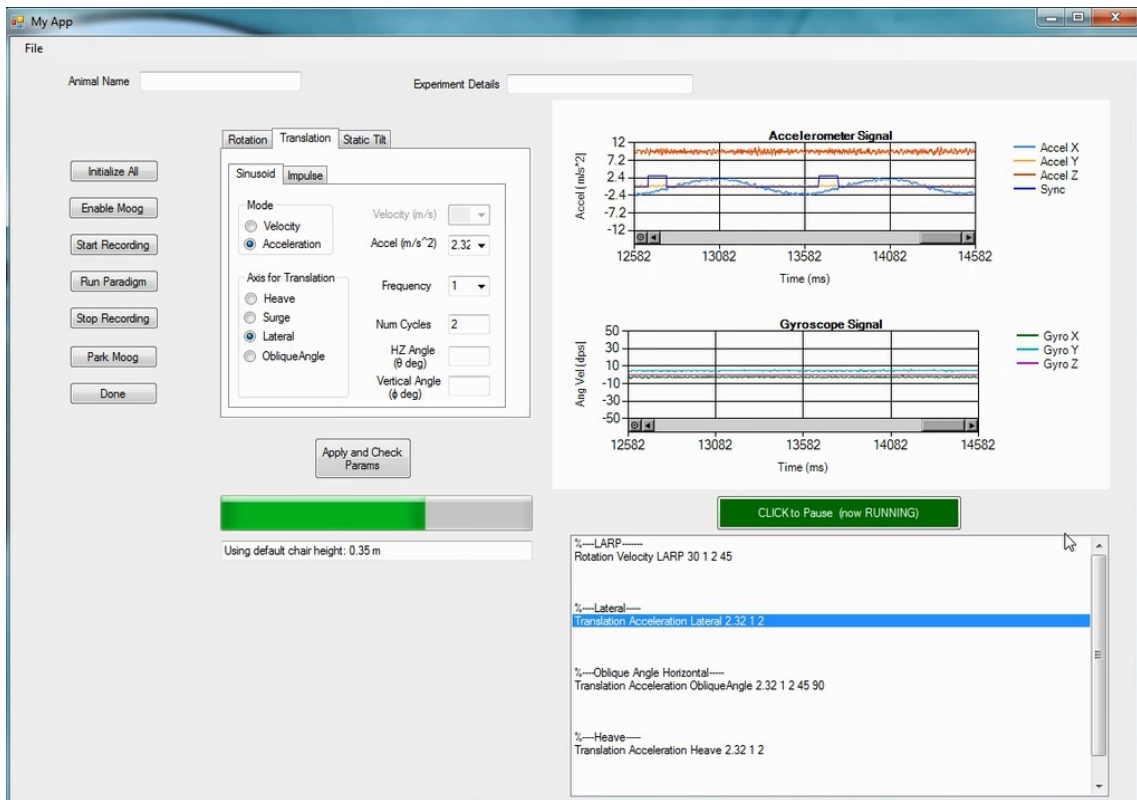


Figure 13. Graphical user interface for motion platform control. Custom C# software designed to control the Moog motion platform. Each tab can be used to command a rotation about any axis, or a translation along any axis. The integrated motion sensor measures the delivered motion and is plotted in the top right corner. Pre-determined scripts can be loaded to automatically run a set of stimuli. The software also communicates with the scleral coil system data acquisition program (discussed in 2.1.2.3) to synchronize the recording of motion and scleral coil data files.

Custom C# software was created to streamline the control of the motion platform during experiments, shown in Figure 13. The C# graphical user interface (GUI) collects user input containing the motion paradigm parameters (direction of rotation, translation, or static tilt, peak velocity or acceleration, frequency, number of cycles, etc.) to calculate the commands for the motion platform. Plots across the top of the GUI display the motion sensor data, offering feedback on the motion platform's movements. The digital pulse in the top plot shows the sync signal from the coil system. Additionally, the GUI controls the C code that acquires the coil system data, to further synchronize data acquisition across equipment. To streamline data collection, a script can be made with the parameters for all trials and loaded into the GUI. The GUI then steps through each command to start recording files (from the motion sensor and the coil system), run the motion paradigm, and stop recording the files.

2.2.3 Discussion

The entire system was tested for multiple motion paradigms including translations and rotation in 3D. Initial findings showed a discrepancy between the commanded motion amplitude and the actual motion amplitude (as measured by the motion sensor), more apparent at faster, higher frequency movements. Investigation into this discrepancy showed the error was due to the slow command rate (60 Hz) and limitations of the internal proportional-integral-derivative (PID) controller. The PID controller provides internal feedback to the motion platform's computer to constantly monitor the position and account for errors in position as new commands are delivered to the platform. Internal corrections for these errors caused lower amplitude movements than those commanded. With some reverse engineering, and the 1 kHz motion sensor feedback, we were able to determine what parameters to command to get our desired output.

Additionally, as the existing literature shows [79,80], the tVOR responses are small in lateral-eyed animals, and although the new coil system can measure small eye movements, a larger amplitude stimulus will drive larger, more robust eye movements. The Moog motion platform was

designed to move a large weight load and thus the velocity and acceleration limits are lower than desired and displacement limits restrict the peak amplitudes during low frequency sinusoidal movements. However, it proved to be sufficient for the goals of this work and characterization of the OORs.

2.3 Electrode Design

2.3.1 Introduction

Extending the existing Johns Hopkins multichannel vestibular prosthesis (MVP) to stimulate the utricle and saccule poses several engineering and physiologic/anatomic challenges. Previous electrode array designs for SCC stimulation in chinchillas (discussed above in section 1.2.4.1) were created from a twisted pair of 75 μm diameter Pt/Ir wire (AS169-40, Cooner Wire, Chatsworth, CA) stripped 0.2 mm and implanted into each SCC's ampulla. For SCC stimulation, a single electrode contact proved sufficient to evoke proper eye movements due to the uniform polarity of hair cells in each SCC. However, the non-uniform directional polarity of hair cells in the utricle and saccule, demands a more complex electrode array to provide stimulation contacts across the maculae compared to the SCC electrode array [29,32].

When increasing the density of electrode contacts in a limited area, electrochemical properties of the chosen electrode material and rules of safe charge injection prove an important constraint [95–97]. Electrical stimulation employs the movement of ions or charge to the tissue at the electrode/tissue interface. The delivered charge per area of the electrode must stay within safe charge injection limits (i.e., within electrochemical reversibility range) and all pulses must be delivered in charge-balanced biphasic pairs of alternating polarity to avoid charge buildup and irreversible electrolysis at the electrode/tissue interface. Historically, the most common electrical stimulation electrode material is platinum or iridium, due to the corrosion resistance of these metals [97].

2.3.2 Methods and Results

2.3.2.1 Design Constraints

A new electrode array was designed using a 3D anatomical chinchilla model reconstructed from μ CT scans described previously in [98] and shown in Figure 14A. We determined the best surgical approach to target the utricle and saccule and designed the electrode array to fit the geometry of the chinchilla labyrinth based on measurements taken from this 3D model. The design goal was to place an array of electrode contacts across the utricle and saccule maculae (Figure 14B) and have multiple electrode contacts in each SCC.

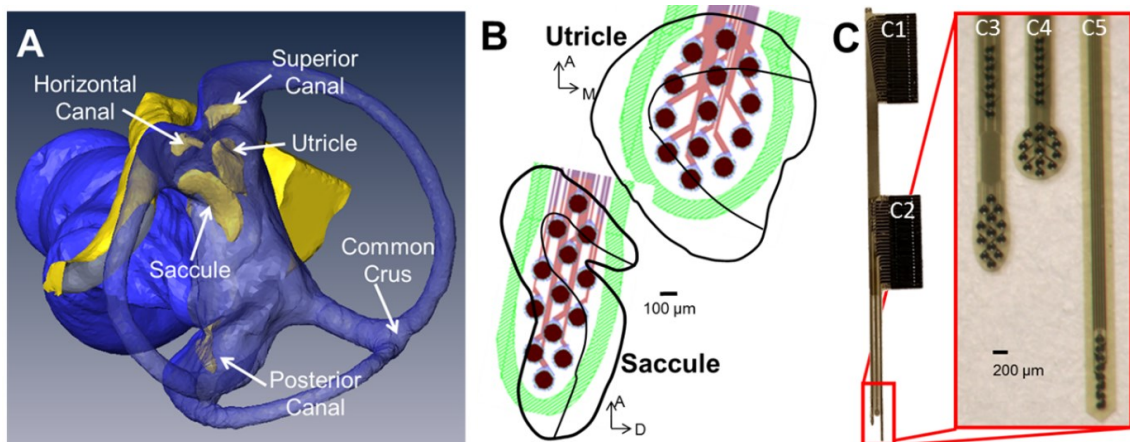


Figure 14. Custom polyimide electrode array design. **A.** 3D reconstruction from chinchilla microCT scans [98] was used to design new electrode arrays to target the utricle and saccule (blue indicates the lumen, and yellow the neural epithelium). Usual surgical landmarks can easily guide to the three canals for implantation, but to reach the utricle and saccule, we rely on the electrode geometry. **B.** The electrode array was designed to get as many contacts on the utricle and saccule while still maintaining safe charge injection. With these constraints, in addition to those from the fabrication process, an array of 13 activated iridium oxide film (AIROF) electrodes for the utricle and 13 for the saccule (outlines of end organs adapted from [99], green indicates the edge of each array) were designed to lay on the macular surface of each end organ. **C.** The fabricated polyimide array has two large connectors (C1 and C2) to interface with a printed circuit board and 50 electrodes total on three different shanks. The first shank (C3) has 8 contacts to target the horizontal SCC and the array of 13 for the saccule, the next shank (C4) has 8 contacts for the superior SCC with 13 for the utricle, and the final shank (C5) has 8 electrodes for the posterior SCC. The spacing and dimensions of the array were all measured from the 3D model.

Based on design constraints and anatomical dimensions, the electrode array has 13 electrode contacts for the utricle and 13 for the saccule with 8 for each of the SCCs, giving a total of 50 electrode contacts. A photo of the fabricated array is shown in Figure 14C. Each electrode contact is 101 μ m in diameter of activated iridium oxide film (AIROF). AIROF was used due to its

significant increase in the allowable safe charge per area ($1200 \mu\text{C}/\text{cm}^2$) compared to bare platinum electrodes ($24 \mu\text{C}/\text{cm}^2$) [97]. These electrodes can safely use up to $400 \mu\text{A}$ at $200 \mu\text{s}/\text{phase}$ (or any pulse amplitude and pulse width to give an equivalent $\mu\text{A} * \mu\text{s}/\text{phase}$) while staying under this safety limit.

2.3.2.2 Fabrication Process

The electrodes were fabricated using a 2-layer metal, multi-contact, polymer electrode design, following standard MEMS fabrication techniques, previously described in [100] and shown in Figure 15. For a brief summary, the processing steps begin with $5 \mu\text{m}$ deposition of a polyimide layer followed by deposition and patterning of trace metal 1 (Ti/Au/Ti). A second layer of polyimide ($2 \mu\text{m}$) is deposited atop the trace metal before O_2 plasma etching for interconnection vias. A second layer of Ti/Au/Ti trace metal is deposited and patterns followed by the deposition and patterning of the electrode metal (Ir). A final $5 \mu\text{m}$ layer of polyimide is deposited before electrode vias are etched using O_2 plasma. Finally, the device outline is etched using O_2 plasma. Iridium electrode contacts were activated using biphasic potential pulses in phosphate-buffered saline, forming the AIROF. An average impedance of $12.2 \pm 3.1 \text{ k}\Omega$ at 10 kHz was recorded in one representative array, as reported in [101].

Each electrode array was connected to a small custom printed circuit board (PCB) and epoxied in place before gas sterilization for implant. Two Pt/Ir wires (Cooner Wire, AS 169-40) were also connected to the PCB for a common crus electrode and a distant electrode in muscle. The PCB routes each of the 50 electrodes, and the distant and common crus electrodes, to two connectors that act as a percutaneous connection for the stimulation circuitry.

2.3.3 Discussion

The polyimide electrode arrays provided multiple contacts on each of the five end organs of the inner ear. The electrode material, polyimide, offered a planar, very flexible carrier for manipulation into the SCC surgical fenestrations for access to the utricle and saccule. However, the level of

flexibility of the polyimide and the planar design of electrode array made handling during surgery very challenging (see section 4.2.1 for details on the surgery and Figure 41 for image taken during implant). Additionally, post-mortem microCT scans, shown in Figure 43 and discussed in section 4.2.5, indicate that placement of the SCC targeted electrodes was successful in all animals, but the flexibility of the longer shanks of the utricle and saccule electrodes cause for greater variability in the final position of the electrode array. Continued development of the arrays will focus on adding a customized silicone stiffener at key points along the electrode array to allow for easier manipulation of the electrode during the implantation procedure.

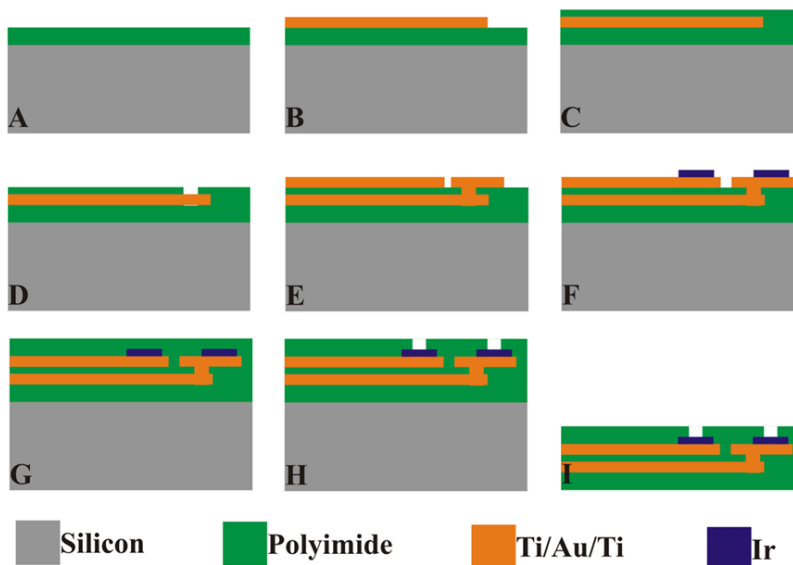


Figure 15. Cross-sectional view of the microfabrication process for polyimide electrodes. This design uses two layers of trace metal to route the electrode contacts to the connector, allowing a more compact design for multi-contact electrodes. The following describes each step of the process: **A.** Polyimide 1 Deposition (5 μm), **B.** Deposition and patterning of Trace Metal 1 (Ti/Au/Ti), **C.** Polyimide 2 Deposition (2 μm), **D.** Interconnection Via etching (O₂ plasma), **E.** Deposition and patterning of Trace Metal 2 (Ti/Au/Ti), **F.** Deposition and patterning of Electrode Metal (Ir), **G.** Polyimide 3 Deposition (5 μm), **H.** Electrode Via etching (O₂ plasma), **I.** Device Outline etching (O₂ plasma). (Images are not drawn to scale, image adapted from [100].)

Based on the measured impedances of the new electrode arrays and the use of the 12 V compliant MVP stimulation circuitry described in [102] and detailed in section 2.4, we can drive the new electrodes with charge-balanced, biphasic current pulses up to and beyond the safe charge injection limit. In previous work, this current range was well above that needed for vestibular

stimulation [29]. The increased number of electrodes and organized layout of the electrode contacts in the array provides greater control and increased capabilities for stimulation paradigms, creating the ability to stimulate across the chinchilla utricle and saccule. The overall layout of the electrode contacts on the array acted as a guide to implantation despite the inability to view the utricle and saccule during surgery, as documented in Figure 41. By using the dimensions from an anatomical model of the chinchilla inner ear, we were able to trust the geometry of the electrode array to reach the target end organs.

2.4 Prosthesis Development: Hardware, Firmware, and Software

2.4.1 Introduction

The Johns Hopkins Vestibular NeuroEngineering Lab’s multichannel vestibular prosthesis (MVP) architecture comprises motion sensing circuitry, a microcontroller, and stimulation management circuitry (schematized in Figure 16) and further detailed in [29,32,102]). In brief, motion sensor signals are converted to current pulses where magnitude, direction, duration, and timing are controlled by a microcontroller to generate variations in vestibular nerve afferent activity to emulate normal physiological encoding of head movement. (For review see [103]).

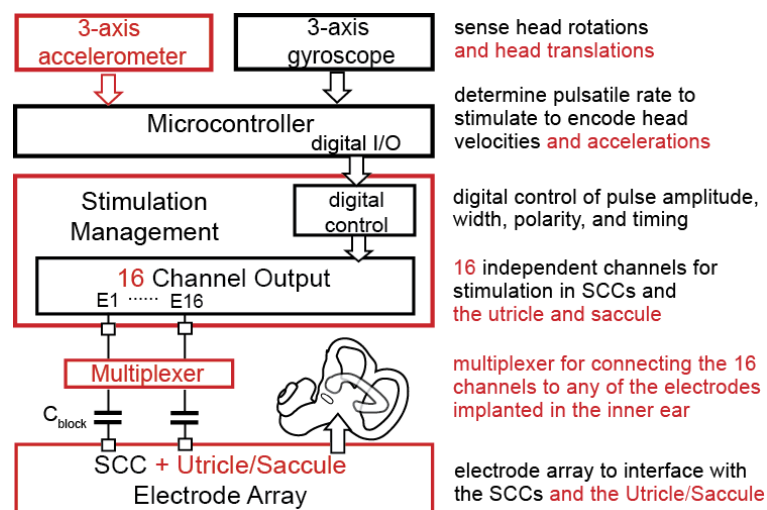


Figure 16. Vestibular prosthesis architecture required for extending the MVP. The black boxes and text show the existing framework of the prosthesis design [29,32]. Red boxes and text indicate additions needed to extend the prosthesis to also stimulate the utricle and saccule.

Figure 17 represents the design progression of the MVP system. The 1st and 2nd generation MVP system (MVP1 Figure 17A and MVP2 Figure 17B) were designed with a semi-implantable approach, using a percutaneous connection between implanted electrodes and external motion sensors, processing circuitry, and the power source. The MVP2 requires this connection to deliver stimulation to the ampullary nerves. To avoid the issue of decoupling, which would cause loss of stimulation from the prosthesis and sudden onset of vertigo due to loss of baseline stimulation, the design goal for the next generation MVP (MVP3) is intended to be a fully implantable system. For fully implantable vestibular devices, size and power consumption are key considerations, driving need for custom, low-power integrated circuit (IC) design.

Multiple groups have recently reported on efforts to develop application specific integrated circuit (ASIC) based stimulators for incorporation into vestibular implants, including a system based on a field-programmable analog array [104], a custom ASIC-based system including telemetry, power and stimulation management [105–107] and an ASIC-based system incorporating motion sensors [108]. Here we report on a complementary metal-oxide semiconductor (CMOS) application specific integrated circuit neural interface (ASIC-NI, Figure 17C) that was designed according to the MVP architecture [109]. This design provides the ability for pulsatile stimulation with pulses as short as 10 μ s/phase, amplitudes as high as 1.45 mA, and rates up to 12 kHz. The use of independent DACs in each of the 16 electrode channels allows for multipolar stimulation. The ASIC-NI is integrated with the MVP system by replacing the highlighted area of the MVP2 in Figure 17B to create the MVP2A. With the ASIC-NI, the MVP system provides equivalent stimulation to previous MVPs, but with a notable size and power consumption reduction. This size reduction is a first step toward reaching our system size goal to use the existing hermetic can of an implantable cochlear implant [110–112]. Outlines of existing cochlear implants are shown in Figure 17D for size comparison. The information in this section about the ASIC-NI development (2.4) can also be found in Hageman and Kalayjian et al. [102].

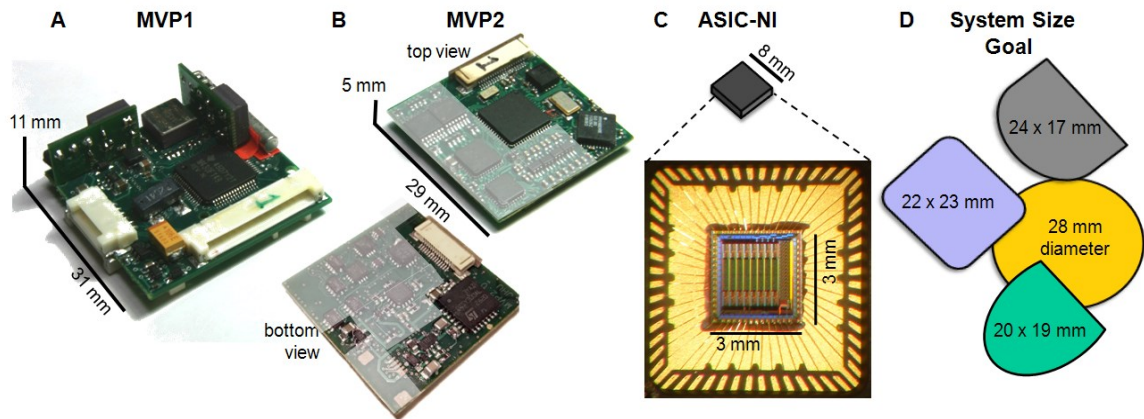


Figure 17. Design progression of the MVP. **A.** The first generation Multichannel Vestibular Prosthesis, MVP1, occupied 31 mm x 31 mm x 11 mm and consumed 100 mW [29]. **B.** Top and bottom views of the 2nd generation MVP2, which decreased in area, thickness and power consumption to 29 mm x 29 mm x 5 mm and 70 mW [32]. The highlighted area on the MVP2 (~866 mm²) indicates discrete analog elements replaced by the (C) 64 mm² QFN56A package for our Application Specific Integrated Circuit neural interface (ASIC-NI) and a photomicrograph of the fabricated chip in this package. The ASIC-NI allows for 48% size reduction in the MVP system size – which provides a significant first step to meet our system size design goals, shown in (D). The outlines in (D), drawn to scale with the MVP1 and MVP2, show the sizes of the hermetic cans of commercially available cochlear implants [110–112].

2.4.2 Methods and Results

The design of a new MVP system that includes additions to extend MVP application to stimulate followed a similar architecture as the previous versions, shown in Figure 16. Although this architecture is similar to that of previous generations [29,32], changes were required to extend the prosthesis to include utricle, saccule and SCC stimulation, briefly discussed in [101]. The system architecture has four main blocks, 1) custom C# software for wireless prosthesis programming, 2) a microcontroller, 3) a custom ASIC which provides stimulation management (described in full in [102]), and 4) a crosspoint switch to select which of the 52 electrodes to use. The system uses a 3.7 V rechargeable Li-Ion battery, which is regulated to 3.3 V for the microcontroller, and uses a step-up converter to reach 5 V and 12 V, which are both needed for the custom ASIC.

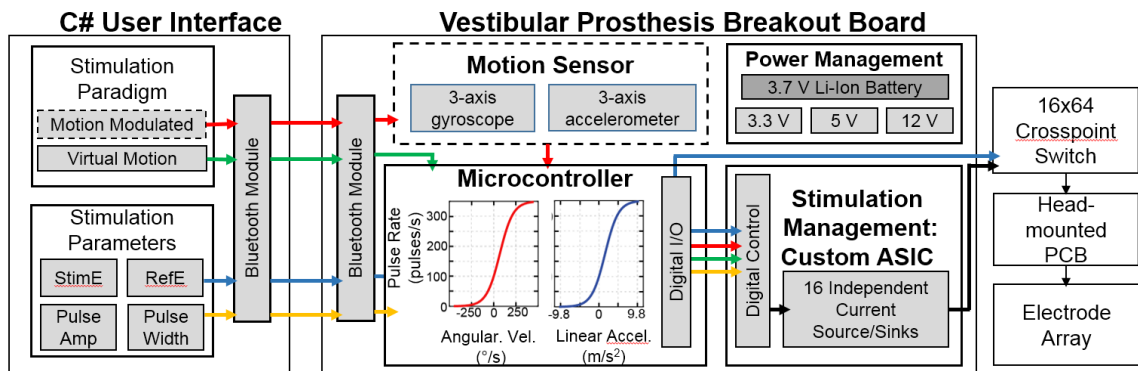


Figure 18. New multichannel vestibular prosthesis system design, created to interface with the new electrode arrays to stimulate the utricle and saccule (discussed in section 2.3). Although similar to the previous system ([29,32]), to also encode and stimulate translations and static tilts, additions to the software, hardware, and firmware were required. A custom C# graphical user interface (GUI, discussed in section 2.4.2.4) was created to program the prosthesis via Bluetooth. The GUI programs all stimulation parameters, such as stimulating electrode, reference electrode, and pulse amplitude and width. Additionally, the GUI controls the stimulation paradigm instructions sent to the prosthesis microcontroller set the pulse rate modulation. Although motion triggered pulse frequency modulation was not used for experiments detailed in this dissertation, the system architecture was created to easily integrate a motion sensor in the future. All virtual modulation paradigms change the pulse rate in order to encode a virtual movement while the animal is kept still. The microcontroller commands the passive application specific integrated circuit neural interface (ASIC-NI, discussed in section 2.4.2.2). The ASIC-NI's 16 output channels can be connected to any of the 52 electrodes (50 on the polyimide array, plus two additional distant electrodes in common crus and muscle) via a crosspoint switch (discussed in 2.4.2.3) which connects to the animal's percutaneous electrode connector.

2.4.2.1 Microcontroller and Motion Sensor Hardware and Firmware

The microcontroller (MSP430F5338, Texas Instruments) communicates with the C# GUI to run each experimental paradigm, manage pulse timing, and program the ASIC-NI and crosspoint switch appropriately for each pulse that is delivered. Although all of the data collected for this manuscript used 'virtual' head movements as the stimulus instead of motion sensor driven changes in pulse rate, the prosthesis was designed to easily integrate a 6 degree-of-freedom motion sensor (MPU9250, Invensense) for experiments in the future (dashed boxes and red arrows in Figure 18). The microcontroller drives the passive ASIC-NI to program the pulse amplitude, polarity, and the global enable to begin stimulation on the stimulating and reference electrodes. The microcontroller also sends a digital pulse to the coil system to be saved with all eye movement data to directly correlate electrically-evoked eye movements with the timing of the pulsatile stimulation.

New firmware for the microcontroller maps velocity-to-pulse rate [29] and includes a mapping for acceleration-to-pulse rate [5] (maps pictured in Figure 18). To test this mapping the motion sensor was mounted onto the 6DOF motion platform. The prosthesis was programmed for velocity-to-pulse rate on one “SCC-intended” electrode and acceleration-to-pulse rate on one “otolith-intended” electrode. The motion platform delivered a 2 Hz, 20°/s peak yaw velocity (Figure 19A), a 2 Hz, 2 m/s² peak acceleration lateral (left-right) sinusoidal acceleration (Figure 19B), and finally a combination of rotation and translation (Figure 19C). Instantaneous velocity, acceleration, and pulse rates on both electrodes were recorded for analysis.

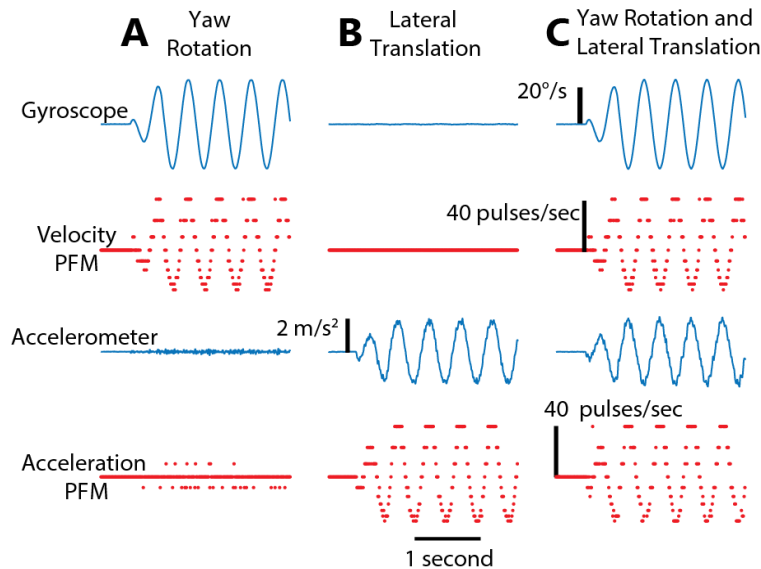


Figure 19. Pulsatile stimulation from rotations and translations. Instantaneous pulse frequency modulated (PFM) electrode output (red) and motion sensor signals (blue) during A. yaw rotation, B. lateral translation, C. simultaneous yaw and lateral movements. Pulse rate was modulated about a 100 pulses per second baseline rate. Motion sensor information to the microcontroller was sampled at 100 Hz to update the instantaneous pulse rate.

The updated MVP firmware successfully encode acceleration to pulse frequency modulated pulse trains. During translation (Figure 19B), the rate modulated appropriately above and below a baseline of 100 pps. During combined translational and rotational movement (Figure 19C), both outputs modulated appropriately without evidence of cross-coupling.

2.4.2.2 Stimulation Management: Custom Application Specific Integrated Circuit (ASIC)

2.4.2.2.1 ASIC Design and Fabrication

The ASIC-NI was designed to adhere to the existing control scheme of the MVP system. This custom design organizes the signals from the microcontroller, i.e. pulse amplitude, polarity, and timing, to efficiently produce the desired stimulation.

Delivering a given amount of charge per phase using shorter duration pulses achieves more selective stimulation of the vestibular nerve [41] and reduces the likelihood of timing clashes that would otherwise occur with longer-duration pulses. However, achieving the desired charge per phase with short duration pulses requires higher current levels, which in turn requires a relatively high compliance voltage and circuit elements that can withstand higher voltage levels. The MVP's requirements for electrode impedance and stimulation current output range dictate that the neuro-electronic interface operate at compliance voltages that exceed typical maximum voltages for standard CMOS processes currently available through contract semiconductor fabrication foundries. Therefore, the high-voltage OnSemi C5F/N CMOS process was used for design and fabrication of the ASIC-NI for the MVP. Compliance voltages of up to 12V are achieved using this process by virtue of high-voltage (HV) transistors featuring lightly doped drains (LDD) and thick gate oxides.

Each stimulation channel is individually addressed and programmed by the external, commercially available microcontroller through a digital multiplexer. Inside each channel, a 10-bit buffer stores the 9-bit current amplitude and 1-bit current direction. A global STIM signal is used to activate all channels simultaneously and provide stimulation.

The ASIC-NI's stimulation channel consists of a 9-bit DAC, a *partial current steering* circuit to obtain bipolar pulses, and control registers. The 9-bit DAC is a unary type current source array laid out in a common centroid arrangement to minimize mismatch. Current source transistor sizes were computed using a statistical yield model based on fabrication process parameters in order to achieve

maximal inter-channel matching within die area constraints [113]. Each DAC is programmed and activated independently for maximal stimulation flexibility.

To maximize battery life for a prosthetic stimulating device, the power consumption of the neuroelectronic interface must be limited. We implemented each stimulation sub-circuit using a *partial current steering* design similar to that described in [114] but realized using a high voltage, augmented differential pair amplifier with a wide range output stage (circuit and transistor sizes shown in Figure 20). This stimulation sub-circuit maximizes charge delivery while keeping stimulus pulses brief enough to allow high pulse rates up to 12 kHz (using minimum pulse duration of 10 μ s/phase and minimum interphase gap (IPG) of 25 μ s). Low-voltage transistors were used in the current source array for their superior matching properties. High voltage cascode transistors were employed to shield these low-voltage transistors from large voltage swings. The differential pair and standby path transistor are composed of HV transistors with gate signals constrained to a maximum of 5V; thus, the maximum voltage the DAC can see during normal operation is 5V.

The *partial current steering* circuit shown in Figure 20, provides three paths for current flow; one dummy path, one for cathodic pulses, and one for anodic pulses. When control registers for a channel are assigned for current stimulation but stimulation is not yet initiated, the DAC is activated and the current steering circuit is put on standby (*stby*). In this state, the programmed current is steered toward a low-voltage (5V) dummy load. This allows a lower voltage on the dummy path transistor, yielding lower power consumption in standby mode and simultaneously allowing the DAC current output to relax from charge-up transients. When the signal to enable stimulation is received from the microcontroller, indicating the start of the biphasic pulse, the standby circuit path is disabled and one of the differential pair transistors is activated based on the current direction (*dir*) signal, which chooses either anodic or cathodic current stimulation output. A non-overlapping switching network is used to switch between the dummy output path and the actual electrode output. This method of *partial current steering* has been effectively used to minimize power in a similar neural simulator [114]. A differential pair is then used to steer the circuit into HV current

mirrors, which either source or sink the programmed current into the electrode output, depending on the channel setting. The impedance of the output stage measured from the results of the output simulation is approximately 1.8GOhm. This was determined at a bias current of 300 μ A and an output voltage of $V_{dd}/2$.

2.4.2.2.2 ASIC Integration and Bench Test Procedures

Each ASIC-NI stimulating channel's DAC was initially tested using a 5V compliance voltage. All registers were cleared by a power cycle reset, and then output current levels were measured for each of the 16 channels for every possible 9-bit DAC command input. The DAC output current was measured using a Source Measurement Unit (SMU) with the output stage clamped at 2.5 V. Once DAC functionality was verified, tests were repeated with the compliance voltage at 12V.

After integration of the ASIC-NI into a MVP2A system board (which includes off-the-shelf MSP430F149 microcontroller (Texas Instruments, Dallas, TX), supply voltage regulation, DC-blocking capacitors, and other components), stimulus current measurements were repeated with the device set to deliver 150 μ s/phase, biphasic, symmetric current pulses with amplitude ranging from 0-1.45 mA between pairs of electrodes immersed in isotonic saline (0.9% NaCl). Bare 90% Pt / 10% Ir electrodes of contact area 51,000 μ m² (area equivalent to that of our *in vivo* electrodes, and therefore similar impedances) each were constructed by stripping Teflon™ insulation from the distal 200 μ m of 75 μ m diameter wires, each of which was connected to an ASIC-NI current source or sink via a series combination of a 1 μ F DC-blocking capacitor and a 10 Ω sense resistor used for current measurement.

Power consumption of the ASIC-NI was measured using 10 Ω sense resistors for each of the three power supply lines for the ASIC-NI (DVDD, AVDD, and V_{comp}). Quiescent power consumption was measured with output current set to 0 μ A across all ASIC-NI output channels. The instantaneous power consumption during a pulse output was measured at varying output currents, allowing for calculation of total operating power consumption based on current amplitude and duty cycle of pulse output.

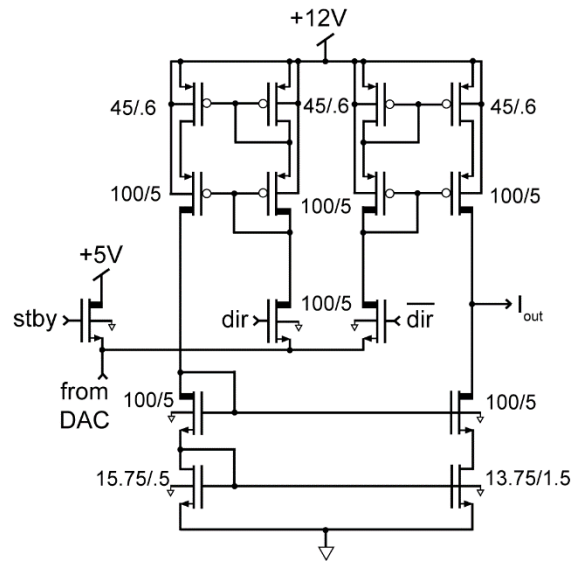


Figure 20. High voltage current steering schematic for the ASIC-NI. A high voltage steering circuit based on an augmented differential pair and cascode transistors with lightly doped drains (thick lines). Transistor sizes are indicated next to each transistor. The compliance voltage, V_{comp} , can be 5-12 V. The signal *dir*, supplied by the microcontroller, controls the direction of stimulus current (amplitude set by each channel's DAC). An additional signal *stby*, also provided by the microcontroller, is employed to minimize power consumption by putting the interface circuit into a standby state between pulses.

2.4.2.2.3 ASIC Performance

Table 2 summarizes bench performance results for the ASIC-NI. The DAC current output was measured and differential nonlinearity (DNL), and integral nonlinearity (INL, also termed relative accuracy) were calculated for all channels ($n=16$) on one ASIC-NI chip with a 12 V compliance voltage. Representative data from one output channel is shown in Figure 21. Using a best-fit method, the DNL magnitude is <0.8 least significant bit (LSB), and the maximum INL deviation from ideal was 5 LSB.

The output current settling time was measured using the maximum current output for the chip to calculate a worst case settling time. Both rise and fall times averaged 360 ± 50 ns. ($n=12$, four channels on each of three separate chips). This fast current settling time allows for short duration pulses with a maintained square pulse shape. The shortest pulse duration possible with the ASIC-NI is 10 μ s.

RESULTS MEASURED FROM THE ASIC-NI.

Characteristic	Measured Value
<i>Stimulator Characteristics</i>	
Max Current Output	1.45±0.06 mA
Output Current Resolution	9 Bits
Relative Accuracy (max)	±5 LSB
Differential Nonlinearity	±0.8 LSB
Offset Error	±0.2 % of Full Scale
Gain Error	±6 LSB
Output Current Settling Time	360±50 ns
Charge Balance	3.6±2.5 %
Current Out Channel Isolation	-39±10 dB (at 1kHz)
<i>Power Requirements</i>	
V_{dd} – core	5 V
V_{dd} – output stage	12 V
DV_{dd} – core	5 V
Quiescent Power Consumption	7.4±0.2 mW
Active Power Consumption*	7.7 mW

Table 2. Results measured from the ASIC-Neural Interface. *Calculated as described in 2.4.2.2.2 using typical multichannel vestibular prosthesis parameters of 94 pulses/second baseline rate on three channels, with biphasic pulses of 150 μ s/phase and 120 μ A.

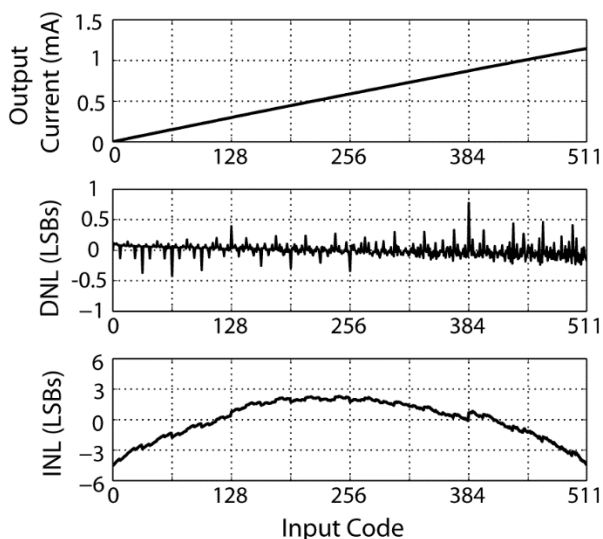


Figure 21. Representative DAC output from one ASIC-NI channel. This was recorded with V_{comp} set to 12 V and maximal current output at 1.2 mA. Current output was measured using a Source Measurement Unit with the ASIC-NI output clamped at 2.5V. Over the full range of DAC operation, the output is highly linear (top), differential nonlinearity error (DNL, middle) is ≤ 0.8 LSB, and integral nonlinearity (INL, bottom) remains within 5 LSB of ideal. The linearity in the DAC is more than adequate for the intended application of the DAC as a programmable interface for a prosthesis.

The ASIC-NI was designed to be used with DC-blocking capacitors to maintain charge balance between biphasic pulses. The charge balance between the cathodic and anodic phases without the DC-blocking capacitors was measured across five source-sink pairs on two separate ASIC-NIs. Data was collected from the ASIC-NI output for 10 seconds, with each pair programmed at 100 pps, 150 μ s/phase, 120 μ s IPG, at four different current amplitudes. The average difference in charge delivered between the cathodic and anodic phases without the DC-blocking capacitors is $3.6\% \pm 2.5\%$.

Current output channel isolation was measured by delivering a 1 kHz square pulse from one channel while all other channels were off. The frequency content seen at the output of neighboring channels was measured to quantify channel isolation. The average channel isolation was $-39 \text{ dB} \pm 9 \text{ dB}$, measured over all channels on two ASIC-NIs.

Figure 22 shows the DAC current output amplitude from three channels on each of three ASIC-NIs for 15 individual DAC input codes (between 0-511) as the compliance voltage is increased from 5 V up to the maximum 12 V. At low compliance voltages, the current output begins to saturate. With the high compliance voltage, the DAC is nearly linear over a wider range and achieves higher current output. The difference in maximum current magnitude between Figure 21 and Figure 22 is due to differences in measurement procedure. For Figure 21, the output node of the ASIC-NI was clamped at 2.5 V with an SMU. For Figure 22, a more realistic experimental set-up using electrode wires in saline, was used to measure the current output.

Replacing multiple discrete and off-the-shelf components of the MVP2 with the ASIC-NI significantly decreased the size of the MVP system (Figure 17). Whereas the MVP2 represents only a 12% reduction in circuit board area from the first generation MVP1 (Figure 17A), the MVP2A replaced all of the MVP2's stimulation circuitry (highlighted area of 866 mm^2 in Figure 17B) with the 8 mm x 8 mm packaged ASIC-NI, yielding a 48% further reduction in the system board area. With the integration of the ASIC-NI (photomicrograph shown in Figure 17C) and use of hybrid technology for mounting an unpackaged ASIC and other system components, we aim to have future

designs toward a finalized system fit in the hermetic enclosure of an existing cochlear implant (Figure 17D).

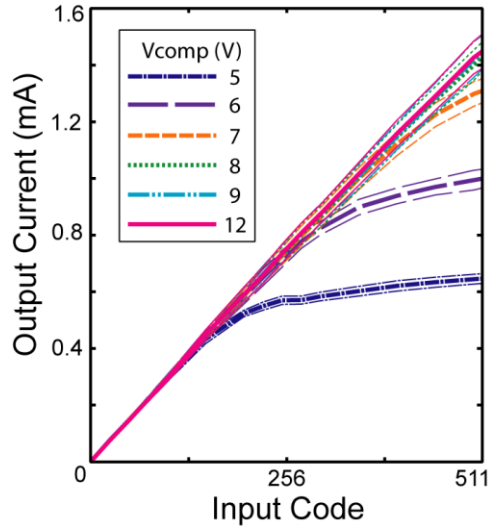


Figure 22. Current output from ASIC-Neural Interface at varying compliance voltages. Average current output (thick lines) from three ASIC-NIs, three channels from each ASIC-NI ($n=9$) using different voltages applied to the compliance voltage pin of the ASIC-NI (V_{comp}). Current values were measured at 15 input codes with a $120\ \Omega$ sense resistor for measuring current, in series with a $1\ \mu\text{F}$ coupling capacitor connected to a $75\ \mu\text{m}$ Pt-Ir wire electrodes with Teflon-insulation stripped $0.2\ \text{mm}$ and placed in normal saline (0.9% NaCl). DAC performance is linear for ($V_{\text{comp}} \geq 8\text{V}$), reaching maximum current levels of around $1.45 \pm 0.06\ \text{mA}$. The current output saturates as current is increased when using a V_{comp} below 8V . Standard deviations (thin line) ranged from $\pm 2.2\%$ to $\pm 4.5\%$ of the current magnitude. All values were collected using the same pulse rate and pulse duration.

The ASIC-NI consumes $7.4 \pm 0.2\ \text{mW}$ (P_0) during quiescent conditions when all channels are set to $0\ \mu\text{A}$ amplitude. A linear regression ($R^2=0.99$) of measured instantaneous power consumption during current output against current amplitude, showed an overall increase from P_0 of $1.2\ \text{mW}$ due to ASIC-NI operation, and an additional $0.02\ \text{mW}$ per μA of pulse output. With the typical parameters used for MVP stimulation, 94 pps on 3 channels with biphasic pulses of $150\ \mu\text{s}/\text{phase}$ (giving a duty cycle of 8.5%), and $120\ \mu\text{A}$ amplitude, the ASIC-NI power consumption is calculated to be $7.7\ \text{mW}$.

Using the ASIC-NI replaces circuitry in the MVP2 that consumed $\sim 20\ \text{mW}$ (based on specifications of the off-the-shelf components used). For the entire MVP system, the inertial

sensors remain the highest source of power consumption; however, improvements in MEMS technologies continue to achieve decreased power consumption for motion sensors. The optimized design of the ASIC-NI decreases the overall power consumption of the MVP2 system from 70 mW in the MVP2 [32] to 58 mW in the MVP2A. Despite the high power consumption of the inertial sensors used with the MVP2A, incorporation of the ASIC-NI enables production of a MVP with lower power consumption and, equivalently, longer device run time on a given battery's full charge.

The ASIC-NI's multiple current sources enable it to perform stimulation paradigms more complex (and potentially more physiologically effective) than the symmetric biphasic pulses most prostheses employ. For example, the ASIC-NI can deliver delayed-pseudomonophasic multipolar current pulses at 1 kHz (Figure 23), in which excitatory current passed by a single cathodic electrode near the target neural tissue is returned in different proportions to each of three anodic electrodes, redirecting the current field away from non-target neurons. In Figure 23, each trace displays the output of one of four electrodes; the bottom trace provides the main, cathodic first, stimulation while the top three act as the return electrodes to steer current of different magnitudes to the respective electrodes sites.

2.4.2.2.4 Physiological ASIC-NI Test Methods

After bench testing confirmed that the ASIC-NI met design specifications, performance of the MVP2A system was quantified during physiological studies of prosthetic stimulation in a vestibular-deficient rhesus monkey (F060738RhG; *Macaca mulatta*; 6-12 kg). The purpose of this experiment was to directly compare physiological responses achieved using the MVP2A system with those elicited by an existing and already well-characterized multi-channel vestibular prosthesis based on commercial off-the-shelf components, the MVP2 [32]. All animal experiments were performed in accordance with a protocol approved by the Johns Hopkins Animal Care and Use Committee, which is accredited by the Association for the Assessment and Accreditation of Laboratory Animal Care, and consistent with European Community Directive 86/609/EEC.

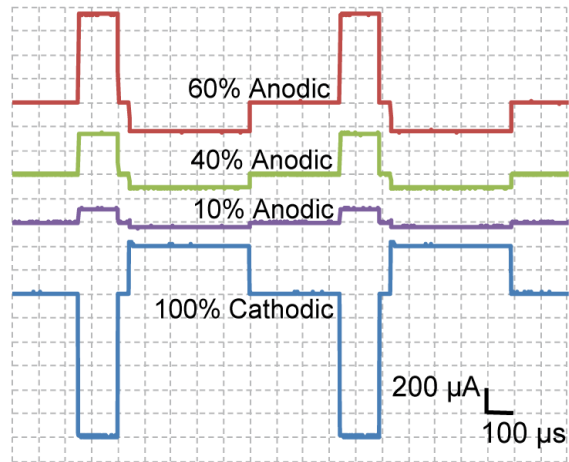


Figure 23. Example multipolar stimulation using the ASIC-Neural Interface. Two delayed pseudo-monophasic multipolar pulses for current steering [115] using four of the 16 stimulus output channels from the ASIC-NI, delivering pulses at 1 kHz. Although, the MVP uses a mono-polar configuration with charge-balanced, symmetric, biphasic pulses for stimulation this demonstrates the versatility in using the ASIC-NI. First phase: 150 μ s with the main stimulating source supplying a 1.2 mA cathodic pulse (bottom trace), while return electrodes steer current at 60%, 30%, and 10% returns of the total source. Interphase gap (IPG): 50 μ s; Second phase: 450 μ s pulse width, main current source at 400 μ A to maintain charge balance and return electrodes. Each channel's load was a 120 Ω sense resistor in series with a 1 μ F coupling capacitor connected to a 75 μ m Pt/Ir wire electrodes with Teflon-insulation stripped 0.2 mm and placed in normal saline (0.9% NaCl).

2.4.2.2.4.1 Surgical Overview

Surgical methods have been previously described in detail [32]. In brief, under general anesthesia (isoflurane, 1.5%-5%), the monkey was fit with a cylindrical plastic chamber secured to the cranium and aligned with the mean horizontal SCC axis. Two mutually orthogonal Teflon™ coated stainless steel wire coils were surgically affixed to the sclera of the right eye to permit precise measurement of 3-dimensional rotational position using the search coil technique [57,116]. The distal aspects of a MVP2 electrode array were implanted into the three ampullae of the left labyrinth via a transmastoid approach and run to a percutaneous connector embedded in dental acrylic within the protective plastic chamber [32]. The electrode array comprised 11 electrodes: three electrodes per ampulla (which were positioned as close as possible to the ampulla's neurosensory epithelium), a distal reference (placed in musculature outside the temporal bone) and a “near” reference inserted into the common crus of the labyrinth. Details on the electrode array

can be found in [32]. Electrode impedance measured around the time of the experiment of the three stimulating electrodes was 5 kOhms – 6 kOhms (measured with a 20 kHz square wave delivered across electrode leads). After recovery from the surgery, natural vestibular sensory function in the implanted ear was ablated via unilateral intratympanic injection of gentamicin (26.7 mg/mL, buffered with bicarbonate to neutral pH, dwell time 30 minutes under general inhalational anesthesia). This regimen has been proven effective at reducing the function of vestibular hair cells to cause a near-total failure of vestibulo-ocular reflexes [33,34,117].

2.4.2.2.4.2 Stimulation Protocol

The monkey was placed in a primate chair enclosure, using the head chamber as a means for atraumatic head restraint during the experiment. The monkey was kept in complete darkness during the experiment to avoid visual cues that would otherwise suppress or enhance VOR responses. The monkey was free to move its body and limbs within the enclosure, but its head remained stationary throughout the experiment to ensure that VOR responses observed were solely due to prosthetic electrical stimuli, which were delivered by the prosthesis with timing and amplitude appropriate to engender vestibular nerve activity that would typically occur in a normal animal during head rotation. Because the head was kept stationary, the microcontroller was programmed to replace signals from the MVP's gyroscopes with sinusoidal pulse-frequency-modulating waveforms that occurred independent of actual head movement, encoding virtual sinusoidal head rotations of 50 degrees per second (dps) at 0.1, 0.2, 0.5, 1, 2, and 5 Hz rather than actual movements of the head.

Current amplitude for each SCC electrode was optimized to maximize eye movement response slow-phase velocity while minimizing misalignment of the 3-dimensional VOR (which would indicate current spread to non-target branches of the vestibular nerve) and ensuring the absence of facial twitching (which would signify spurious activation of motor neurons in the nearby facial nerve). These optimized amplitudes ranged from 100-200 μ A, depending on the electrodes used. Both the MVP2A and the “gold standard” MVP2 delivered charge-balanced, cathodic-phase-first, 150 μ s/phase biphasic pulses with a 120 μ s interphase gap. Pulse rates were modulated over a range

of 68-130 pulses/s (pps) using a sinusoidal modulating waveform passed through a sigmoidal operating curve designed to emulate the normal encoding of head velocity into afferent neuron firing rate that is characteristic of normal rhesus monkey vestibular afferent neurons [29,32,40]. Parameters describing the operating curve parameters using the scheme in [29] were: $C=2$, baseline pulse rate 94 pps, and maximum pulse rate 350 pps. The range of stimulus pulse rates used was approximately equivalent to those that the MVP2 would typically generate during a sinusoidal head rotation with $50^\circ/\text{s}$ peak velocity.

At the outset of the experiment, baseline stimulation at 94 pps was applied asynchronously to each of the three SCCs while the monkey remained still in a well-lit room with a visually rich scene. At the onset of baseline, nystagmus was apparent with slow phase eye movements away from the prosthetically stimulated ear (and rapid nystagmus “quick phases” resetting the eyes back near the center of their range of travel). This is typical immediately after the sudden onset of a large asymmetry in aggregate afferent firing rates on vestibular nerves from the two ears. However, the animal being tested had experienced such transitions enough times during prior experiments to develop the ability to rapidly adapt (such context-specific adaptation is also seen in humans exposed repeatedly to rapid changes in vestibular or visual input [118,119]), so within 20 min of exposure to the baseline prosthetic stimulus in room light, her slow phase nystagmus faded to less than $\sim 5^\circ/\text{s}$, consistent with central vestibular nervous system neurons adapting to correct for the asymmetry (a process known as vestibular compensation [3]).

At this point, trials of stimulus pulse rate modulation began. Prior to modulating the pulse frequency for a given stimulus trial, eye position was confirmed to be within 10° of center via direct observation using an infrared camera. The camera was turned off when modulation began to ensure no visible light from the camera’s LEDs interfered with VOR responses. At least ten cycles were completed for each stimulation parameter set, for each of the three SCC’s. Pulse frequency was modulated for one electrode channel (and SCC) at a time; the other two were kept at baseline stimulus rates.

2.4.2.2.4.3 Eye Movement Recording and Analysis

Physiological responses to prosthetic stimulation were characterized through measurement of 3-dimensional (3D) VOR eye movements using our former magnetic scleral eye coil system that has been described in detail in [57,73,116] (different system than that described in section 2.1). Briefly, three pairs of wire coils were attached rigidly around the monkey chair, energized with sinusoidal currents at mutually prime frequencies, and oriented to generate three mutually orthogonal magnetic fields aligned to the head's nasooccipital (X, +anterior), interaural (Y, +left) and superoinferior (Z, +superior) axes. Fields generated by these coils in turn induce currents in each scleral coil that can be demodulated to yield signals proportional to the angle between the scleral coil's axis and the axis of each pair of field coils. By using two approximately orthogonal coils affixed to one eye, one can obtain the eye's 3D rotational position (with respect to a starting reference) and angular velocity through 3D rotational kinematics analysis using well-established methods described in detail in [84,85,87]. Trials including blinks were removed prior to further analysis. Positive and negative half-cycle gains (i.e., slow phase eye velocity divided by virtual head velocity during the excitatory or inhibitory cycles, respectively) were computed for responses to stimuli delivered by either of two systems: the standard MVP2 or the new MVP2A system.

2.4.2.2.5 Physiological Results Using the ASIC-NI

A side-by-side comparison of cycle-averaged eye movement responses to 1 Hz stimulation delivered either by the MVP2 or the MVP2A is presented in Figure 24. These eye movements were measured during 1 Hz sinusoidal pulse-frequency-modulated stimulation between 68 and 130 pps (comparable to the modulation of natural afferent firing rates during a 50°/s peak sinusoidal rotation in a normal monkey [40]). Delivered stimulation to electrodes implanted in the left horizontal SCC elicited predominantly eye movements in the horizontal plane (Figure 24AB), stimulation to the anterior SCC elicited eye movements aligned with the LARP plane (Figure 24CD), and stimulation to the posterior SCC elicited eye movements in the RALP plane (Figure 24EF). The standard deviations for each cycle-averaged response are all $\leq \pm 2.4$ %/s.

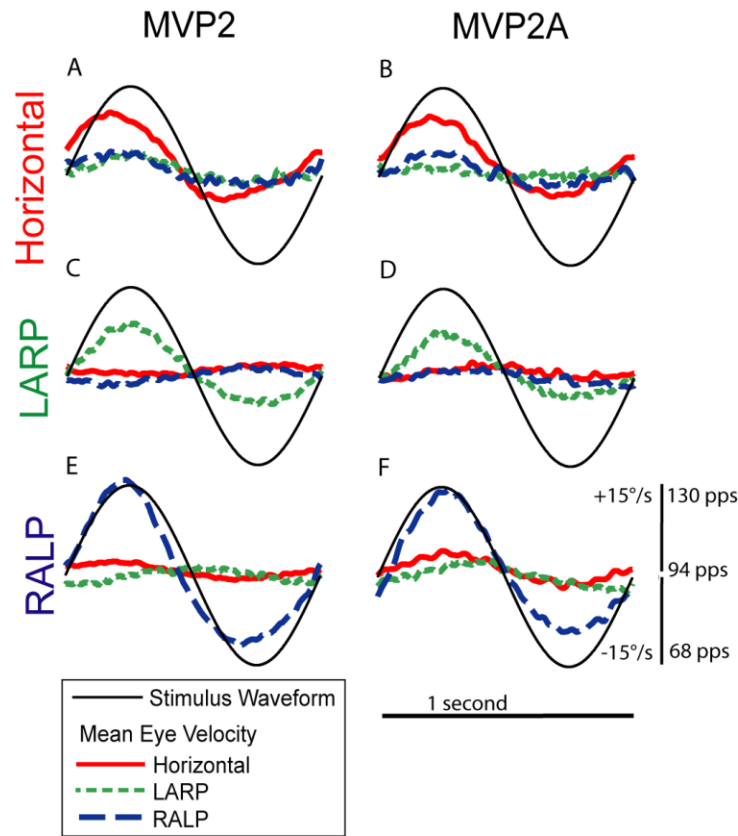


Figure 24. Comparison of electrically-evoked eye movements from the MVP2 versus the ASIC-based MVP stimulator circuitry (MVP2A). Each panel shows cycle-averaged vestibulo-ocular reflex eye movement responses of a stationary, head-fixed monkey (F060738RhG) during 1 Hz sinusoidal modulation of stimulus pulse frequency between 68 and 130 pulses per second (pps) around a baseline of 94 pps (using stimulation parameters detailed in the text), which approximates neural activity that occurs during a 50°/s-peak 1Hz rotation in normal monkeys [36]. **A,B:** Stimulation targeting the horizontal semicircular canal elicits eye movements dominated by the horizontal component. **C,D:** Stimulation targeting the left anterior (LA) canal elicits eye movements aligned with the left anterior and right posterior (LARP) SCCs. **E,F:** Stimulation targeting the left posterior (LP) canal elicits eye movements aligned with the right anterior and left posterior (RALP) canals. Traces indicate cycle-averaged mean slow phase velocity after removal of saccades and smoothing with a nonlinear low pass filter. Standard deviations are $\leq \pm 2.4^\circ/\text{s}$ for each trace at each point in time.

Figure 25 shows averaged aVOR gains at 0.1, 0.2, 0.5, 1, 2, and 5 Hz in each canal. Data are displayed separately for excitatory and inhibitory half-cycles. The MVP2 produced eye movement responses ranging from 1.9-16.7°/s (gains from 0.04-0.33) and the MVP2A evoked 2.0-14.2°/s (gains from 0.04-0.28). Standard deviations of all eye velocities were less than $\pm 4^\circ/\text{s}$ at each data point. The ratio of the VOR gains elicited by the MVP2 to those by the MVP2A was used in a t-

test of the hypothesis that the ratios come from a distribution with a mean equal to 1 (where a ratio of 1 implies the same VOR gain for each device). The t-test indicated the null hypothesis that the mean of the ratios is equal to 1 cannot be rejected at the 5% significance level, suggesting no detectable difference between VOR gains produced by the MVP2 vs. the MVP2A ($p=0.34$, 95% CI=[0.94, 1.17]).

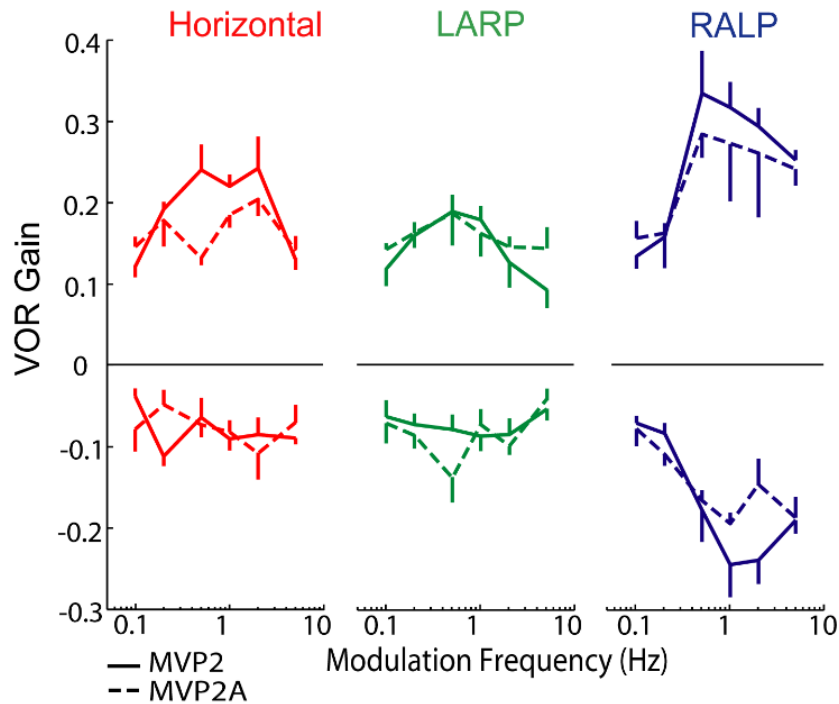


Figure 25. Gain of electrically-evoked aVOR responses in monkeys using the MVP2 and MVP2A. Excitatory (top) and inhibitory (bottom) half-cycle gains for 3D vestibulo-ocular reflex eye movements of monkey F060738RhG evoked by a 0.1-5 Hz sinusoidal modulation of pulse frequency using the parameters described in Fig. 6. Mean responses ranged from 1.9 to 16.7 °/s (gain of 0.04-0.33) with the 2nd generation multichannel vestibular prosthesis, MVP2 (solid) and from 2.0 to 14.2°/s (gain of 0.04-0.28) with the ASIC-based MVP system (MVP2A, dashed). Statistical analysis showed no detectable difference (t-test, $p=0.34$) between the VOR gains produced by the MVP2 vs. the MVP2A.

2.4.2.3 Crosspoint Switch

The crosspoint switch board contains four 16x16 multiplexers (AD75019, Analog Devices) to give an overall 16x64 multiplexer (shown in Figure 26). This allows any of the 16 ASIC output channels to be connected to any of the 50 electrode contacts or 2 reference electrodes. The crosspoint switch uses a serial programming scheme commanded by the microcontroller firmware

and C# GUI. The crosspoint output is connected directly to the head-mounted PCB that provides a percutaneous connection to the 52 implanted electrodes.

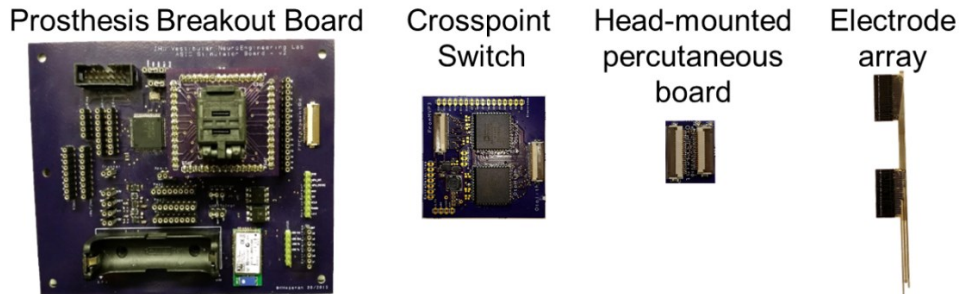


Figure 26. Hardware of the new MVP system designed for stimulation of the three SCCs and the utricle and saccule. The prosthesis breakout board contains the microcontroller, the ASIC-NI and Bluetooth module, as well as power management circuitry. A crosspoint switch board is used to route the 16 ASIC-NI outputs to any of the 52 electrodes on the electrode array. A small printed circuit board is used as a percutaneous connector, where the electrode array is connected to the board and implanted.

2.4.2.4 Overall System Hardware Results

Although ASIC-NI development greatly reduced the system size, for experimental purposes, a larger breakout board, shown in Figure 26, was created for the initial experiments. The larger board provides ease of customization and integration of auxiliary components as the system is tested. Physiological test results of the overall system (and not just the new ASIC-NI, as presented in section 2.4.2.2.4) is proven by all experimental data shown in Chapter 4.

2.4.2.5 Prosthesis Graphical User Interface

Custom C# software was developed to provide a streamlined graphical user interface (GUI) to wirelessly program the prosthesis using Bluetooth protocol. The software, shown in Figure 27 allows for straightforward connection between the microcontroller, ASIC, and crosspoint switch to program the stimulating and reference electrodes (blue arrows in Figure 18). With 52 electrodes and 16 ASIC-NI stimulating channels, the software allows efficient visualization of which electrodes are connected to the through the crosspoint switch circuitry (shown as yellow highlighted electrode numbers in Figure 27), which is easily reprogrammed to connect different electrodes. Additionally, the software has two other electrode designs integrated into the user interface. When

a different electrode array is selected in the GUI, the pictorial representation of the array is changed to better represent the appropriate electrode array used for the experiment.

Multiple stimulation paradigms are possible with this software, mainly implementing ‘virtual’ head movements since the present circuitry does not include a fully integrated motion sensor. (‘Virtual’ movement refers to holding the animal stationary and in the dark but modulating the pulsatile frequency as though the MVP were sensing an actual head movement). In this nomenclature, a ‘virtual rotational head impulse’ is a short burst of electrical pulses delivered via SCC electrodes, and a ‘virtual translational head impulse’ is a short burst of electrical pulses delivered via electrodes near the utricle or saccule. ‘Virtual sinusoidal rotation or translation’ denotes sinusoidally pulse-frequency-modulated stimulation using the sigmoidal map from head rotational velocity (e.g., Figure 19A) or head translational/gravito-inertial acceleration (e.g. Figure 19B), respectively, to pulse frequency. Similarly, ‘virtual static tilt’ denotes a step change in pulse rate that is held for 40 sec duration and delivered via an electrode targeting the utricle or saccule. Although this stimulus may not exactly replicate the pattern of macular and ampullary nerve activity that normally occurs during a head (because it does not include a burst of SCC electrode stimulation representing the head rotation normally required to reach a new head orientation), the term ‘virtual static tilt’ will be used throughout this dissertation to indicate a 40 sec pulse train delivered via a utricle or saccule electrode. The GUI software sends all necessary parameters to the microcontroller to complete each stimulation trial, including pulse amplitude, rate, duration, polarity, and all other pulse timing information.

Due to the large number of parameters required for each individual data set, the software was designed to maximize data collection efficiency and streamline changing of parameters through automation. A pre-determined script for each experimental protocol can be loaded before the experiment begins. The software then steps through the script to load all required parameters, program the microcontroller and complete each set of data collection without requiring individual use case parameters to be manually updated for each trial. Additionally, this GUI communicates

with the coil system software to synchronize stimulation and eye movement recording files.

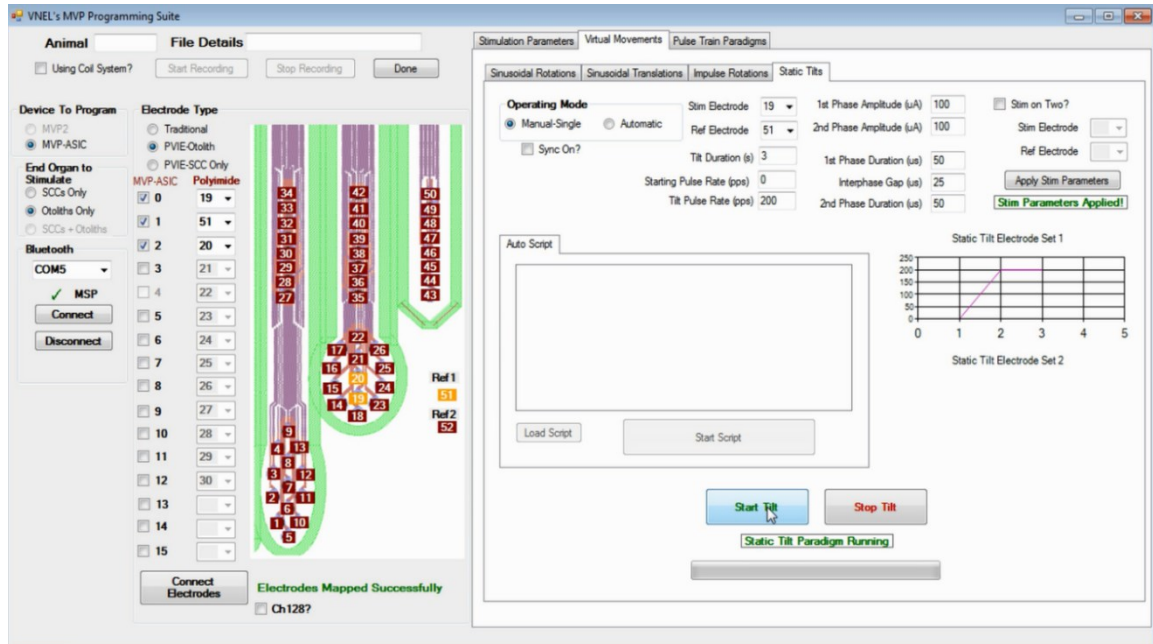


Figure 27. Custom C# graphical user interface (GUI) used to wirelessly program the prosthesis via Bluetooth. The GUI design illustrates the electrode array in use and provides an easy way to program and to visualize which electrodes are connected to the ASIC-NI's 16 outputs. The software can run multiple different stimulation paradigms, including virtual sinusoidal rotations and translations, pulse trains, and virtual static tilts. Each paradigm can be completed with a script to streamline data collection. Additionally, this software communicates to the coil system software to synchronize file names of stimulation and eye movement data files.

2.4.3 Discussion

The first generation MVP1 (Figure 17A) was designed for initial proof of concept experiments in animals receiving chronic multichannel stimulation of vestibular afferents. While it proved effective for that purpose [29], its 100 mW power consumption and 31 mm x 31 mm x 11 mm size are both large compared to cochlear implants currently used in clinical practice [110–112]. The MVP2 (Figure 17B) increased the number of possible electrode outputs and decreased size and power consumption to 29 mm x 29 mm x 5 mm with 70 mW, respectively, but to create a fully implantable device, further size and power reductions are needed [32].

Development of the ASIC-NI (Figure 17C) is the first step in realizing our 3rd generation MVP (MVP3), which aims to be a fully implantable system that can fit into an existing cochlear implant

hermetically sealed can (outlines pictured in Figure 17D). While the MVP2A system uses a commercially available microcontroller, further minimization could be accomplished by integrating the ASIC-NI with an on-chip microcontroller or a separate microcontroller mounted atop a hybrid substrate. This would avoid use of the 8 mm x 8 mm QFN package, shown in Figure 17C, which was chosen to simplify initial testing in the present design iteration. While ASIC-NI integration reduced the existing MVP system power consumption by 17%, off the shelf motion sensors are still the dominant factor in power consumption. Fortunately, market forces driven by the consumer products industry continue to drive the size and power consumption of inertial motion sensors downward. With the replacement of existing MVP2 motion sensors (45 mW [32]) with a new Invensense MPU9250 sensor (~10 mW [120]) as well as the development of the ASCI (7.7 mW) replacing (~20 mW off the shelf components as determined by product specification documents), the overall power consumption can be reduced even further.

With 16 independent, accurate, and highly linear 9-bit DAC output channels that each produce up to 1.45 ± 0.06 mA across a load impedance of ~ 10 k Ω (measured with a 20kHz square wave delivered across electrode leads) and can be activated simultaneously to generate multipolar stimulus profiles that steer current toward target fibers while steering it away from nontarget fibers, this ASIC-NI realization is well suited for prosthetic vestibular stimulation. The extended current range and additional electrodes provide opportunities to build upon the current prosthesis design to include multipolar stimulus configurations, stimulation of otoconial sensory organs (to encode linear accelerations and head orientation), stimulation of the semicircular canals in both ears, or to create a hybrid device that restores both cochlear and vestibular sensation (e.g., using eleven electrodes for the cochlear array, three electrodes for vestibular array, and two reference electrodes). Moreover, the ASIC-NI can also serve as a general purpose neuroelectronic interface for devices intended to stimulate other parts of the nervous system, see Appendix 6.1 for details.

The ability to use a compliance voltage of up to 12V was realized with the high-voltage OnSemi C5F/N CMOS process, which employs HV transistors. While the high compliance voltage was

specified to allow delivery of very brief stimulus pulses via the relatively small electrodes (such as those we have previously used in chinchillas [41,42] and prior experiments with rhesus monkeys [44]), in the present study we typically observed robust responses to stimuli with pulse widths of 150 μ s and current levels of 100-200 μ A delivered across a load impedance of \sim 10 k Ω (measured with a 20kHz square wave delivered across electrode leads). A compliance voltage below 5V could achieve these current levels and would have the advantage of allowing us to use a more generic CMOS process to fabricate the ASIC-NI and remove the need for a step-up convertor to generate a 12V source. However, using a high compliance voltage offers some compensating advantages, because it allows delivery of sufficient charge during a shorter duration stimulus pulse. Stimulus pulses that are relatively brief and high current incur fewer timing clashes, require less charge per phase to excite vestibular afferents [42] and are more effective at stimulating cochlear afferents when incorporated into pseudo-monophasic, cathodic-first stimulus paradigms [115].

As is evident in Figure 24 and Figure 25, MVP2A stimulator and the MVP2 yielded very similar outcomes during *in vivo* experiments. This is not surprising, because bench tests demonstrated that both systems deliver the same stimulus current waveforms. Results for both stimulators also exhibit aspects that exemplify challenges that merit additional research to optimize electrode placement and stimulus protocols. Responses to stimulation of left posterior SCC afferents consistently produced larger magnitude eye responses in the corresponding RALP direction, compared to stimulation targeting the left anterior and horizontal SCCs. This larger response is due to the greater selectivity with which current can be delivered to the posterior SCC's ampullary nerve branch (which is relatively far from other vestibular nerve branches) compared to the anterior and horizontal SCCs' nerve branches (which are very close to each other, constraining the magnitude of current pulses that can be delivered without spurious activation of the other afferents).

Responses also exhibit a pronounced excitation-inhibition asymmetry, with responses to excitatory stimuli (representing head rotation toward the implanted ear) being larger than responses to inhibitory stimuli (representing head rotation away from the implanted ear). Excitation-inhibition

asymmetry is a normal feature of many stages in the neural circuitry underlying the vestibulo-ocular reflex, most notably in vestibular afferent neurons' larger dynamic range for excitation (which can drive action potential rates from the ~100 spike/s baseline to more than 400 spike/s) compared to inhibition (which can only down-modulate firing rates to zero). This inherent asymmetry is exacerbated during prosthetic stimulation because down-modulation of the rate of exogenously applied stimulus pulses cannot drive afferent spike rates below a floor set by nonzero spontaneous discharge rates [121]. Methods currently under study to reduce this asymmetry include bilateral implantation [25,122], rehabilitation paradigms [123,124], "safe DC" stimulation [125] and concurrent modulation of stimulus pulse amplitude and frequency [42,44]. The ASIC-NI is especially well suited to enact the latter strategy, because its high compliance voltage allows delivery of brief, high current pulses.

This ASIC-NI provides a first step toward an MVP3 while maintaining compatibility with the existing MVP2 architecture. As ASIC-NI development continues, additional features can be integrated along with design changes that further reduce system size and power consumption. We envision an enhanced ASIC-NI that includes an integrated, on-chip microcontroller and an amplifier for neural response recording and measurement of electrode impedances *in vivo*. Addition of a telemetry unit, hermetic encapsulation, implantable battery and power management will be key components needed to complete a fully implantable system.

With the enhancements to MVP architecture described above, we can drive PFM stimulation for the utricle and saccule to encode GIA. Addition of the necessary hardware and firmware provides a means to sense and encode linear accelerations and changes in head orientation with respect to gravity. The MVP system can deliver stimuli via any pair of the 52 electrode contacts that the new electrode arrays offer. In conclusion, the overall prosthesis architecture greatly benefits from the ASIC-NI addition. The overall system architecture was successfully implemented to provide stimulation to the new electrode arrays to stimulate the utricle and saccule. Further discussion on this circuitry can be found in 4.4.

Chapter 3 Normal 3D Binocular Otolith Ocular Reflexes in the Chinchilla

3.1 Introduction

Successful implementation of prosthetic electrical stimulation of the utricle and saccule requires first understanding normal 3D otolith ocular reflex responses to static tilts and linear translations. Studies exploring the static tilt response report eye movements that partially correct for the degree of head tilt in lateral-eyed animals (fish, mice, rabbits, chinchillas) [38,126–128], frontal-eyed animals (primates) [129–131] and humans [132]. Lateral-eyed animals typically have a more robust tilt response compared to humans and other primates [7]. Findings indicate that the change in GIA during a static tilt about one axis elicits an ocular counter-roll in the direction compensatory for the axis of reorientation independent of the optic axis orientation (lateral- vs. frontal-eyed), ([126] for summary). Most published studies for lateral-eyed animals report ocular counter-roll responses about the roll/naso-occipital or pitch/interaural axes alone, leaving tilt responses about other axes unexplored.

Most studies of the tVOR in lateral-eyed animals, including rabbits [80], pigeons [77] and rats [79] focused on a limited range of head movements and primarily monocular recordings. Published results report very small changes in rotational eye position due to tVOR, typically $<2^\circ$ eye movement during peak accelerations ranging from 0.2-3 m/s^2 [79,80]. A gain for each component of recorded eye movements is conventionally described by (angular eye position)/(apparent tilt angle), where apparent tilt angle, θ , is the angle between earth-vertical and the net GIA vector during horizontal translations ($\theta = \arctan(a_{\text{linear}}/g)$). Baarsma and Collewijn reported gain of ~ 0.1 in rabbits up to 0.3 Hz, dropping to ~ 0.01 at 1 Hz [80]. Hess and Dieringer reported gain of 0.29 ± 0.1 for 0.1 Hz and a drop to 0.13 ± 0.03 gain at 1 Hz during sinusoidal translation in rats [79]. Both groups reported an increase in phase lag (eye movement peak following peak head acceleration magnitude) as frequency of motion increases.

Although the tVOR has been studied in lateral-eyed animals, the full 3D tVOR of lateral-eyed animals has not been characterized to the extent of tVOR research in frontal-eyed animals [78,89,90,129,130,133]. Frontal-eyed animals exhibit a strong horizontal eye velocity component during left-right translations (especially at frequencies >2 Hz) that is not seen in lateral-eyed animals [78,89,90,129,130,133]. This is attributed to frontal-eyed species' reliance on the tVOR to maintain image fixation on the high resolution central region of the retina. Lateral-eyed animals, such as the rabbit, rat, and chinchilla, have afoveate retinæ, meaning there is not a specialized region that must maintain fixation during faster movements such as a translation. The horizontal component of tVOR in lateral-eyed animals is minimal [77,79,80] and the vertical and torsional eye movements elicited from translation produce non-compensatory responses to the linear head movement and instead are compensatory for an apparent tilt angle. These findings support the 'apparent tilt' theory for interpretation of the tVOR in lateral-eyed animals [77,79,80], meaning the eye movement elicited by a translation is equivalent to that appropriate for an 'apparent static tilt' representing the head orientation that would yield the same GIA as the sum of translational acceleration and gravitational acceleration.

Tilt-translation ambiguity arises with how the brain processes the difference between tilt and translation since the influence of acceleration on the otoconial membrane, whether from linear acceleration or gravity, acts on the maculae in the same way. In frontal-eyed animals, hypotheses for central processing differentiation of tilt versus translation include the dynamics of the movement (i.e., a translation is generally brief, while a tilt is more likely to be prolonged), and input from the SCCs (during a tilt, the angular velocity at the beginning of the tilt provides an important input to the central processing of this data) [90,130,134–136]. However, the apparent tilt theory for lateral-eyed animals' tVOR implicitly assumes that there is no difference between tilt and a translation that results in an equivalent GIA with respect to the head. Note that normally, it is impossible to change tilt orientation without rotating the head, so one should distinguish between the act of tilting and the status of remaining steadily in a given tilted orientation.

The chinchilla, a lateral-eyed, afoveate animal with resting optic axes $\sim 55^\circ$ from the midsagittal plane, is an attractive species for vestibular stimulation research due to its relatively large and accessible labyrinth and the large body of literature on chinchilla vestibular anatomy and physiology. However, OORs have yet to be described in detail for this species, and the available data on 3D OOR of other lateral-eyed animals are insufficient to specify the relationship between observed OOR eye movements and the natural stimuli (i.e., head translation and/or tilt) that elicit them. Experiments to characterize binocular OOR in chinchillas and other lateral-eyed animals can provide insight toward central nervous system processing of vestibular input and how it differs in regard to the orientation of binocular optic axes, lack of foveal regions, and tilt versus translation elicited OOR.

Additionally, OOR characterization is required to determine whether eye movement responses map uniquely back to the head movements that elicit them. If every response pattern is unique and uniquely maps back to a single given head motion stimulus, then we can measure prosthetically-evoked eye movements and infer the natural head motion that would normally cause them. This back-projection from observed eye movement to inferred pattern of labyrinthine input is implicitly assumed during diagnosis of clinical disorders of the semicircular canals, because the 3D aVOR essentially drives eye movements equal and opposite the “perceived” head rotation that would normally elicit those eye movements [3,121]. In contrast, the mapping from head acceleration (or net GIA) to tVOR responses is complex, because the resulting eye movements are often disconjugate and a simple ‘eye equals negative head’ relationship like the aVOR does not occur for the tVOR, especially in lateral-eyed animals where for which tVOR responses are most readily understood as static tilt responses.

3.2 Methods

3.2.1 Surgical Methods

All experiments were performed using normal adult chinchillas (*C. lanigera*). Surgical

procedures were conducted in accordance with a protocol approved by the Johns Hopkins Animal Care and Use Committee, which is accredited by the Association for the Assessment and Accreditation of Laboratory Animal Care (AAALAC) International and consistent with European Community Directive 86/609/EEC. Under general anesthesia (isoflurane, 1.5%-5%), six adult chinchillas were fit with a head post to stabilize the head during experiments and a head cap using dental acrylic. Two scleral eye coils (design discussed in section 2.1.2.1) were implanted in each eye for 3D binocular tracking of eye movements. In each eye, two pockets were created under the conjunctiva at approximately orthogonal locations (superotemporal and anterosuperior/nasal side of the eye). Coil location was chosen to avoid injury to or restriction of extraocular muscles. Each coil was sutured to the sclera using polypropylene suture, the tightly twisted stainless steel leads of each coil were routed out of the orbit and subcutaneously to the head cap, then the conjunctiva was sutured closed with fast gut suture. Each animal recovered for 10-14 days before proceeding with experiments.

3.2.2 Eye Movement Recording

We recorded 3D binocular eye movements with a custom magnetic scleral coil system adapted from the methodology first described by Robinson [57]. All eye movements are reported in head coordinate frame (with the head tilted nose down $\sim 50^\circ$ to align the horizontal canals with Earth horizontal [137]) following the right-hand rule, where +X is to the front, +Y is out the left ear, and +Z is superior (as shown in Figure 28A). The new scleral coil system used for these experiments is described in section 2.1. In brief, alternating magnetic fields generated by 3 coil pairs, with each pair comprising two opposite faces of a cubic frame and operating at one of three different frequencies, which induces a voltage in the implanted scleral coils. After amplification and filtering, the induced scleral coil voltage from each of the four implanted scleral coils is sampled and demodulated in the digital domain using a field programmable gate array (FPGA) to determine the axis of each scleral coil in 3D with respect to the coil frame.

During experiments, the animal was head-fixed in a plastic cylindrical enclosure with the head centered in the middle of the coil frame and nose tilted down $\sim 50^\circ$ to align the horizontal canals parallel to Earth horizontal [137]. Before the motion paradigm began, we measured gains and offsets of the system. Gains (relative maximum voltage for each magnetic field) were measured by facing a non-implanted scleral coil directly into each of the three magnetic fields. Subsequently, the offsets for each implanted scleral coil were measured after connecting the animal's scleral coils to the system. All experiments were completed in total darkness to avoid visual suppression of the VOR; however, audible artifacts from the motion platform were present.

3.2.3 Motion Stimulus

We employed a six degree of freedom (DOF) motion platform (6DOF2000E, Moog, Inc.) to deliver linear accelerations and static whole-body tilts via custom software developed in C#. This platform allows translation along any 3D axis, and static tilt about any axis. Before beginning collection of data for normal tVOR and ocular counter roll, the motion platform was programmed to deliver 0.5, 1, and 2 Hz sinusoidal rotations about the Yaw, Pitch, Roll, LARP, and RALP axes at peak 20 and 30°/s. For comparison to an existing database of aVOR responses previously recorded from normal chinchillas [29,38], we used this measurement as a baseline to ensure the eyes were not tethered from the scleral eye coil surgery. After ensuring normal aVOR responses, data collection proceeded with translations and static tilts.

The motion platform's peak acceleration, velocity and position limits constrained our choice of translation and tilt stimuli. To collect tVOR during translations in the full 3D space, we programmed the motion platform to deliver 1 Hz sinusoidal translations along all of the axes illustrated in Figure 28. Each direction is shown in spherical coordinates, where azimuth θ ranges over $[-180, +180]$ and polar angle φ , which ranges over $[0, +180]$, is the polar angle as measured from the +Z (i.e., dorsal and superior) axis. In this coordinate system $(\theta, \varphi) = (0, +90)$ points anteriorly/nasal along +X; $(+90, +90)$ points left along +Y; and $(0, 0)$ points superiorly along +Z.

Note that as implied in Fig. 1, the chinchilla's head was pitched relative to the coil system so that the horizontal SCC canal plane was approximately Earth-horizontal at the outset of each session (i.e., the horizontal SCCs' axes were approximately earth-vertical and parallel to the +Z axis [$(\theta, \varphi) = (0, 0)$]). Sinusoidal translation peak acceleration was 1, 2, and 3 m/s^2 for translations in the Earth-horizontal plane (i.e., for $\varphi = 90$) and 2 m/s^2 for sagittal, coronal and oblique plane translations.

A frequency sweep of whole-body translations was conducted along the surge: front/back initially along the +X axis $(\theta, \varphi) = (0, +90)$ and lateral: left/right initially along the +Y axis $(\theta, \varphi) = (+90, 0)$. The motion platform's peak acceleration varied for different frequencies as shown in Table 3.

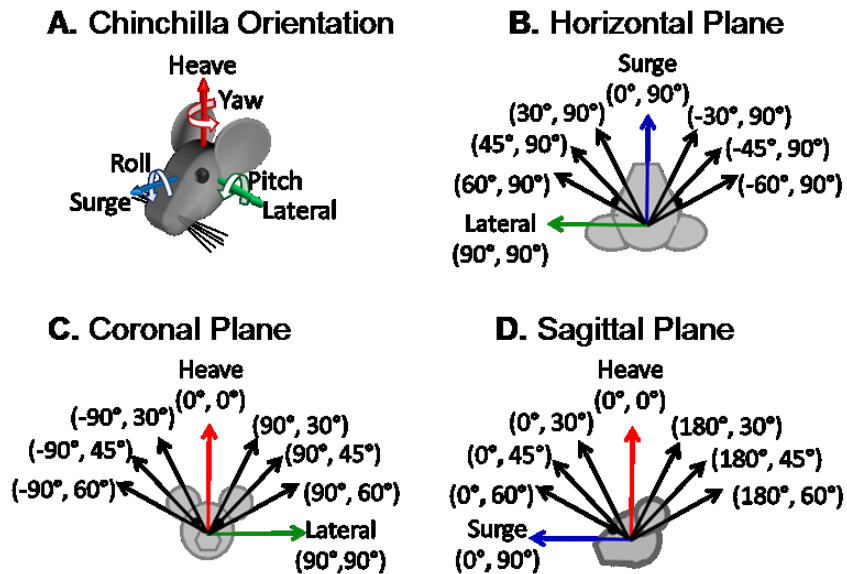


Figure 28. Axes of sinusoidal translations for characterization of the 3D translational vestibulo-ocular reflex. A. The chinchilla was oriented $\sim 50^\circ$ nose down to align the horizontal canal parallel with Earth horizontal [137]. The three cardinal translation axes, Lateral (interaural), Surge (fore-aft), and Heave (up-down), align with the rotational Roll, Pitch and Yaw axes respectively. Each arrow points in the positive translation direction and each curved arrow indicates a positive rotation. Sinusoidal translations at 1 Hz were completed along each axis in the horizontal plane (B), the coronal plane (C), and the sagittal plane (D). Axes angles are in spherical coordinates (θ, φ) , where $(0, +90)$ points toward +X, $(90, 90)$ points toward +Y, and $(0, 0)$ points toward +Z.

Frequency (Hz)	Peak Acceleration (m/s ²)
0.1	0.07
0.2	0.1, 0.2, 0.3
0.4	0.5, 1
0.5	1
0.6	1, 1.5
0.8	1, 2
1	1, 2, 3
2	1, 2, 3
3	1, 2, 3

Table 3. Frequency and peak acceleration of sinusoidal translations. Peak sinusoidal translational accelerations varied as a function of motion axis and frequency due to motion platform limitations.

Whole-body static tilts were completed for 40 sec duration about the 16 axes shown in Fig. 2. The axis of tilt is depicted using the right-hand rule, as the example arrow on the black ‘Right Ear Down’ vector illustrates. Due to angular position limitations of the motion platform, the maximum angle achievable for static tilt was 20° from Earth horizontal.

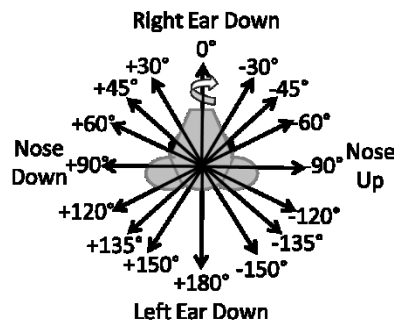


Figure 29. Axes of whole-body static tilts. Whole-body static tilt re-orientations were completed about these sixteen Earth-horizontal axes (via right-hand-rule rotations). All tilts were 20° from horizontal held for 40 s prior to a return to the starting orientation. The rotation to get to and return from the tilt orientation was 4°/s for 5 s duration.

3.2.4 Data Analysis

We developed a custom data analysis software package in Matlab (MathWorks, Natick, MA) that employs methods of rotational kinematics, methods previously described [84,85]. In brief, for each of the four scleral coils, the coil system demodulated the coil voltage into its 3 dominant frequency components, which represented the X, Y and Z components of the coil’s axis with respect to the field col frame. Data from the two scleral coils per eye was first mathematically

orthogonalized to account for variability in placement on the scleral surface [116]. For sinusoidal rotations and translations, the orthogonalized data was converted to a rotation vector and then to angular eye velocity vectors. Each binocular component of angular eye velocity (R_x , R_y , R_z , L_x , L_y , L_z) was fit with a single frequency discrete Fourier transform at the frequency of rotation or translation. The axis of eye velocity was determined based on the value of the eye velocity at peak positive acceleration defined by the right-hand rule. Example data analysis steps are shown in Figure 33 and are subsequently discussed in Results (section 3.3). For ocular-counter roll data, the average rotation vector for the final five seconds of the tilt was calculated and used to represent the final ocular counter-roll position, shown in Figure 31.

3.3 Results

The 3D binocular eye movements during angular rotations, whole-body static tilts, and 1 Hz translations along all axes in the horizontal, sagittal, and coronal planes were collected from six normal chinchillas. The frequency sweep data were collected from five normal chinchillas.

3.3.1 Angular Vestibulo-Ocular Reflex

Example aVOR results recorded from one chinchilla are shown in Figure 30A-C during 1 Hz rotations about the axis of each SCC with peak $20^\circ/s$. During yaw rotation about the Earth-vertical axis of the horizontal canals (Figure 30A), both eye position and eye velocity show primary yaw aVOR response, with compensatory eye velocity for the head velocity. The eye position returns to the starting position within two-three seconds after the yaw rotation ends. Figure 30B and C show binocular eye position and velocity first six cycles of trials rotation about the LARP and RALP axes. The direction of eye velocity is compensatory for the direction of head rotation, however the aVOR amplitude differs between the two eyes (as seen in all six animals) and differs from the findings previously reported, showing equal aVOR amplitude between the right and left eyes [29,38]. The previous experiments required reorientation of the animal with respect to gravity in

order to complete rotations about the LARP and RALP axes with an Earth-vertical motor, suggesting possible influences to the exhibited eye movements that were not seen for these data.

The axis of eye velocity recorded from all six chinchillas during 1 Hz sinusoidal rotations about each SCC's axis at peak 20°/s and 30°/s during a left-ward head rotation is illustrated in Figure 30D. Each axis was calculated by taking the single frequency discrete Fourier transform (DFT) of each component of eye velocity. Overall, the 3D axis of eye rotation is approximately aligned with the 3D axis of head rotation, as expected. However, an asymmetry between right and left eye velocity amplitude for LARP and RALP is seen in this image, with smaller eye velocities for right eye during LARP and for the left eye during RALP. This smaller amplitude caused greater variability in the axis. Although it is possible that this asymmetry is due to restriction from the scleral coils (e.g., if the right eye were mechanically restricted by the coil leads for rotations about its line of sight during LARP head rotation), the $\sim 9^\circ$ peak to peak positional range of, for example, the right eye during static tilts about the LARP axis was 3.5-fold larger than the $\sim 2.5^\circ$ range evident in Figure 30B, so the eye evidently is can at least move through that range of movement. An alternate interpretation is that during a head rotation about an Earth-horizontal LARP axis, VOR neural pathways are strengthened by a larger adaptive drive to keep left eye image slip minimized, whereas in the same condition, the right eye can afford to slip because images on the retina will only rotate rather than sliding off the retina entirely.

3.3.2 Ocular Counter-Roll Response to Static Tilts

Examples of the ocular counter-roll are shown in Figure 31; each tilted orientation at 20° from Earth horizontal was held for 40 second duration. Figure 31A shows an example from the left eye during left ear down static tilt. To plot this eye movement in 3D, as shown in Figure 31B, the average over the final five seconds of the ocular counter-roll for each component of eye movement was used to create a 3D vector to represent the final ocular counter-roll position. By the end of the 40 s tilt, it can safely be assumed that there are no influences of the angular rotation to achieve the

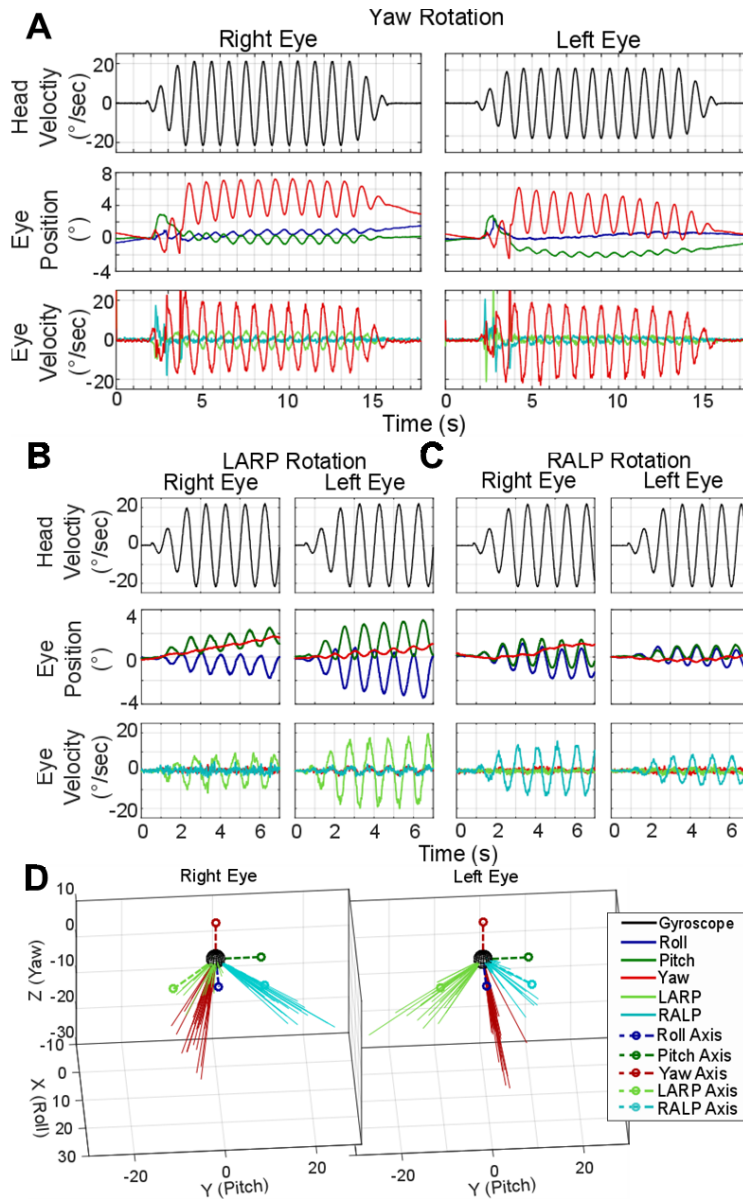


Figure 30. Normal chinchilla angular VOR. Angular vestibulo-ocular reflex results during 1 Hz, peak $20^{\circ}/\text{s}$ sinusoidal rotations about the left-horizontal/right horizontal (Yaw, panel **A**), left-anterior/right-posterior (LARP, panel **B**) and right-anterior/left-posterior (RALP, panel **C**) axes. **A**, **B** and **C** show example trials recorded in one chinchilla. The top row of each panel illustrates the head velocity about the indicated axis, as recorded from a six degree-of-freedom motion sensor. The second row shows recorded angular *eye position*, collected in head coordinates, yaw, pitch, and roll. The third row shows the angular *eye velocity* for each trial. Panel **D** illustrates the axis of eye velocity recorded during a left-ward head rotation for trials collected from all six chinchillas. For LARP (**B**) and RALP (**C**), an asymmetry in magnitude of eye position and velocity was seen. During LARP rotation, the left eye elicited a larger compensatory eye velocity while during RALP rotation, the right eye showed larger compensatory eye velocity. This is further illustrated by the difference in vector length in **D** between the right and left eyes for LARP and RALP. The smaller magnitude responses (right eye LARP and left eye RALP) showed greater variability in direction, while the larger responses (left eye LARP, right eye RALP, and binocular Yaw) are well aligned with the expected direction.

static reorientation based on the position traces shown in Figure 30A returning to starting position within 2-3 seconds of the end of the angular rotation. Figure 31C shows right and left eye position recorded during static tilts about seven Earth-horizontal axes. As the axis of the static tilt changes from left ear down to right ear down, the progression of the magnitude and direction of each component of eye movement changes to account for the change in GIA.

Figure 32 shows a summary of all ocular counter-roll responses measured from six chinchillas during 20° static tilts about the sixteen axes indicated in Figure 32C. The direction of static tilt is determined using the right-hand rule, as shown with the arrow on the solid black ‘Right Ear Down, 0°’ vector. Figure 32A and B show the 3D vector of ocular counter-roll for the right and left eye. An asymmetry is seen between the magnitude of the change in angular eye position of the right and left eye during tilts about axes aligned with the contralateral eye. For example, the *right* eye responses are larger in magnitude than the left for tilts about axes aligned with the *left* eye. Similarly, the *left* eye responses are larger in magnitude than the right eye for tilts about axes aligned with the *right* eye. This is further illustrated in Figure 32D, where the ratio of right/left eye ocular counter-roll position is plotted based on the tilt axis. These data show a ratio > 1 (right eye is larger) for tilt axes through the left eye and a ratio < 1 (left eye is larger) for the tilt axes aligned with the right eye. Tilts about the front-back and interaural axes show right and left eye responses with similar magnitudes.

Each component of eye movement from the data in Figure 32AB is plotted in Figure 32E. Any outliers larger than three times the interquartile range were removed for both D and E (< 11 of the 184 samples for each plot). During tilts that reorient the head via a negative roll from its starting orientation (i.e., bring the left ear down) the ocular counter-roll shows a positive roll-component for both eyes. In contrast, responses to tilts that bring the right ear down have a negative roll component. The polarity of the pitch component depends on whether the tilt axis moves the nose up or down. For pitch tilts that reorient the head in a negative pitch-tilt direction (nose up), the

ocular pitch component (in head coordinate frame) for both eyes is positive. Tilts that bring the nose down elicit a negative pitch eye movement.

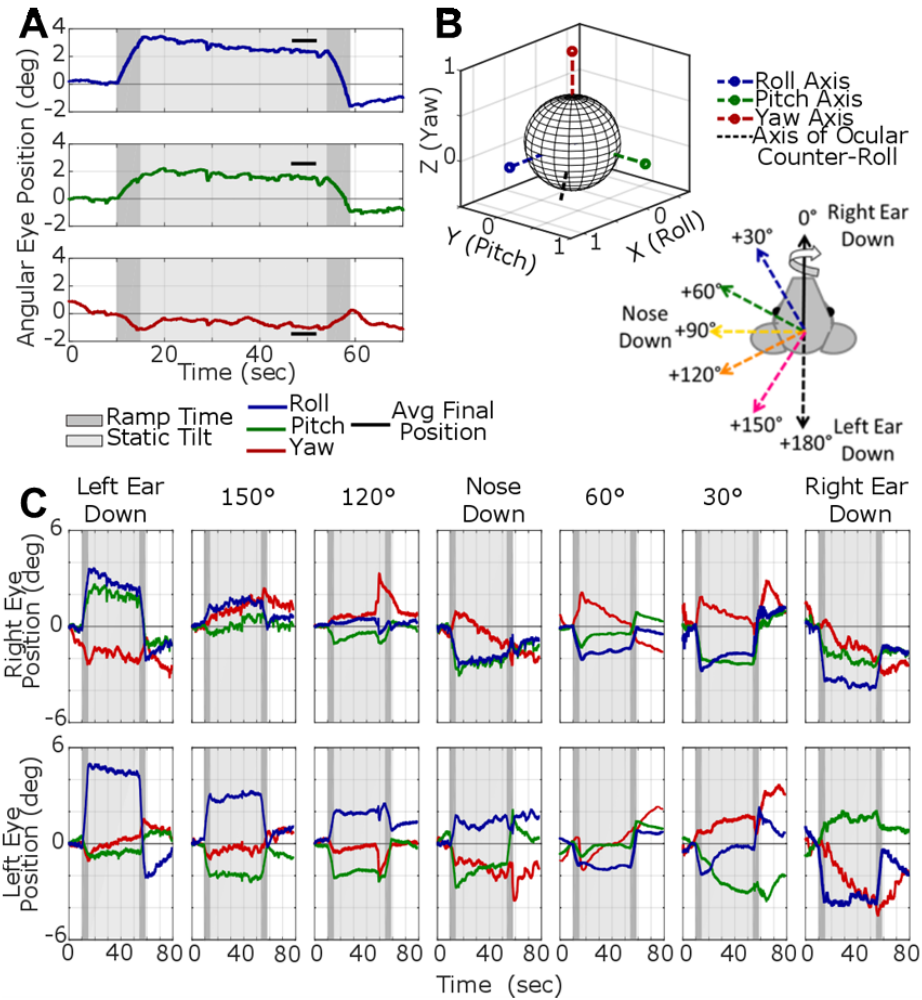


Figure 31. Example ocular counter-roll responses recorded during 20° from horizontal tilts. **A.** Example left eye position during a left ear down tilt. The time during the ~4°/s rotation to reach the static orientation is shaded in dark gray, and the time during the static tilt in light gray. The final ocular counter-roll position is calculated by averaging each component over the last five seconds in the tilted orientation, indicated by solid black lines near the eye movement traces. **B.** The final ocular counter-roll position can be plotted in 3D, shows with the black dashed line. **C.** Example ocular counter-roll responses during static tilts about seven of the sixteen different axes. The magnitude of each component of the ocular counter-roll data changes as the tilted orientation of the animal changes from left ear down to right ear down. Overall, the roll-component flips polarity moving from left to right ear down, as expected. Additionally, the pitch component moves from disconjugate at left ear down, to conjugate at nose down, and finally disconjugate again at right ear down. The yaw component shows greater variability throughout the trials, making it difficult to determine a meaningful interpretation of the yaw data from these examples.

These results support the compensatory nature of the ocular counter-roll response. For both eyes, the yaw-component of ocular counter-roll was smaller in amplitude than the pitch and roll for every axis of head tilt shown in Figure 32C. Note that this is the opposite of the finding reported previously for yaw head reorientations about an Earth-horizontal dorsoventral axis, which would be perpendicular to every axis shown in Figure 32C [38]. It is therefore apparent that the same head rotation about a given axis with respect to the head can yield different responses depending on whether the animal's starting orientation has that rotation axis Earth-vertical, Earth-horizontal, or somewhere in between. One must therefore exercise caution when comparing results measured using Earth-vertical rotators and 6DOF motion platforms.

A nonlinear mixed-effect statistical model of the static tilt data from five of the chinchillas (one was eliminated from the model due to an incomplete data set) was created to predict the ratio of the magnitude of right eye angular position over the magnitude of left eye angular position and six models were completed to predict each component of eye movement based on the tilt axis. All models used the fixed effect (independent variable) of the tilt axis and due to the small sample size, a random effect of chinchilla ID number (see [138] for review on random effects). Each nonlinear model was fit using the equation $y=a*\cos(b*tiltAxis+c)+d$ function. Parameters a, b, c, and d are estimated by the nonlinear fit, y is the predicted value (component of eye movement or the ratio of eye position magnitudes), and tiltAxis is the theta of the axis about which the tilt occurred. Values for the root mean square error (RMSE) for each fit were all ≤ 2.53 . The results of the model are listed in Table 5 in the Appendix and plotted atop the data in red in Figure 32DE.

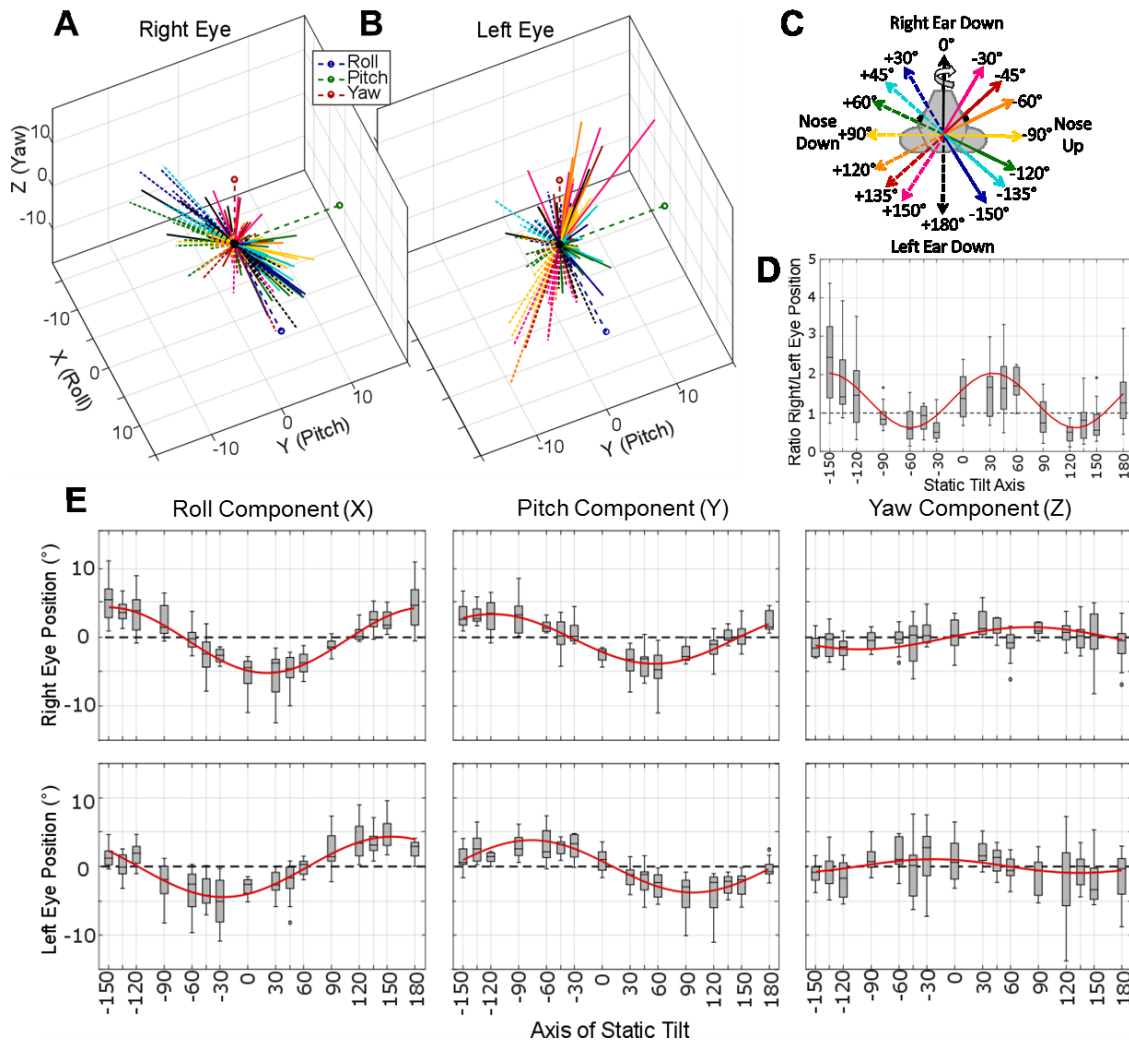


Figure 32. Ocular counter-roll responses recorded from six chinchillas during static tilts. Each animal was tilted 20° from horizontal about the sixteen indicated axes in panel C. Each tilt was held for 40 seconds and the final position of the ocular counter roll, which is plotted in A and B, was calculated by averaging over the last 5 second of the eye movement, as demonstrated in Figure 31A. Each vector is color coded based on the legend in panel C. An asymmetry is seen between the magnitude of the change in angular eye position of the right and left eye during tilts with a larger change in angular eye position during tilts about axes aligned with the contralateral eye. Tilts about the naso-occipital and interaural axes elicit ocular counter-rolls in the left and right eye of similar magnitude. To further illustrate this asymmetry, a boxplot of the ratio of right/left eye ocular counter-roll position is shown in panel D. Component-wise results from all static tilts in the six animals is shown in panel E. Any outliers larger than three times the interquartile range were removed for both D and E (fewer than 11 of 184 samples were removed for each plot). Nonlinear mixed effect models were created to predict each component of eye movement and the ratio of right eye/left eye magnitude based on the tilt axis with fixed effect of tilt axis and random effect of chinchilla ID number. The fits are shown in red, with $RMSE \leq 2.53$ for all fits. All fit parameters are detailed in Table 5. Each axis of static tilt has sample number $n \geq 11$.

3.3.3 Translational VOR Response to Linear Translations

Example data traces of recorded tVOR eye movements are shown in Figure 33. These representative right and left eye position traces recorded from one chinchilla were collected during translation along the following axes: lateral (Earth-horizontal interaural), surge (Earth-horizontal fore-aft), oblique approximately along the left eye's resting line of sight (+45°), and oblique approximately along the right eye's resting line of sight (-45°). Motion platform *acceleration* and each component of eye 3D *angular position*, X (Roll), Y (Pitch), and Z (Yaw) are shown in Figure 33A-D, respectively. Aside from analog filtering of the scleral coil signal before demodulation, these data represent the unfiltered rotation vector of eye position showing the ability of the low-noise scleral coil system to capture the small eye movements elicited during translations. The angular eye velocity for the Lateral example is shown in Figure 33EF with the single frequency discrete Fourier transform (DFT), used to fit each component of the angular eye velocity for both eyes at the frequency of the sinusoidal translation. A 3D vector of this fit represents the cloud of points (angular velocity at each time point during the trial) shown in Figure 33GH. This vector represents the axis of angular eye velocity during the lateral translation.

Binocular 3D tVOR results were recorded during sinusoidal translations at frequencies ranging from 0.2-3 Hz with the corresponding peak accelerations listed in Table 3 and are shown in Figure 34. Gain was defined as angular eye position (in degrees) divided by the apparent tilt angle (defined by Baarsma and Collewijn as $\text{apparent tilt} = \arctan(\text{acceleration}/\text{gravity})$ [80]). Phase was calculated as the difference between peak head acceleration and peak eye movement of the single frequency DFT, where a negative phase indicates eye movement lags head movement. Resultant tVOR during lateral translations (Figure 34A) shows overall low-pass filter dynamics for all three components of eye position with a steep drop in gain as frequency extended beyond 1 Hz. Phase comparison between the two eyes reveals conjugate roll and yaw responses for all frequencies. Roll and pitch directions are compensatory for the change in gravity that would be sensed about the apparent tilt axis associated with the translation direction. The pitch component was disconjugate

(i.e., 180° out of phase for the two eyes) at all frequencies, supporting apparent tilt theory where a lateral translation follows right ear down apparent tilt. With a right ear down tilt, the right eye is brought closer to the ground, and thus should pitch up, while the opposite is true for the left eye.

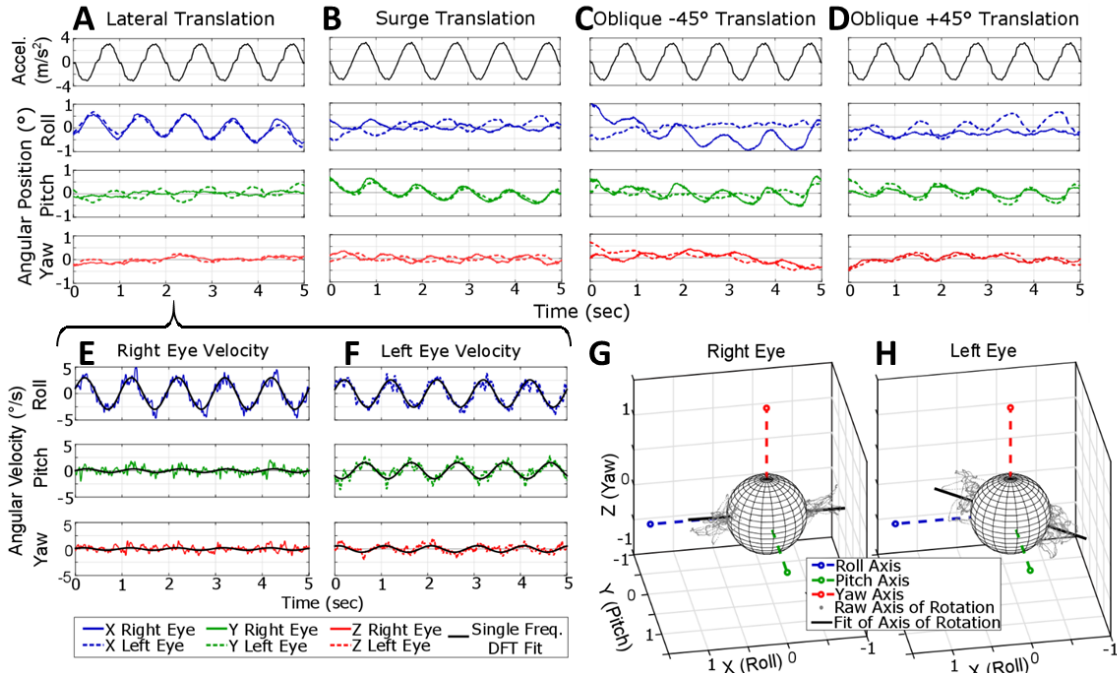


Figure 33. Example binocular tvOR position and velocity traces during translations. Eye position traces from one chinchilla recorded during translations along **A** lateral (interaural), **B** surge (fore-aft), **C** 45°, approximately along the right eye’s resting line of sight, and **D**. +45°, approximately along the left eye’s resting line of sight. Right and left eye responses (solid and dashed lines, respectively) are shown with no post-processing filtering, illustrating the capability of the system to record the small tvOR eye movements. The Lateral translation (**A**) elicits a primarily conjugate roll eye movement, whereas surge translation (**B**) elicits conjugate pitch and disconjugate roll. During oblique translations (**C** and **D**), the eye along which the animal is translating has a larger magnitude than the opposite eye. The eye position for the lateral translation in **A** can be converted to angular velocity, shown in **E** and **F**. Each component of the angular velocity is fit with a single frequency discrete Fourier transform (DFT) at the frequency of the sinusoidal translation, 1 Hz in this case. The X (roll), Y (pitch), and Z (yaw) components of the eye velocity plotted in 3D over time are shown in **G** and **H** as a cloud of gray points. These points represent the axis of angular eye velocity at each point in time throughout the trial. This cloud of points can be summarized to show the axis of angular eye velocity with the DFT fit, shown as the black line in **G** and **H**.

Figure 34B shows the frequency sweep results from surge (fore-aft) translations at frequencies from 0.2-3 Hz. During the forward acceleration, the apparent nose-up tilt should elicit conjugate positive pitch, which is seen as the phase between both eyes remains conjugate and approximately in phase with the head acceleration. The two eyes have disconjugate yaw and roll for frequencies

above 0.2 Hz, consistent with the vergence eye movement one might envision a bull makes as it pitches its head down in preparation for a charge and directs its gaze forward. The roll component is compensatory in direction for an apparent nose-up tilt (showing a positive roll in the right eye and negative in the left during forward translations, i.e., both eyes roll away from the nose).

Although gain for lateral-eyed animals tVOR has been historically defined as shown in Figure 34, the low-pass filter nature is simply due to the somewhat arbitrary choice of numerator and quotient to define a gain. Comparing (eye rotational velocity / head translational acceleration) and (eye rotational velocity / head translational velocity), as shown in Figure 35, illustrates how the physiologic system appears to have a high-pass dynamics when the stimulus of interest is chosen to be head translational velocity (bottom plot in Figure 35), suggesting that the lateral tVOR eye velocity elicits a higher sensitivity to head velocity at higher frequencies. Data from Rhesus monkeys, reported by Angelaki in Fig. 5 of [129], are shown atop chinchilla data in Figure 35 for comparison. The gain responses for monkey torsional and chinchilla roll show similar dynamics for all three plots, while when comparing monkey horizontal to chinchilla yaw, a much larger difference is seen with monkey gains (or sensitivities) compared to chinchillas for eye velocity re-head acceleration velocity. This difference is attributed to the drive for monkeys (and other frontal-eyed animals and humans that have foveae) to maintain fixation of the image on the retina. Therefore, a large yaw component in both eyes is seen during left-right translations.

Figure 36 shows tVOR data elicited during 1 Hz sinusoidal translations along eight axes in the horizontal plane from six chinchillas. Each translation was completed with peak 2 or 3 m/s² acceleration. The 3D vector of eye velocity at the instant of the peak positive acceleration (in the direction of the arrows in Figure 36C) is represented by a 3D vector in Figure 36A for the right and left eyes. The corresponding vectors at the peak *negative* head acceleration are simply the inverse of the plotted DFT fit for eye velocity during positive peak acceleration and are not pictured. Translations along axes approximately aligned with the *left* eye show an apparent asymmetry in the magnitude of left versus right eye velocities, with larger magnitudes in the *left* eye. Similarly,

during translations along axes approximately aligned with the *right* eye, the magnitude of eye velocity in the *right* eye is larger than that elicited in the left (Figure 36A). Figure 36E shows the ratio of right eye velocity magnitude/left eye velocity magnitude to further illustrate this asymmetry between the velocity magnitudes of each eye.

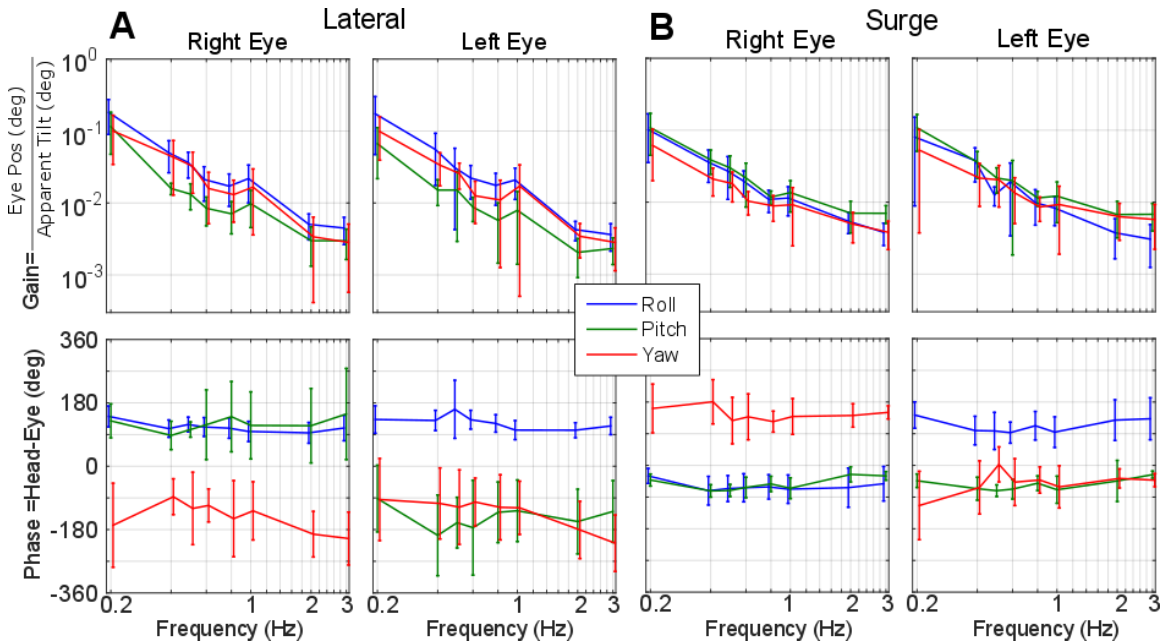


Figure 34. Gain and phase of the chinchilla tVOR during lateral and surge translations. Frequency sweep results during lateral (A) and surge translations (B) at 0.2-3 Hz recorded from five normal chinchillas. Gain is reported as the position of angular eye position in degrees divided by the apparent tilt of the gravitation vector due to the linear acceleration (apparent tilt = $\arctan(\text{acceleration}/\text{gravity})$) and plotted on a log-log scale. Steady state sinusoidal phase was calculated as the difference between peak head position and peak eye position of the single frequency discrete Fourier fits for each component of eye movement. Negative phase indicates eye position lags head acceleration. Lateral translations elicit a roll component of tVOR with a gain around 0.2; with all gains decreasing as frequency increases. The roll component leads head acceleration by 90° while yaw lags the head by -90° to -180° . The pitch components between both eyes are disconjugate (the phases of the right and left eye are $\sim 180^\circ$ out of phase, meaning the two eyes are not moving in the same direction during the head movement). Surge translations elicit approximately equal roll and pitch gain at low frequencies, showing a decline of all gains as frequency increased. Phase values indicate disconjugate yaw and roll components while pitch was conjugate throughout all frequencies.

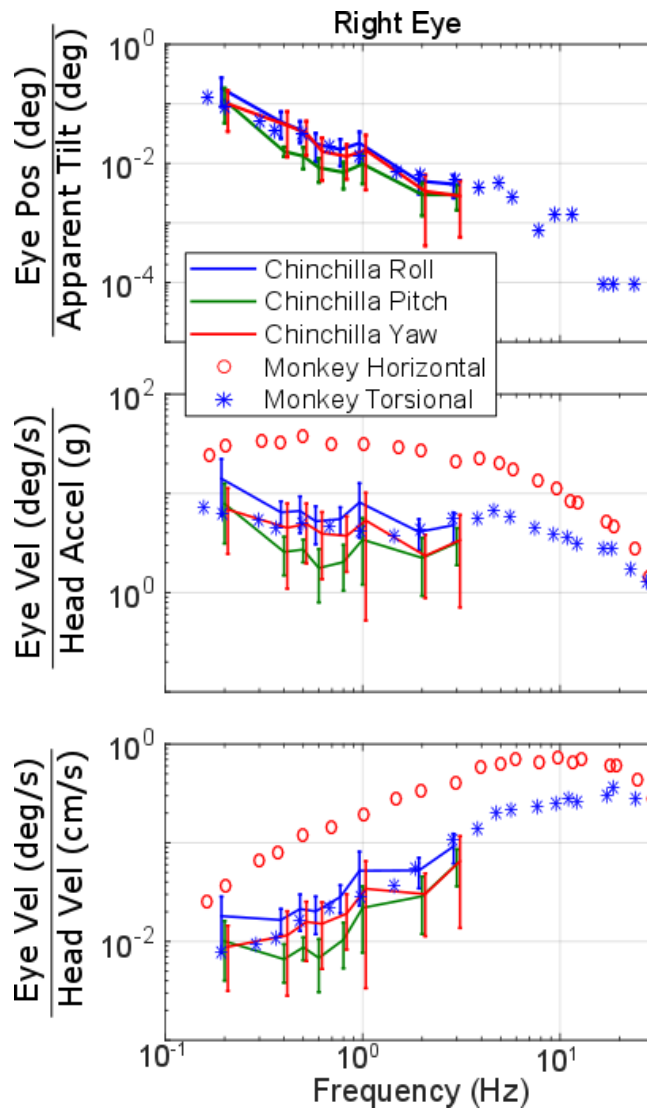


Figure 35. Comparison of monkey and chinchilla tVOR frequency response during lateral translation. Gain or sensitivity calculated in three different ways for right eye lateral translations. Top shows angular eye position (deg) divided by apparent tilt angle ($\arctan(\text{head acceleration}/\text{gravity})$). Middle shows eye velocity (deg/s) divided by head acceleration ($g=981 \text{ cm/s}^2$). And the bottom shows eye velocity (deg/s) divided by head velocity (cm/s). Data collected from Fig. 5 in Angelaki [129] shows the equivalent data recorded in monkeys, where the monkey horizontal (red circles) is equivalent to our chinchilla yaw (red lines) and monkey torsional (blue *) is equivalent to our chinchilla roll (blue lines). Note the similarity the roll/torsional components between species. However, the monkey horizontal response is much more robust than the chinchilla, a common difference seen between frontal and lateral-eyed animals.

Normalized data are shown in Figure 36B to illustrate the spread of direction of eye movements from translations in the horizontal plane. Additionally, the plots in Figure 36D show eye velocity components for each θ of translation. As the direction of translation changes, the axis

of eye velocity response changes systematically in a way that best fits the expected response to an apparent tilt rather than the response one might expect if an animal were trying to minimize retinal slip of an Earth-stationary visible target near the eye and along the eye's line of sight at the outset of head motion. The two eyes maintain a conjugate roll response during translations along the lateral (interaural) axis, in addition to when moving about the left and right eyes (+60, +45, +30 and -30, -45, -60 respectively), as might be expected if the stimulus is interpreted as an apparent head tilt. However, during surge (0°), disconjugacy is evident, with a positive roll in the right eye and negative roll in the left eye. The yaw component of eye movement is not offer compensatory direction of eye movement to the direction head movement (where compensatory would provide an eye movement to counteract the head movement and stabilize vision). Instead, the yaw component of eye movement tends to move in the direction of the translation (i.e. a left-ward translation elicits a binocular left-ward yaw eye velocity).

A nonlinear mixed effect statistical model was created to fit each component of eye movement, with fixed effects including translation amplitude and translation direction and a random effect of chinchilla ID number. The model was based on the nonlinear equation $y = a * \text{TranslationAmp} * \cos(b * \text{tiltAxis} + c) + d$. Where a, b, c, and d are model variables for the fit, TranslationAmp is the amplitude of the translation in m/s^2 and tiltAxis is the theta of the axis about which the static tilt occurred in degrees. An additional model was created to predict the ratio of right eye velocity magnitude/left eye velocity magnitude based on this same equation, fixed effects, and random effect. Model results are plotted atop the boxplots in Figure 36D and E for each component of eye movement and the ratio of right/left eye velocities respectively. All models created for the horizontal plane translations had a root mean squared-error (RMSE) ≤ 0.74 . The fit parameters can be found in Table 5 in the Appendix.

Similar data were collected for translations along axes in the *coronal* (Figure 37) and sagittal (Figure 38) planes. Figure 37 shows the tVOR during 1 Hz sinusoidal translations at peak $2 m/s^2$ along eight axes in the coronal plane. The coronal plane tVOR, Figure 37A shows an inequality

between left and right eye velocities, similar to that seen in Figure 36AE. Translations along axes approximately aligned with the *right* eye elicit binocular responses with larger eye velocity magnitudes in the *right* eye. Comparatively, translations along axes approximately aligned with the *left* eye elicit responses with larger magnitudes in the *left* eye. This is further illustrated by the boxplot in Figure 37E, showing the ratio of right eye/left eye velocity magnitudes. Figure 37B shows the normalized data to better visual direction-specific characteristics related to each translation direction. The boxplot in Figure 37D (note, all outliers greater than three times the interquartile range were removed for Figure 37DE) shows conjugate roll responses when the translation component along the y-axis is largest. Additionally, when translation in the z-axis dominates, i.e. $(-90^\circ, 30^\circ)$, $(0^\circ, 0^\circ)$, and $(90^\circ, 30^\circ)$, the roll component becomes disconjugate. The pitch component of both eyes maintains conjugacy for all head translational movements except for lateral. The yaw component is more variable and smaller in amplitude than the roll and pitch.

Figure 38 illustrates the tVOR elicited by 1 Hz sinusoidal whole-body translations at peak 2 m/s^2 along eight axes in the sagittal plane. The data in Figure 38A show the right and left eye tVOR eye velocities elicited by the corresponding translations shown in Figure 38C. Translations along these axes elicit binocular eye that are approximately equal between the two eyes. Figure 38B shows the normalized eye velocity vectors to facilitate visualization of the directional differences between the left and right eye tVOR which is further illustrated by the component-wise plots shown in Figure 38D. All outliers greater than three times the interquartile range were removed for Figure 38DE. Translations in the sagittal plane elicit disconjugate roll and yaw components and conjugate pitch. Roll and pitch components are compensatory for the apparent tilt axis instead of the direction to maintain visual acuity during the translational acceleration. The data from both coronal and sagittal plane translations support the previously mentioned apparent tilt theory [77,79,80].

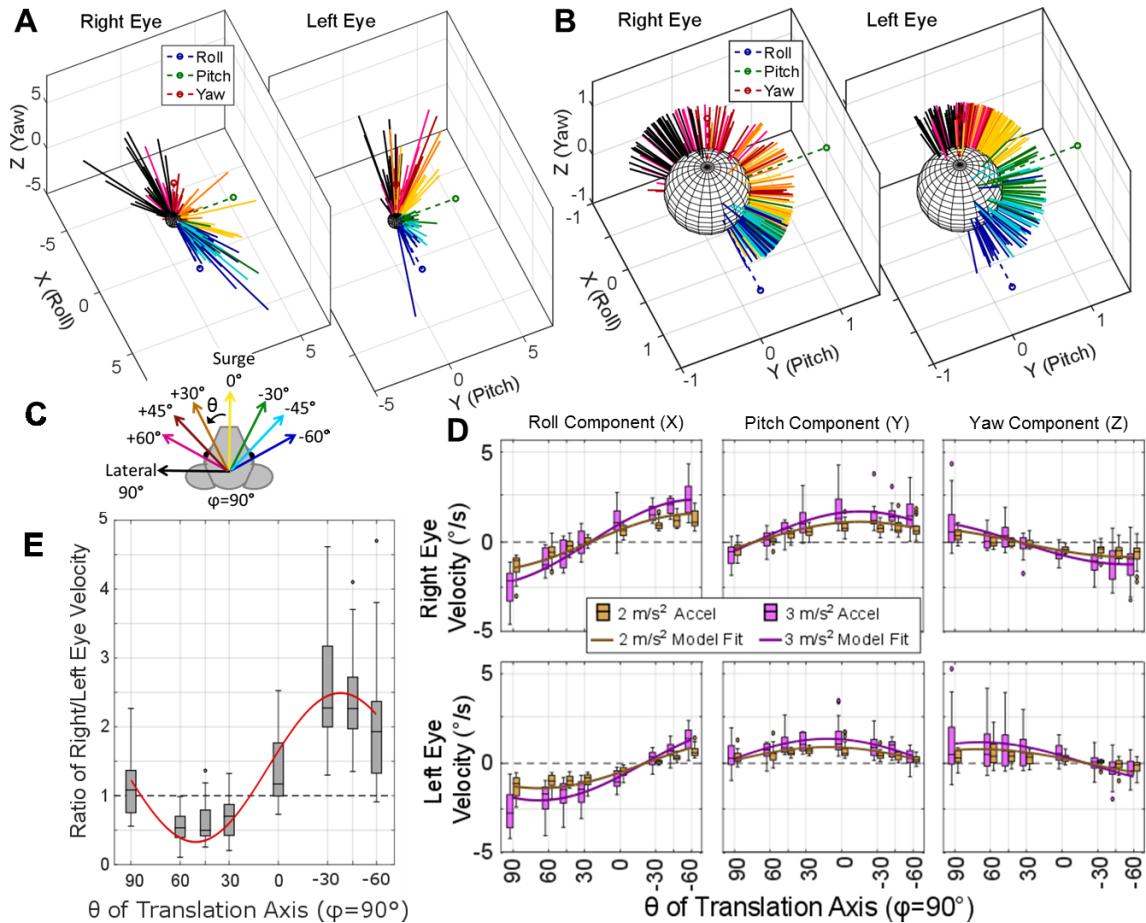


Figure 36. Translational VOR elicited during translations along axes in the *horizontal plane*. 3D axis of right and left eye velocity recorded from six chinchillas during translations along eight axes in the horizontal plane is illustrated in panel **A**, with the normalized vectors shown in **B**. Each vector represents the single frequency discrete Fourier transform fit of the eye velocities elicited during the positive peak of acceleration of a 1 Hz sinusoidal translation in the horizontal plane ($\varphi=90^\circ$) with peak 2 or 3 m/s². The color of the vector indicates the theta of the translation axis and the peak positive acceleration is in the direction of the arrows, both illustrated in panel **C** (all axes in Earth-horizontal plane so $\varphi=90^\circ$). Translations along axes approximately aligned with the *right eye*'s resting line of sight ($\theta=-30^\circ, -45^\circ, -60^\circ$) produce a larger magnitude eye movement in the *right eye* than the left. Conversely, translations along axes approximately aligned with the *left eye* ($\theta=+60^\circ, +45^\circ, +30^\circ$) elicit larger eye velocities from the *left eye*. This is further emphasized in **E**, where the ratio of right/left eye velocity is shown. The boxplots in **D** show component-wise responses grouped by θ for the eye movements elicited by both 2 m/s² (brown) and 3 m/s² (purple). Outliers greater than three times the interquartile range were removed for **D** and **E** (fewer than 16 of 257 samples were removed for each plot). Nonlinear mixed effect models were created to predict each component of eye movement and the ratio of right eye/left eye magnitude based on the magnitude of translation and the theta of the translation axis with a random effect of chinchilla ID number. The fits for each component of eye movement during 2 and 3 m/s² translations are shown in brown and purple in **D** and the fit for the ratio of right/left eye velocity is shown in red in **E**. All model results had $RMSE \leq 0.74$. All fit parameters are detailed in Table 5 in the Appendix. Each axis of translation for each amplitude (i.e. each individual box and whisker plot has $n \geq 11$).

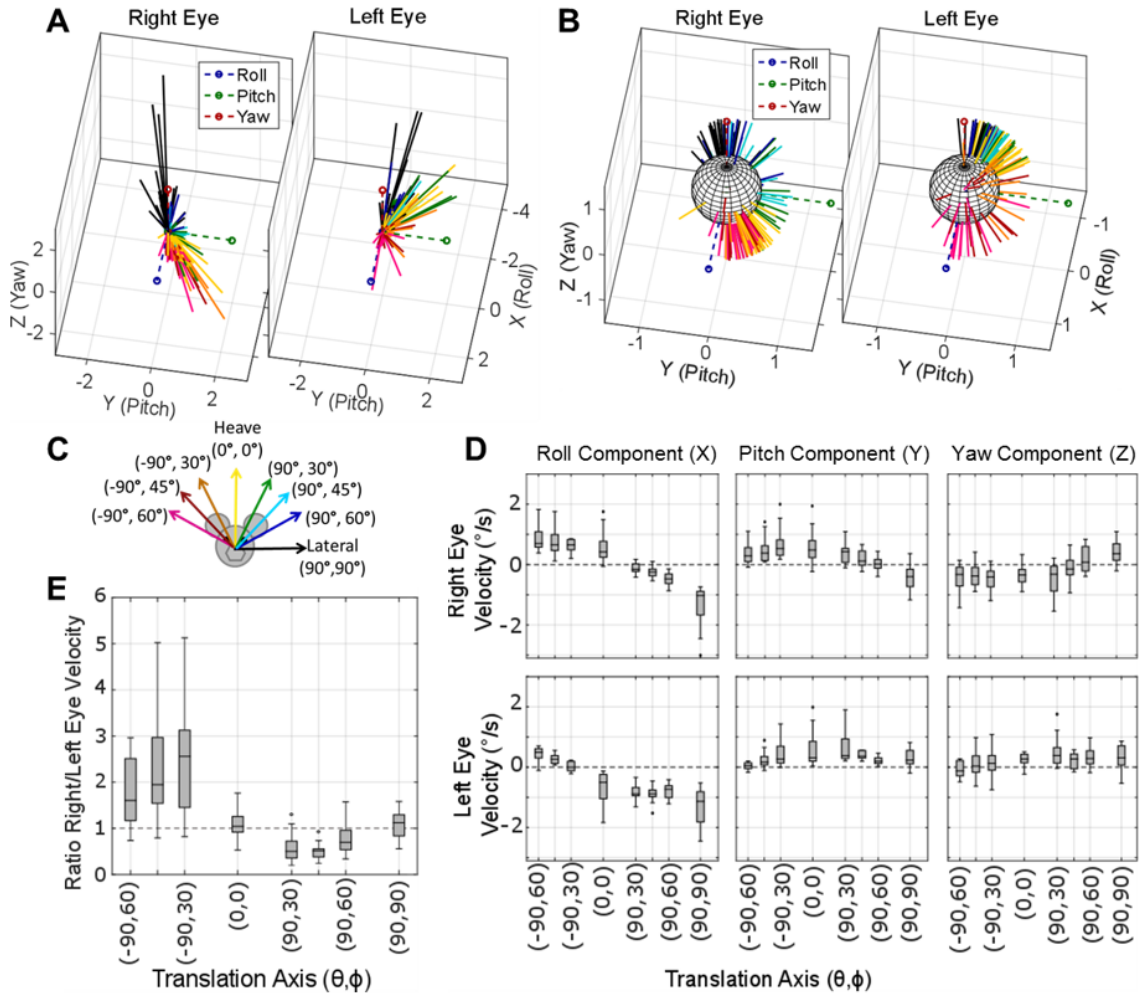


Figure 37. Translational VOR elicited during translations along axes in the coronal plane. Binocular 3D eye velocities recorded from six chinchillas, elicited during 1 Hz sinusoidal translations in the coronal plane with a 2 m/s^2 peak acceleration. The color of each vector indicates the translation direction, illustrated in C. Panel A shows the binocular axes of eye velocity; normalized vectors shown in B to better visualize the spatial spread for each translation direction. In A, an asymmetry between the right and left eye velocity magnitude is seen, similar to that seen in Figure 36A, where each eye's velocity is greatest during translations along axes approximately aligned with the ipsilateral eye. The boxplot in E further emphasizes this point, showing the ratio of right eye/left eye velocity. Translations oriented along the quadrant of the *right* eye (pink, red, orange in AB) elicit a larger *right* eye velocity than left (ratio > 1 in E). Translations oriented along the quadrant of the *left* eye (green, light blue, dark blue in AB) elicit a larger *left* eye velocity than right (ratio < 1 in E). The boxplot in D shows component-wise eye velocities. During coronal plane translations, the eyes generally show conjugacy in all three components, except during heave ($0^\circ, 0^\circ$) and lateral ($90^\circ, 90^\circ$) movements. All outliers larger than three times the interquartile range for D and E were removed (fewer than 13 of 131 samples were removed for each plot). Each box for each axis has samples $n \geq 14$.

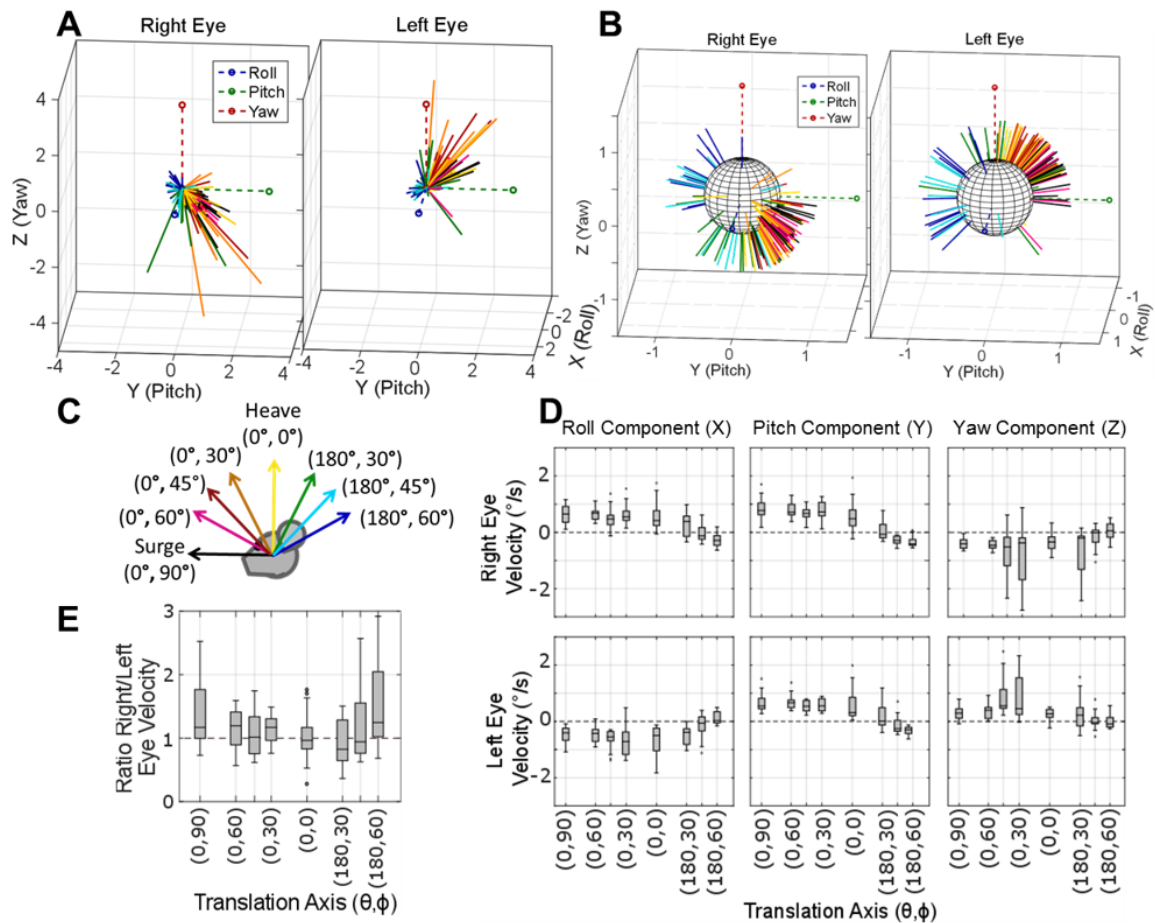


Figure 38. Translational VOR elicited during translations along axes in the *sagittal* plane. Axis of eye velocity recorded from six chinchillas during 1 Hz sinusoidal translations along 8 axes in the sagittal plane with peak 2 m/s^2 acceleration shown in panel C. Panel A shows the axes of the right and left eyes which have larger magnitudes for translations toward the front of the animals (black, pink, red, orange) than toward the back of the animal (green, light blue, dark blue). A boxplot of the ratio of right eye/left eye velocity (E) illustrates that the two eyes rotate at approximately the same velocity for translations in all the directions. The normalized data are shown in B to visualize the spatial spread of the sagittal plane tVOR. The boxplot in D shows component-wise eye velocity for each axis of translation, illustrating that the two eyes remain primarily disconjugate in roll and yaw, and conjugate in pitch. All outliers larger than three times the interquartile range for D and E were removed (fewer than 6 of 131 samples were removed for each plot). Each box plot for each axis has samples $n \geq 13$.

3.3.4 Tilt-Translation Comparison

To compare ocular responses elicited by reorientations due to static tilts and those driven by translation, the tVOR data can be interpreted according to the ‘apparent tilt’ axis (Figure 39B) instead of the translation axis (Figure 39A). For example, a leftward acceleration along the lateral (interaural) axis, causes a deflection of the otoconial mass to the right, which is similar to the otoconial deflection during a right ear down tilt in the Earth’s gravitational field. Even though these

two conditions differ (because the action of tilting necessarily involves a head rotation and because the net GIA's magnitude is larger during a pure interaural translation than when the head is stationary in some tilted orientation), the concept of apparent tilt is both an intuitive heuristic and a reasonably well explains tVOR responses of lateral-eyed animals [77,79,80]. Baarsma and Collewijn called this "perceived tilt" [80], but we use "apparent tilt" to avoid implying that the measured responses require conscious perception. In fact, tilt perception and tilt-driven ocular responses are not identical; Merfeld *et al.* showed tilt perception is largely driven by SCC sensation during a tilt reorientation [135].

The magnitude of change in eye position during the static tilts described was larger than the magnitude of eye velocity during translation because the temporal dynamics and amplitude of the 1 Hz sinusoidal translation were quite different from a 40 second whole-body static tilt. Equipment limitations prevent a linear translation of duration similar to the duration of the static tilt, so I direct comparison between tilt and translation is difficult. Therefore, to eliminate the big difference between eye movement magnitudes elicited from tilts versus translations, the ratio of the right eye/left eye magnitude was used. This ratio illustrates any common patterns in magnitude relationships between the right and left eyes. Figure 39C shows the ratio of right/left eye movements in response to tilts (right eye position/left eye position) and translations (right eye velocity/left eye velocity, with the translation axis adjusted to indicate axis of 'apparent tilt') from all six chinchillas, illustrating a larger magnitude of eye movement in one eye during tilts (or apparent tilts from a translation) about axes approximately aligned with the contralateral eye. The direction of ocular counter-roll and tVOR were compared after normalization and after reparameterizing translation axes as apparent tilt axes. Figure 39D shows each normalized component of binocular eye movements (angular eye position during static tilts, angular eye velocity for tVOR), illustrating obvious similarities between the direction of eye movements elicited by a static tilt and the corresponding linear translation.

A nonlinear mixed effect model was created to forward-predict each component of eye movement (all root mean squared error (RMSE) $\leq 0.37^\circ$) and the ratio of right/left eye movement (RMSE=0.64 $^\circ$) using fixed effects of tilt axis and type of stimulus (static tilt or translation), where axis for the translation files is the apparent tilt axis for the translation. A random effect of chinchilla ID number is also used due to the small sample size (n=6 chinchillas), see [138] for a review on mixed-effect models. The nonlinear model was fit to the following formula: $y = (a \cdot \cos(b \cdot \text{TiltAxis} + c) + d) + (e \cdot \text{TypeOfStimulus})$, where a, b, c, d, and e are all fit parameters for the model, TiltAxis is the theta of the axis about which each tilt (or ‘apparent tilt’), and TypeOfStimulus was a binary value indicating whether the data were collected during a tilt or translation paradigm. The parameters for the fit for each normalized component of eye movement are listed in Table 6 in the Appendix. All fits are shown in red in Figure 39CD. A two-way ANOVA between the predicted data from this model using type of stimulus as a fixed effect and a similar model without the (e*TypeOfStimulus) fixed effect was completed to determine the significance of the type of stimulus. The ANOVA for all components of eye movements and ratio of right/left eye movement magnitudes returned F-statistics ≤ 0.03 with all p-values ≥ 0.86 , suggesting no detectable difference with fixed effect of type of stimulus (tilt or translation) for each normalized component of eye movement. This implies that type of stimulus (tilt or translation) did not play a significant role in creating the models.

3.3.5 Reverse Model: Predicting Tilt Axis from Ocular Counter-Roll

To enable use of eye movement responses to infer the direction of the static tilt head orientation stimulus, a reverse model was created using the data presented above. Knowing a cosine relationship exists to relate each component of ocular counter-roll to the tilt axis and magnitude (Figure 39CD), the reverse model should use the arccosine to predict tilt axis from each individual component of ocular counter-roll. However, a cosine does not offer a one-to-one relationship between the input and output, meaning two different tilt axes can produce the same value for one

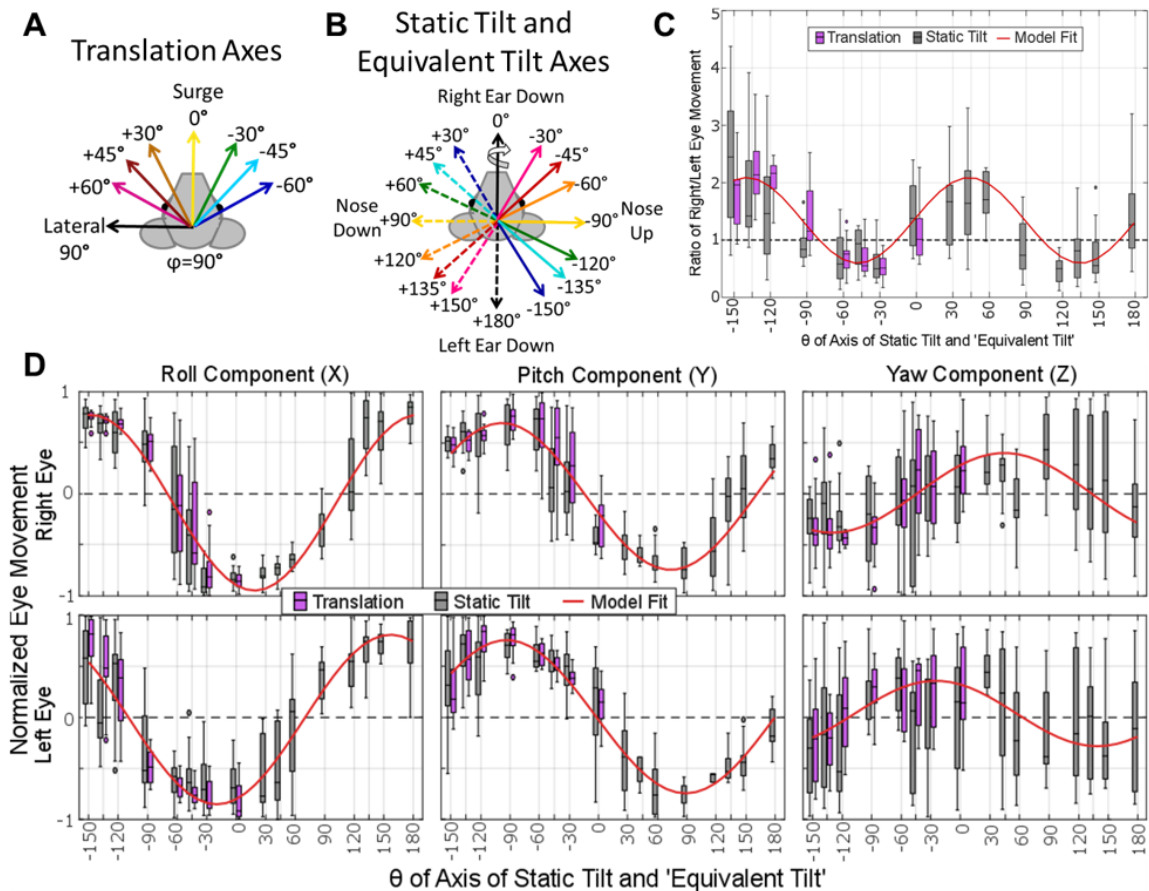


Figure 39. Comparison of tilt versus translation eye movement data. To compare changes in eye position elicited during static tilts to the axis of eye velocity during translations, the axes of translation (shown in **A**) can be converted to apparent tilt axes (**B**). The color and style of each line in **A** corresponds to the apparent tilt axis of the same color and style in **B**. For example, a surge acceleration toward the front (solid yellow line at 0° in **A**) is apparent to a tilt axis about the solid yellow at -90° , nose up in **B**. After adjusting the translation axes, we accounted for difference in the magnitude of eye movements between the two groups by taking the ratio of right eye/left eye magnitude shown in **C** and by normalizing the data, shown in **D**. Panel **C** illustrates a similar pattern for tilts and translations with larger magnitude of eye movement elicited in the eye that is contralateral to the axis of the tilt (i.e. tilts about the left eye elicit larger right eye magnitudes of ocular counter-roll and vice versa). To compare the direction of eye movements elicited from translations versus tilts, the normalized components for each case are shown in **D**, where the direction of eye movement is similar for each component between tilts and translations. Outliers larger than 1.5 times the interquartile ranger were removed (fewer than 14 of 441 samples were removed for each plot). A nonlinear mixed effect model was created to predict each of these components (**D**) and the ratio of right/left eye movement (**C**), with fixed effects of tilt direction and type of movement (tilt or translation) and a random effect of chinchilla ID number. Model output is shown in red in **C** and **D**; model parameters are detailed in Table 6. An ANOVA of the results of this nonlinear mixed effect models and a similar one after eliminating type of movement showed no detectable difference when a fixed effect of ‘type of movement’ is included (p-values for each model all >0.86), indicating that whether the eye movement was recorded during a tilt or translation did not play a significant role in creation of the model.

component of ocular counter roll (for example in Figure 39D, a tilt axis of -150° and $+150^\circ$ both elicit a right eye roll component ~ 0.8). Without a one-to-one correspondence between tilt axis and component of eye movement, more than one component of the ocular counter-roll is required to uniquely infer (i.e., back-project or back-predict) tilt axis.

Further analysis of the results shown in Figure 39CD showed the general trends listed in Table 4 below. One can quickly narrow down the group of potential tilt axes using the *binocular* polarity of the roll and pitch components in addition to the magnitude ratio. Since all data were acquired with the Z-axis initially Earth-vertical, the yaw component was not included in the table because there is large variation seen in the small yaw component and thus it was not useful for prediction of tilt axis from eye movement data. Note, this table does not present *absolute* requirements for each data group; instead, the table focuses on the polarity of the *median* ocular counter-roll for each tilt axis to get an idea of the trend of the data.

Data Group	Tilt Axis	R-Eye Roll	L-Eye Roll	R-Eye Pitch	L-Eye Pitch	Magnitude Ratio
1	$-30^\circ, -45^\circ, -60^\circ$	-	-	+	+	L>R
2	$-120^\circ, -135^\circ, -150^\circ$	+	+	+	+	R>L
3	$120^\circ, 135^\circ, 150^\circ$	+	+	-	-	L>R
4	$30^\circ, 45^\circ, 60^\circ$	-	-	-	-	R>L
5	Nose Up (-90°)	+	-	+	+	R=L
6	Nose Down (90°)	-	+	-	-	R=L
7	Right Ear Down (0°)	-	-	-	+	R=L
8	Left Ear Down (180°)	+	+	+	-	R=L

Table 4. Trends in the ocular counter-roll data grouped by tilt axis. The polarity of normalized left and right eye components of ocular counter-roll response based on the grouped tilt axes in the 2nd column. Trends found using the median responses of data shown in Figure 39CD.

Using the trends listed in Table 4, a linear mixed-effect model was made to predict the tilt axis based on three fixed effects as follows: 1&2) the *interaction* between the sign (+ or -) of the normalized pitch-component and ((arccosine of normalized roll-component)-180) for *each eye* and 3) the ratio of right/left eye ocular counter-roll magnitude, where arccosine was completed in degrees. The model also used a random effect of chinchilla ID number. Figure 40 shows the normal data that was used to train the model (purple diamonds) plotted with two of the model's inputs,

normalized X and Y of the left eye. The predicted model output (green circles) fits the normal data with adjusted $R^2=0.65$. To achieve this level of goodness of fit, the model relies on normalized *binocular* roll and pitch components and the ratio of the magnitude of ocular counter-roll position between the two eyes. Yaw added no significant information to the prediction so was not included. Each of the included fixed effects and interactions of fixed effects show significance in back-predicting the tilt direction ($p<0.01$ for all). Model parameters are listed in Table 7 in the Appendix.

2.1 Discussion

Until now, vestibular prosthesis development has focused on stimulation of the three SCCs with the goal of restoring the angular component of VOR. With the breadth of literature on normal eye movements elicited during rotations about the axes of the SCCs, and the straightforward, unipolar encoding of rotational velocity head movements, SCC stimulation was an optimal place to begin for vestibular prosthesis development. This development relied on the electrically-evoked 3D aVOR as a key metric to interpret the electrically-encoded motion and optimize vestibular prosthesis designs [29,31–33].

Two challenges have prevented extension of vestibular prosthesis designs to achieve systematic stimulation of the utricle and saccule to restore the tVOR and ocular counter-roll responses. First, the dense packing of hair cells and afferent neurons with different directional sensitivities in the utricle and saccule make it a more challenging target for electrical stimulation, which unavoidably incurs spurious activation due to current spread. Second, with the limited characterization of 3D binocular OOR in lateral-eyed animals it is more difficult to follow the path of development for SCC electrical stimulation that proved to be so successful. These two challenges have motivated this work on the characterization of the 3D OOR in the chinchilla, an attractive animal for preliminary vestibular research due to the easy surgical accesses to the inner ear.

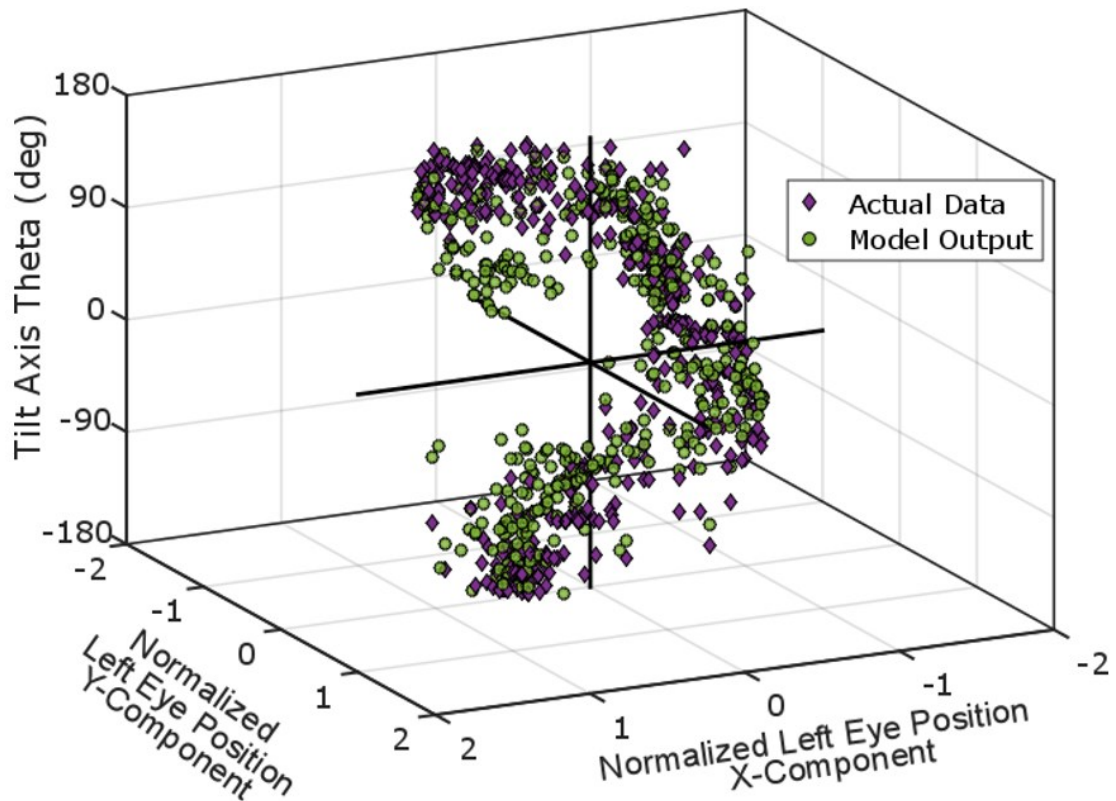


Figure 40. Model output to predict tilt axis using binocular eye movement data. Theta of the tilt axis versus the normalized X and Y components of ocular counter-roll (purple diamonds) showed a helical trend. To reverse the model to predict the tilt axis based on ocular counter-roll, a linear mixed effect model was created to predict the tilt axis based on the different components of eye movements. This fit to predict the tilt axis was achieved using fixed effects of: the interaction between the sign of the right eye pitch and arccosine of right eye roll, the interaction between the sign of the left eye pitch and arccosine of left eye roll, and the magnitude ratio of the ocular counter roll of the right/left eye with a random effect of chinchilla. The model (output shown in green circles) has an adjusted R^2 of 0.65 with significance for all fixed effects included (all p-values < 0.01). In design of this model, it became apparent that the best fit must include information from the roll and pitch components of both eyes, as well as the magnitude ratio. This model provides a basis to use electrically-evoked eye movements to predict the electrically-encoded tilt axis from prosthetic stimulation of the utricle and saccule. Model parameters are detailed in Table 7.

Angular VOR showed overall consistent direction of eye movements from previously published experiments [29,38]. The eye velocity was compensatory for head velocity for yaw, LARP, and RALP rotations, with eye position returning to the starting position within 2-3 seconds after termination of the rotation. One key difference from the previously published results showed a difference in the amplitude of eye velocity between the right and left eyes for both LARP and RALP rotations. During a LARP rotation, the right eye showed smaller responses and greater

variability in the axis of rotation. During a RALP rotation, the left eye showed smaller responses with greater variability. This difference could be partially attributed to some restriction from the scleral coils, but the data were also collected in a different manner than the previous experiments. Della Santina et al. and Migliaccio et al. both collected their data with an Earth-vertical motor, thus requiring static reorientation of the animal to align the LARP and RALP canal planes with Earth horizontal to obtain their data [29,38]. With the 6DOF motion platform, this reorientation was not required, and thus the difference in eye velocity amplitude, seen in all six chinchillas, could likely be a physiologic response.

Ocular counter-roll responses due to static tilts have been shown to maintain spatial orientation due to reorientation of the head with respect to gravity in both lateral- and frontal-eyed animals and humans [126–128,132]. While the *direction* of ocular counter-roll provides compensatory response to the head reorientation, the *magnitude* of the ocular counter-roll is smaller than a gain of one for chinchillas (these results and those previously collected by Migliaccio et al. [38], as also shown to in rabbits during static tilts by Maruta, et al. [127] and further supported by the gains at very low frequencies of sinusoidal translation by Baarsma and Collewijn [80]. Each component of the chinchilla ocular counter-roll showed cosine dependence on the axis of the tilt angle (i.e., the azimuth angle from +X) with a larger eye movement seen for each eye during tilts about axes aligned with the line of sight of the contralateral eye.

As discussed by Goldberg et.al [7], the translational VOR of humans and other primates seems to have been optimized to maintain visual acuity of targets on the fovea of the retina during linear translations, especially at high frequencies. Research by Paige and Tomko [130], Schwarz et.al [139,140], and Hess and Angelaki [94,129] support these observations, emphasizing the importance of fixating a visual target for generation of a robust tVOR response in monkeys. Compared to chinchillas, monkeys show larger horizontal eye velocities during lateral translations to maintain this fixation; this difference between monkeys and chinchillas is readily apparent in Figure 35. However, for afoveate animals, such as rabbits, rats, and chinchillas, there is minimized

importance of this response since visual fixation does not occur for afoveate animals and the lateral-eyed chinchilla relies less on the visual acuity than primates, minimizing the need for high gain tVOR responses [38,141].

Our chinchilla tVOR data (collected in the dark) corroborate trends seen in previously published data in other lateral-eyed species [77,79,80] where the tVOR responses support compensation for an apparent tilt angle based on the vector sum of acceleration and gravity instead of the translation direction. Similar to results discussed by Baarsma and Collewijn in rabbits [80], and Hess and Dieringer in rats [79], the positional changes in eye movement during translation in chinchillas were very small, $\sim 1^\circ$ to 2° peak-to-peak during 1 Hz sinusoidal accelerations (Figure 33A-D). The chinchilla's tVOR roll and pitch components of eye position were compensatory for apparent head tilt. Translations in the horizontal and coronal planes display a larger eye velocity magnitude in one eye during translations along axes approximately aligned with the contralateral eye. This observation was also seen by Hess and Dieringer in rats [79].

To compare results collected during static tilt to those during linear translations, models were created to first predict the ocular counter-roll eye position during tilts, and the tVOR eye velocity during horizontal plane translations. Simple observation of the variation in eye movement revealed a nonlinear, sinusoidal relationship between the input of tilt or translation axis and each model's predicted output of component of eye position or velocity. Thus, the nonlinear mixed effect model used a cosine base function with a random effect of chinchilla ID number. This random effect takes into account small variabilities between animal when creating the model, which is common for models with a small sample size. These models can subsequently be used to forward-predict the eye movements normally elicited during different movements in chinchillas if the axis of tilt or translation is known.

Although separate models were made for the two different motion stimuli (static tilt and horizontal plane translation), similar to Baarsma and Collewijn [80], Hess and Dieringer [79], and Dickman and Angelaki [77], we found that the tVOR velocity results were compensatory for an

apparent tilt. This prompted creation of an additional model to predict the normalized eye movements (i.e. just using direction and not magnitude of eye movements) from tilt and translation data. The results of this model did not show significant differences between tilt and translation data, thus offering support for the apparent tilt theory for analyzing chinchilla tVOR.

Constraints on distinguishing normal tilt versus translation responses arise from the input from other vestibular end organs during static tilts and the difference in dynamics of a translation versus a tilt. First, during a static tilt, the vestibular system initially senses the angular head rotation that occurs during movement to the static tilt position. Then the change in orientation of the gravitational vector during a static tilt not only affects the shear forces felt on the utricular macula, but the saccular macula as well. Therefore, a true whole body tilt is sensed and reported by input of SCCs, utricle, and saccule. Second, the dynamics of the acceleration during a translation are different than a static tilts. Due to equipment limitations it is nearly impossible to give a constant linear acceleration for a 40 second duration. However, Baarsma and Collewijn showed eye position during constant acceleration linear track that reached much higher gains than those seen during the sinusoidal translations, although with very slow response time, the eye movement was still increasing in amplitude after nearly 5 seconds after the start of movement [80].

As previously mentioned, moving toward electrical stimulation of the utricle and saccule requires a map to interpret an electrically-encoded head movement using the eye movements. One unfortunate aspect of using a sinusoidal fit for all head to eye movement mapping models above is that without extra information, there is not a 1-to-1 reversibility to then predict tilt axis from one component of eye movement. However, combining both pitch and roll information, as well as the difference between the binocular magnitudes of responses allowed us to develop a model that can provide this inverse map to predict the axis of head tilt from the change in roll and pitch eye position during an ocular counter-roll.

In conclusion, we characterized binocular 3D otolith-ocular responses of six chinchillas and created models revealing that the ocular counter-roll responses show a compensatory roll and pitch

eye movement for changes in whole-body static reorientations. The translational VOR elicits very small changes in eye position, and the relationship between eye rotational velocity and head linear acceleration exhibits low pass dynamics. Roll and pitch tVOR velocity is compensatory, in direction, to the change in gravity that would be sensed from an apparent head tilt to the direction of translation. Binocular roll and pitch information, in addition to the binocular magnitude of the OOR response, is required to create a model to predict tilt axis from eye movement. Using this model created six normal animals, an electrically-evoked ocular counter-roll could be used to infer the apparent natural tilt or translation stimulus that would normally give rise to the measured eye movement response.

Chapter 4 Electrically-Evoked Eye Movements from Utricle and Saccule Stimulation

4.1 Introduction

The process toward restoring aVOR in guinea pigs, chinchillas, monkeys, and humans using electrical stimulation created a path of development for new vestibular technologies. The development of the vestibular prosthesis relied on the depth of published literature characterizing aVOR responses from head rotations and electrical stimulation in these various species to interpret electrically-evoked eye movements and further optimize stimulation. In comparison, few publications describe electrically-evoked OORs, and those that do present conflicting results.

Suzuki et al. [49] electrically stimulated the utricular nerve in cats using short pulse trains (2-50 pulses) with 100-500 μ s per pulse duration. During these short bursts of stimulation, they observed rotation of both eyes, with upward shifts in the ipsilateral eye, downward in the contralateral eye, and small horizontal changes in eye position. Additional experiments were completed by Goto et al. [50,51] who also attempted to measure eye movements elicited from stimulation of the utricular and saccular nerve in cats. With utricular nerve stimulation, Goto et al. reported horizontal eye movements and primarily vertical eye movements from saccular nerve stimulation.

Fluur and Mellström [52–54] described attempts to stimulate the maculae in cats using 1 ms pulses of 200-800 mV at 300 pps and reported eye movements from visual inspection. They reported coordinated eye movements of compensatory direction based on the location of stimulation across the maculae. In a similar fashion to Fluur and Mellström, Curthoys [55] reported results of electrical stimulation of the utricular and saccular maculae in guinea pigs with fine electrodes, expected to result in less current spread and therefore more selective stimulation. However, Curthoys reported that electrically-evoked eye movements always tended upward or up+torsional, independent of the stimulation location on the maculae.

Ramos de Miguel et al. report on utricular stimulation in humans [56]. Three electrodes from a commercial cochlear implant were inserted temporarily in the vestibule near the utricle while attempts were made, with the patient under general anesthesia, to record far-field potentials the authors believed were electrically-evoked compound action potentials (eCAPs) from the electrode array and ocular vestibular evoked myogenic potentials (oVEMPs) for the contralateral eye. They reported detection of eCAPs and oVEMPs. However, the level of specificity that can be achieved with that approach to utricular stimulation remains to be seen, because the methods described cannot measure eye movement directions. Moreover, the results Ramos de Miguel *et al.* reported should be interpreted in light of the fact that for normal subjects, oVEMPs are typically absent under general anesthesia.

Discrepancies between the very limited number of studies that have attempted selective electrical stimulation of the utricle or saccule suggest a need for further investigation to determine the feasibility of spatially selective (and prosthetically effective) utricle and saccule stimulation. With the results of normal OOR responses in chinchillas and the corresponding model using ocular responses already established and able to predict static tilt axis reported in Chapter 3, the foundation for interpreting electrically-evoked OORs in the chinchilla has been developed. This chapter presents electrically-evoked ocular counter-roll responses using all the technology development discussed in Chapter 2 to extend the MVP to stimulate the utricle and saccule.

4.2 Methods

4.2.1 Surgery

All experiments were performed using normal adult chinchillas (*C. lanigera*). Surgical procedures were conducted in accordance with a protocol approved by the Johns Hopkins Animal Care and Use Committee, which is accredited by the Association for the Assessment and Accreditation of Laboratory Animal Care (AAALAC) International and consistent with European Community Directive 86/609/EEC. After the surgical implant of scleral eye coils, described in

detail in section 3.2.1 and following the completion of normal data collection, a second surgery to implant the electrode array was completed.

Under general anesthesia (isoflurane, 1.5%-5%), an electrode was implanted in the animal's left ear using an approach through the posterior bulla as shown in Figure 41. To place the posterior canal electrodes, a small hole was drilled into the posterior canal and the electrode shank was threaded into the canal until the contacts reached approximately to the posterior ampulla (this distance was measured with the 3D chinchilla model and marked on the electrode array pre-operatively). Two small openings were drilled into the horizontal and anterior canal ampullae. The two holes were connected to allow for easier manipulation of the electrode shanks during insertion. Since the utricle and saccule targets cannot be seen from the surgical view, we relied on the predetermined geometry of the electrode array for guidance to the utricle and saccule. Each electrode shank (saccule+LH canal, and utricle+LA canal) was carefully inserted into the drilled holes with the electrode contacts on the electrode array's anterior surface. Once the electrodes targeting the SCCs reached the ampulla, we used fascia to hold the electrode shank in place and then cemented the array into place using dental acrylic. One Pt/Ir reference wire was placed in the common crus, and a second distant reference wire was placed in the muscle (see 2.3.2.2 for details on the reference wires). The small PCB used to connect to the electrode and provide the percutaneous connection for experiments was cemented to the head cap using dental acrylic. The animal recovered for 5-7 days before proceeding with stimulation experiments.

4.2.2 Eye Movement Recording

All eye movement recording methods are identical to those described in section 3.2.2

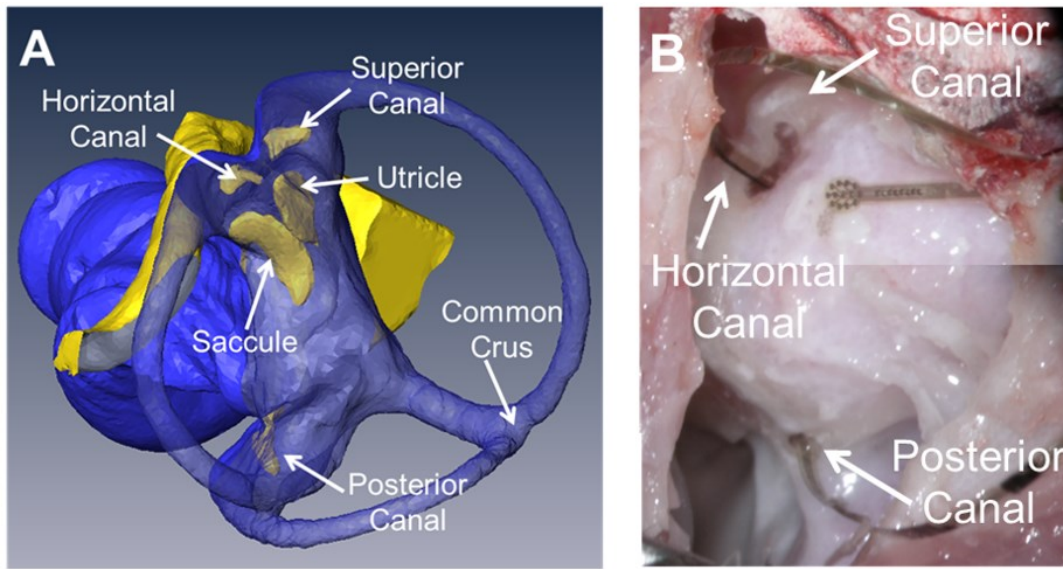


Figure 41. The surgical view during the polyimide vestibular electrode implant procedure. **A.** The surgical view with our 3D model. **B.** shows an image taken during surgery with the posterior canal electrode shank and the horizontal+saccule array shank in place. During surgery, the view of the utricle and saccule is occluded by bone covering paraflocculus, thus we rely purely on the geometry of the electrode array to reach the target end organs.

4.2.3 Electrical Stimulation Paradigm

All experiments were completed in darkness, to avoid visual suppression of the VOR, with the animal's head fixed in the center of the coil system frame with the head tilted down $\sim 50^\circ$ to align the horizontal SCCs with Earth horizontal [137]. The animals were not treated with gentamicin to ablate the hair cell stereocilia and cause vestibular loss, instead, 'virtual movements' were created using changes in stimulation rate while the animal's head was kept still. All pulses were 100 μs /phase with a 50 μs interphase gap. During the first experiment for each animal, current thresholds were determined by turning on stimulation for each electrode and slowly increasing to a maximum of 200 μA /phase. We kept 200 μA as our maximum to provide a large safety buffer during the first experiments of this kind; this limit is well within the 'safe charge injection' range for an AIROF electrode of this diameter. If any sign of facial nerve activation was seen before the 200 μA level was reached, that value was set as the maximum, and a value of 80% of maximum was used, otherwise 200 μA was used as the maximum. Electrode contacts were numbered as shown in Figure 42. Since post-mortem imaging was conducted after completion of all experiments,

saccule stimulation refers here to stimulation via electrodes intended to target the saccule (electrode contacts 1-13), *utricle stimulation* refers to stimulation via electrodes intended to target the utricle (electrode contacts 14-26), and *SCC stimulation* refers to stimulation via electrodes intended to target the three SCCs (electrode contacts 27-50).

4.2.3.1 Virtual Sinusoidal Rotation

At the beginning of each experiment, ten cycles of a virtual rotation were delivered to each of the 50 electrodes using the common crus reference to track any changes in electrically-evoked VOR over time. A simulated sinusoidal rotational velocity was converted to sinusoidal changes in pulse rate using a sigmoidal map with the following parameters: baseline rate of 100 pulses/s (pps), maximum 350 pps, minimum 0 pps, and compression factor of 3 mapped to $\pm 500^\circ/\text{s}$ angular velocity. Each virtual rotation was a 1 Hz sinusoid with peak $100^\circ/\text{s}$. The sigmoidal map is shown in the block diagram in Figure 18.

4.2.3.2 Virtual Static Tilt/Constant-Rate Pulse Trains

A step change in pulse rate was delivered via every utricle and saccule electrode using the common crus, distant, and various near bipolar reference electrodes. Each 40 sec pulse train used a step change in pulse rate from zero, to the pulse train rate (ranging from 50-300 pps). The pulse train was on for 40 seconds; stimulation stopped to indicate the end of the virtual static tilt/pulse train.

4.2.4 Data Analysis

All data analysis methods are identical to those discussed in section 3.2.4, however all eye movements were electrically-evoked from virtual movements (i.e., the animal was kept still while stimulation rate was changed to encode a virtual movement). Additionally, the digital pulse from the microcontroller indicating timing of each stimulation pulse was used to analyze the eye movements with respect to stimulation.

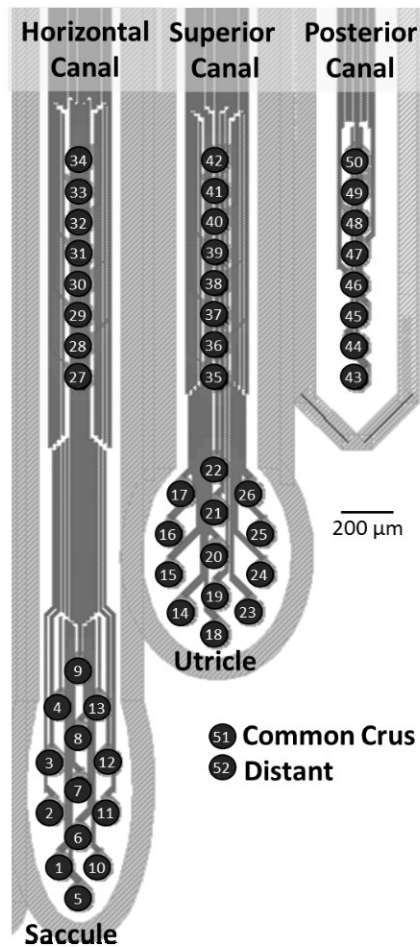


Figure 42. Polyimide electrode array contact numbering scheme. Electrodes 1-13 are intended for the sacculle, 14-26 the utricle, 27-34 the left horizontal SCC, 35-42 the left superior SCC, and 43-50 the left posterior SCC. Electrode 51 was a Pt/Ir wire placed in the common crus and 52 was a Pt/Ir wire placed in the distant muscle. Each contact is 101 μm in diameter.

4.2.5 Imaging of Electrode Placement

Electrode placement was visualized using a SuperArgus CT scanner (Sedecal, Spain) microCT scan. Scan parameters were set to acquire 1080 projections at high resolution, with 1x1 binning, 65 kV, 100 μA, 200 ms exposure, resulting in 32 μm isotropic voxel size and the capability to visualize the implanted electrodes with minimized metal artifact. Due to equipment constraints, all scans were completed post-mortem; therefore, all physiologic data were collected and analyzed before knowing the placement of the electrode arrays. MicroCT segmentation was completed using Amira (FEI Visualization Sciences Group, Bordeaux, France). Figure 43 shows the segmented CTs for the three chinchillas.

4.3 Results

There were five goals/questions for this initial implementation of utricle and saccule stimulation: 1) can we replicate results of SCC stimulation with the new system, 2) can we maintain a sustained ocular counter-roll response during constant-rate pulse train stimulation, and if so, does the response increase as pulse rate and/or pulse amplitude are increased, 3) do we observe different responses and temporal dynamics between stimulation of the SCCs versus the otolith electrodes, and 4) what direction of ocular counter-roll responses can we achieve with stimulation of the left ear, and 5) can we elicit *different* ocular counter-roll with stimulation on *different* electrodes across the maculae. The three chinchillas implanted with electrode arrays were Ch128, Ch132 and Ch133. Three types of reference electrodes will be referred to, 1) distant reference, PtIr wire in the muscle behind the ear, 2) common crus reference, PtIr wire located at the common crus, and 3) near bipolar reference, which refers to a neighboring electrode located on the same end organ as the stimulating electrode (1-13 for saccule, 14-26 for utricle).

4.3.1 Electrically-Evoked Angular VOR

To test the new stimulation circuitry, software, and electrodes, we first measured aVOR responses to replicate previous findings with SCC stimulation in chinchillas, detailed in [29]. The top row of Figure 44 illustrates the normalized axis of aVOR velocity during 1 Hz sinusoidal whole-body rotations at peak 30°/s velocity, about the axis of each canal, recorded after each animal was implanted with a head cap, head post, and scleral eye coils, but before electrode implant. Each axis shows the response during a leftward rotation. Due to the wealth of knowledge on normal aVOR responses in chinchillas [29,38], we can determine the integrity of scleral coil placement with the aVOR response from normal rotations about each SCC axis. While the majority of the axes are aligned to the appropriate aVOR response, Ch128's and Ch133's right eye LARP response shows some misalignment from the LARP axis, indicating possible restriction from scleral coil placement.

The bottom row of Figure 44 shows the normalized electrically-evoked aVOR elicited from

stimulation on the highlighted electrodes (LH=left horizontal, LA=left anterior, and LP=left posterior SCCs), all using a common crus reference. In general, the best electrodes for each chinchilla are in clusters of two or three neighboring electrodes, giving an indication of the electrode placement before the microCT scans were completed. For Ch132, the best electrodes for LH are more spread out due to a disconnect in the electrode array for 29. All of the electrodes in LA elicited well-aligned responses in Ch132. Ch133's LA canal stimulation showed likely current spread toward LH, causing misalignment of the LA response, which is common due to the proximity of the LH and LA ampullae.

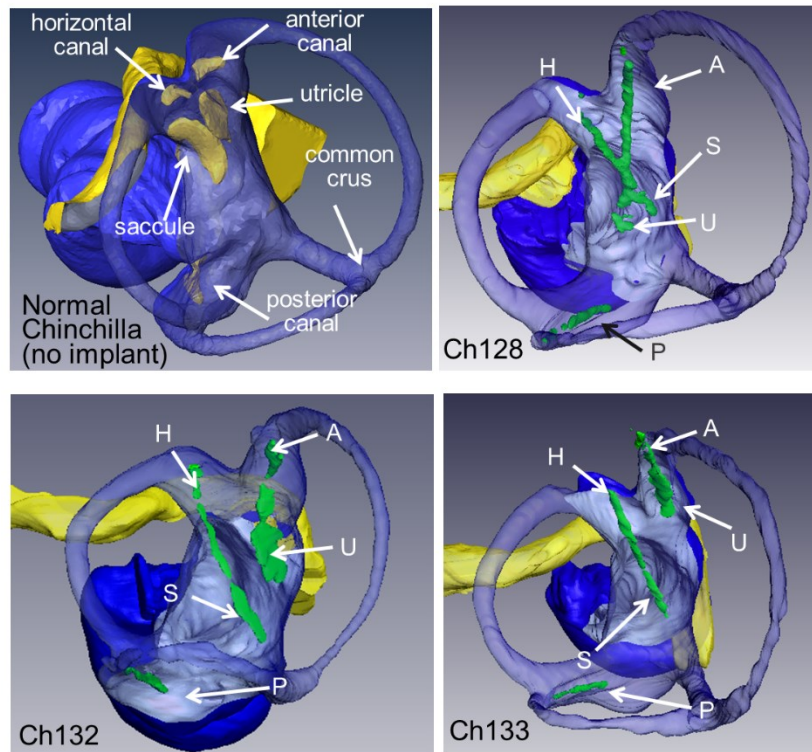


Figure 43. Post-mortem microCT scans for each of the three implanted chinchillas with the normal MRI image in the top right corner labelled for comparison. The scan at 32 μm resolution was segmented in Amira (FEI Visualization Sciences Group, Bordeaux, France). Blue=lumen, yellow=facial nerve, green=electrode array, each array is labelled based on intended target as follows: H=Horizontal SCC, A=Anterior (or superior) SCC, P=Posterior SCC, U=Utricle, and S=Sacculle. The posterior SCC array was well place in all three animals. For Ch128, the horizontal and superior target electrodes were well place but the trajectory of the utricle and saccule cause overlapping in the vestibule. Ch132 showed ideal horizontal and superior array placement with optimal location of the utricular array, but the saccule was more superior to the target end organ. Ch133 had the best saccule placement of the three animals, however the utricle array contacts are on the medial side of the array, where the target end organ is lateral. These post-mortem microCTs assist in analyzing the data collected from each animal prior to these scans.

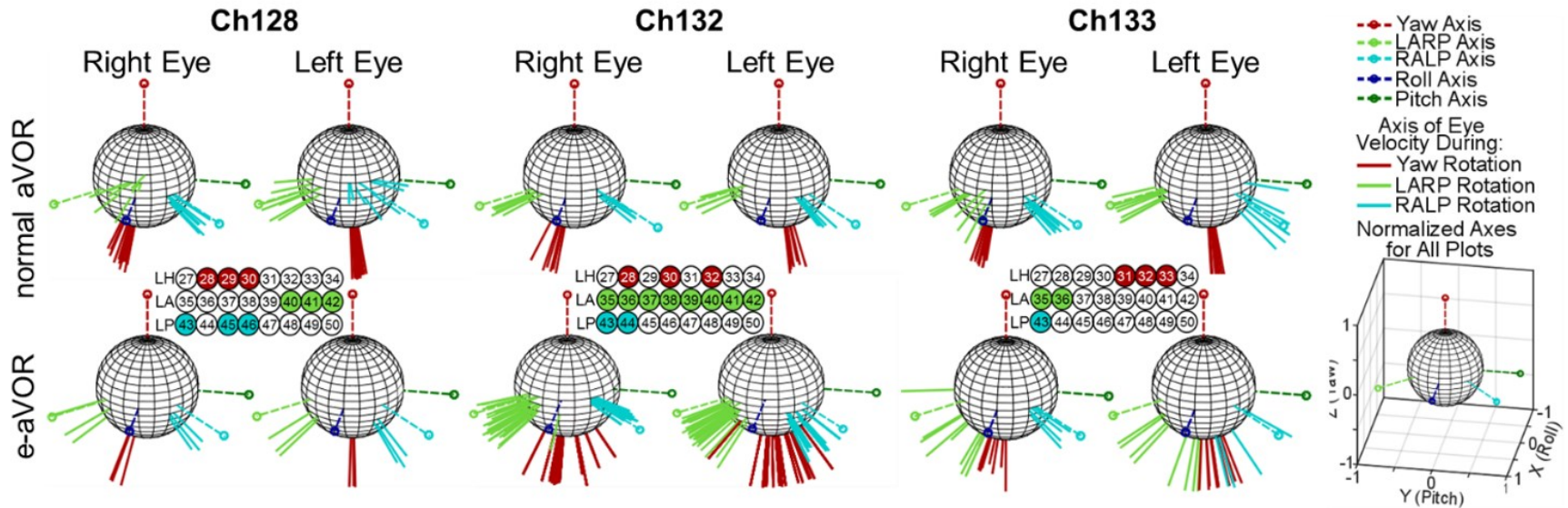


Figure 44. Electrically-evoked aVOR from three chinchillas. To test whether the new electrode array and circuitry could replicate previous results to restore the angular VOR [29,30], we compared normal eye movements collected before electrode implant (top row) to electrically-evoked eye movements (bottom row) using SCC targeted electrodes. Each spherical plot shows the normalized axes of rotation, Yaw, LARP, RALP, Pitch and Roll. The axes represent the axis of eye velocity during a left-ward head movement for the normal data. In general, the axis of eye rotation is aligned with the axis of rotation (the canal axis). However, for Ch128 and Ch133, the right eye LARP response shows misalignment, which is possibly due to slight tethering from the scleral coil. For the electrically-evoked aVOR (e-aVOR, bottom row), each axis represents the normalized axis of eye velocity during peak positive stimulation. The rows of electrodes represent the eight electrode contacts for the left horizontal (LH), left anterior (LA), and left posterior (LP) canals. Highlighted electrodes represent the contacts that elicited the best results within that canal.

4.3.2 Electrically-Evoked Ocular Counter-Roll

Figure 45 shows example electrically-evoked eye movements during a 40 sec pulse train at 300 pps presented to one utricular electrode pair (stimulating electrode 20 and reference electrode 15, see Figure 42 for electrode schematic) at different amplitudes shown by the different color lines. The shaded area in gray indicates the time when stimulation was on. As the pulse amplitude was increased, the magnitude of angular eye position also increased while maintaining the same direction of ocular counter-roll throughout the five trials of amplitude variation. Similarly, Figure 46 shows the electrically-evoked eye movement during a 40 sec pulse train using 100 μA pulses at varying pulse rates from 50-300 pps. These examples were collected using stimulating electrode 20 and reference electrode 19, both on or near the utricle (see Figure 42 for electrode numbers), with the stimulation period indicated by the gray shading on the plot. As the pulse rate increased, the change in angular position also increased for the eight trials of pulse rate variation.

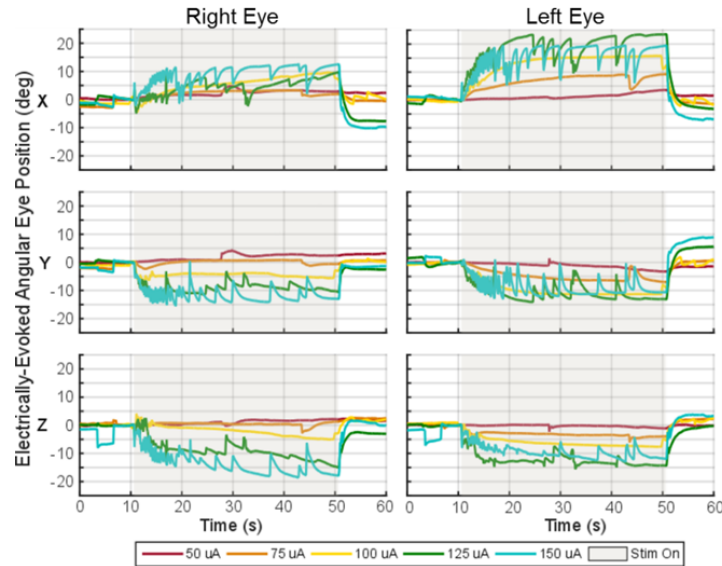


Figure 45. Electrically-evoked ocular counter-roll with stimulation of increasing pulse amplitude. Example data from Ch133 during a constant-rate pulse train using the same ‘near bipolar’ pair of electrodes in the utricle, stimulating electrode 20 and reference electrode 15 (see Figure 42 for numbering schematic). The stimulation was on for 40 seconds (gray shaded area) with a pulse rate of 300 pps. As the current amplitude was increased for each trial, a larger ocular counter-roll response was seen with consistent direction of eye response.

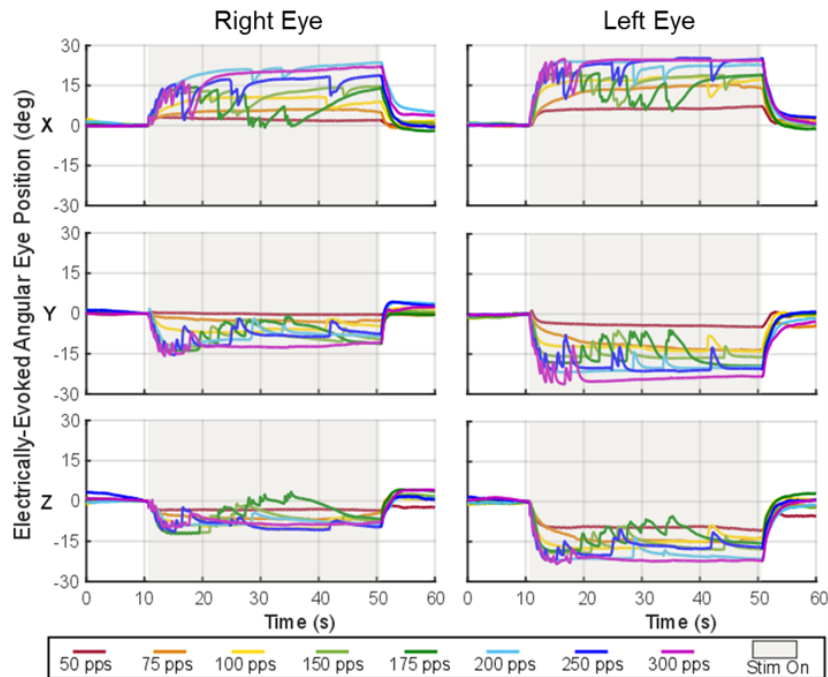


Figure 46. Electrically-evoked ocular counter-roll with stimulation of increasing pulse rate. Example data from Ch133 during a constant-rate pulse train using the same ‘near bipolar’ pair of electrodes in the utricle, stimulating electrode 20 and reference electrode 19 (see Figure 42 for numbering schematic). The stimulation was on for 40 seconds (gray shaded area). Each biphasic pulse was 100 μ s per phase with a 50 μ s interphase gap and 100 μ A amplitude. As the pulse rate was increased for each trial, a larger ocular counter-roll response was seen with consistent direction of eye response.

4.3.3 Temporal Dynamics of SCC versus Otolith Stimulation

Figure 47 illustrates a comparison between a step in pulse rate (200 pps) delivered to SCC electrodes with a common crus reference and a step in pulse rate (300 pps) delivered to utricle- or saccule-targeted electrodes with either distant, common crus, or near bipolar references. Although a 40 second pulse train delivered to the SCCs (equivalent to constant velocity rotation for 40 sec) is not a common movement, this was completed to study the difference in dynamics between the SCCs and otolith end organs when exposed to a similar electrical stimulus. Each panel displays both the right (top row) and left (bottom row) eye angular position over time. Varying responses were seen during the step change in the SCCs, as illustrated with the three representative examples in columns a-f. The first (a,b) shows prolonged nystagmus seen at the onset of the stimulation that begins to decay over time with an increase again at stimulation offset. The second column (c, d)

shows an eye response similar to an ocular counter-roll (with the addition of quick phases), with a change in angular eye position that is held throughout the stimulation, possibly indicative of current spread to the utricle or saccule. The third column (e, f) shows a fast adapting nystagmus at the onset of stimulation, typical of an SCC-mediated aVOR response to electrical stimulation targeting the SCC.

The electrically-evoked eye movements from a pulse train stimulus delivered to utricle and/or saccule electrodes varied in temporal dynamics based on the location of the reference electrode. Figure 47g and h shows a representative example of an electrically-evoked response during a constant-rate pulse train with a distant reference electrode. The change in eye position happens immediately upon stimulation onset, and the position is held for the duration of the stimulation. When using a common crus reference (representative trace shown in Figure 47i and j), the eye position generally changes right at onset, but then continues to grow a small amount to settle at the final angular eye position. Finally, when using a near bipolar reference, two common dynamics were seen (in addition to those shown in Figure 45 and Figure 46) with either a slow rise time to the final position (Figure 47k and l), or a delayed onset of change in angular eye position (Figure 47m and n).

Based on the differences between reference type for utricle and saccule stimulation, a comparison between rise times to final angular eye position was completed and is shown in Figure 48. All utricle and saccule constant-rate pulse train trials were pooled into three groups: distant reference, common crus reference, and near bipolar reference. The time to reach 63% of the final angular eye position was calculated for each component of the angular eye position (yaw, pitch, roll) for each eye. If one component of the eye movement changed less than 1° throughout the trial, it was excluded from this calculation. The spread of rise time for the near bipolar configuration is noticeably larger than that for distant and common crus reference. A Kruskal-Wallis test showed significance within each component of each eye. Post-hoc Wilcoxon rank sum tests determined a

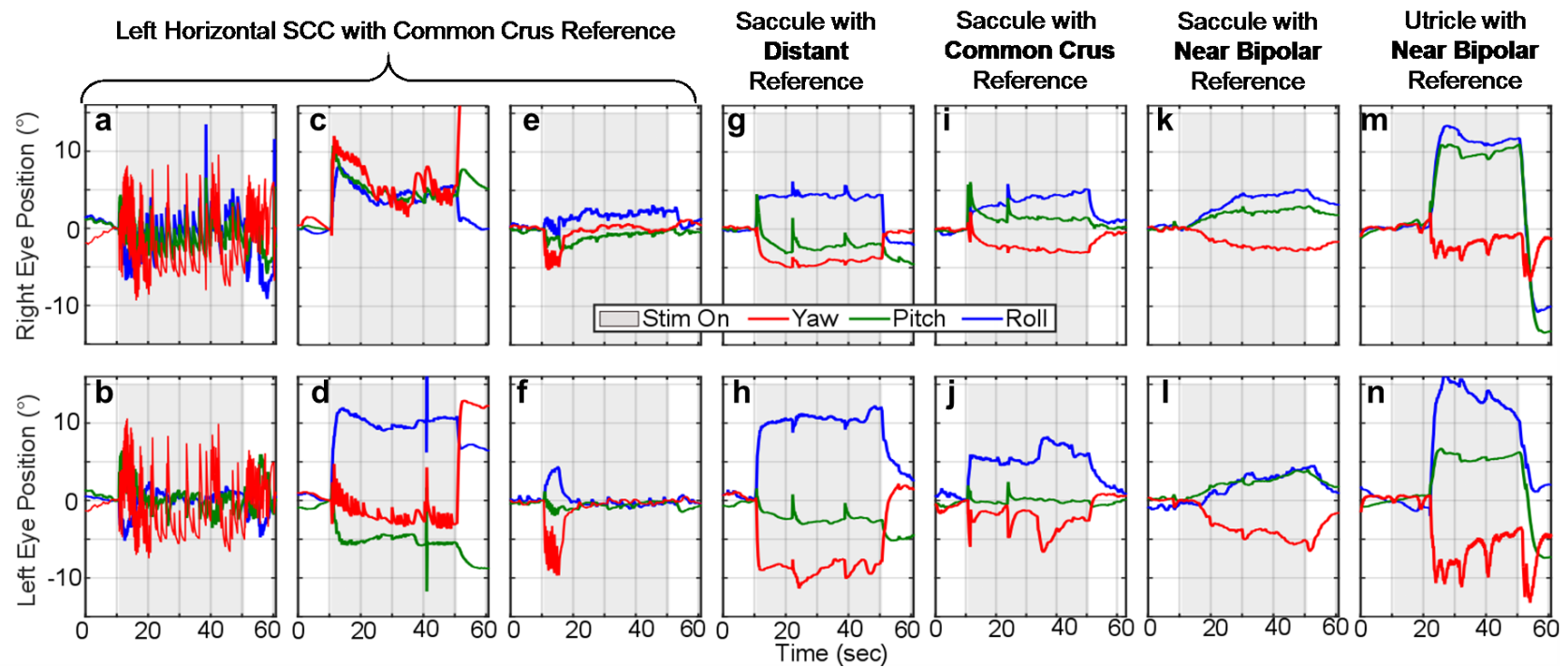


Figure 47. Electrically-evoked ocular counter-roll using different reference electrodes. Example ocular counter-roll responses during constant-rate pulse train stimulation applied to difference combinations of electrodes. Columns ABC show three different types of responses seen when delivering a step change in pulse rate of 200 pps to a SCC electrode with common crus reference. Although each example is recorded from a different chinchilla, all examples are representative of responses seen in each animals. The first example (column A, Ch133) shows immediate onset of quick phases that begin so adapt out throughout the 40 seconds of stimulation, with an increase of frequency after stimulation stops. The second example (column B, Ch132) appears to follow the trend of an ocular counter-roll, suggesting likely current spread to the otolith end organs. Third (column C, Ch128), shows a brief change in eye movement at the beginning of stimulation that quickly adapts out. To compare the SCC response to otolith, the final four columns show representative examples of a pulse train (300 pps) delivered to the utricle and saccule stimulation with distant (column D, Ch128), common crus (column E, Ch128), and near bipolar (columns F, , Ch128 and G, Ch132) references. Stimulation using distant reference elicited immediate change in angular eye position, similar to that seen during normal whole-body static tilt. The saccule with common crus example follows a similar trend with immediate change in eye position but a slower incline to the final angular eye position. Using a near bipolar reference elicited two different types of responses: 1) a slow gradual increase in angular eye position, following the low-pass filter behavior of the otolith end organs, and 2) a delayed sudden change in angular eye position after stimulation onset.

significant difference ($p < 4e-4$) between the rise time for near bipolar paradigms and that for the corresponding distant and common crus references for all components of eye movement in both eyes.

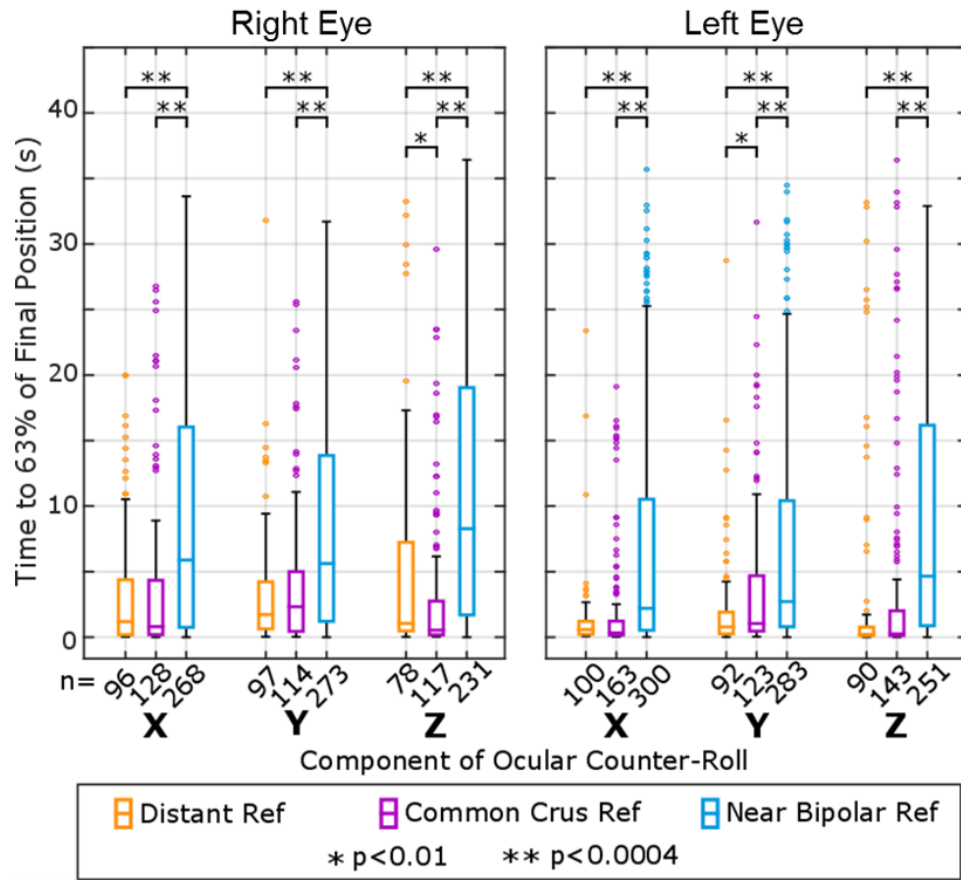


Figure 48. Analysis of electrically-evoked ocular counter roll rise time grouped by reference type. Analysis of rise time to 63% of final ocular counter-roll position for each component of each eye. Components that showed $< 1^\circ$ change in angular position were not used for this analysis which is why there is a difference in number of samples (n), listed along the x-axis. An initial Kruskal-Wallis test showed significance between the reference groups for all groups (Right X, Right Y, Right Z, Left X, Left Y, Left Z) with all p-values $< 1e-9$. Subsequent pairwise Wilcoxon rank sum tests showed significance between Near Bipolar Reference compared to Distant and Common Crus with all p-values $< 4e-4$.

4.3.4 Spatial Selectivity of Ocular Response from Otolith Stimulation

Figure 49 illustrates the non-normalized electrically-evoked eye movements from all constant-rate pulse trains delivered via a utricular electrode (first two columns) or saccular electrode (last two columns) for each chinchilla. Each line indicates the axis of the final angular position during

each pulse train and is color coded based on the stimulating electrode number, shown in the legend in the bottom right corner. The last row shows the normal ocular counter-roll axes recorded from six chinchillas during 20° whole-body static tilts about the indicated axes, shown in section 3.3.2. The yaw, pitch, and roll axes were plotted with a magnitude of 10°. Similarities between the direction of angular eye rotation from the normal and electrically-evoked data help determine the encoded tilt angle from the electrically-evoked eye movements.

As shown in 3.3.2, the normal ocular counter-roll responses from the whole-body static tilts that were tested have an asymmetry in magnitude between the right and left eyes when tilting about an axis oriented along one of the eyes. To briefly summarize, a tilt about an axis oriented through the right eye (-30°, -45°, -60°, 120°, 135°, 150°) will give a larger left eye magnitude than right eye, and thus a ratio of right eye magnitude/left eye magnitude of < 1. A tilt about an axis oriented through the left eye (30°, 45°, 60°, -120°, -135°, -150°) elicits a larger right eye magnitude than left, and thus a ratio >1. Tilts about the cardinal axes (0°, 90°, 180°, -90°) give a ratio ≈1. The magnitude of left eye response is generally larger than the right eye, indicating a tilt about an axis through the right eye (-30° to -60° or 120° to 150°). Further comparison to the direction of normal eye movements shows that the electrically-evoked responses for all chinchillas seem to be mostly aligned with normal eye movements from tilts about Earth-horizontal axes of 120° to 150° from +X. The data for Ch128 follow similar trends for utricle and saccule and correspond to what is expected based on the electrode placement shown in Figure 43. However, the saccule data for Ch132 and Ch133 show differences compared to that from the utricle, with a greater tendency toward the axes of ocular counter-roll that normally encode whole-body tilts about axes that are Earth-horizontal and -150° to -120° from the +X axis.

We investigated which electrodes elicited which eye movements, specifically grouping the eye movements by the magnitude ratio of right/left eye position. Using the three groups of magnitude ratios mentioned in the previous paragraph, each electrode that elicited an eye movement can be categorized into one of the groups. Figure 50 shows an image of the utricle and saccule array for

each group for each chinchilla (group A: ratio<0.8 red, group B: $0.8 \leq \text{ratio} \leq 1.2$ yellow, and group C: ratio>1.2 blue). Trials where the magnitudes of eye movement for both eyes were $< 2^\circ$ were eliminated. Each colored oval represents the stimulating electrode (from a near bipolar pair) that was used to elicit an eye movement in the respective group. This analysis did not show any pattern for Ch128 and Ch132 (illustrated at the top of Figure 50); however, for Ch133, the electrode that gave a (left eye positional magnitude / right eye positional magnitude) ratio Leye/Reye < 0.8 (i.e., left eye movement exceeded right eye movement by at least 25%) cluster toward the bottom part of the array. Additionally, even though not many examples for a Leye/Reye ratio > 1.2 in the utricle exist, the ones that do occur cluster toward top part of the array, suggesting semi-selective stimulation in Ch133.

4.3.5 Tilt Axis Model Output

The model created in section 3.3.5 to predict the Earth-horizontal axis of a whole-body tilt from electrically-evoked eye movements relies on binocular recordings and uses the ratio of magnitudes of the final ocular counter-roll position, the arccosine of the binocular normalized X-component, and the sign of the binocular normalized Y-component. Figure 51 shows the model output (tilt axis) grouped by otolith end organ (utricle= circles, saccule=triangles) and by the type of reference electrode. The gray diamonds represent each animal's normal eye movements, measured before electrode implant. For Ch132 and Ch133, *utricle* stimulation using distant and common crus reference electrodes encoded tilts primarily about horizontal plane axes that are 90° to 150° from +X (shown in bottom right of Figure 49), while the *saccule* stimulation using distant and common crus reference electrodes encoded tilts about the -150° to -90° axes. For Ch128, a more equal distribution of utricle versus saccule stimulation patterns is seen. Finally, when using a common crus reference electrode (blue circles/teal triangles in Figure 51) a larger coverage of the entire range of tilt axes is achieved, suggesting the need for near bipolar electrode pairs on each maculae to best encode static tilts.

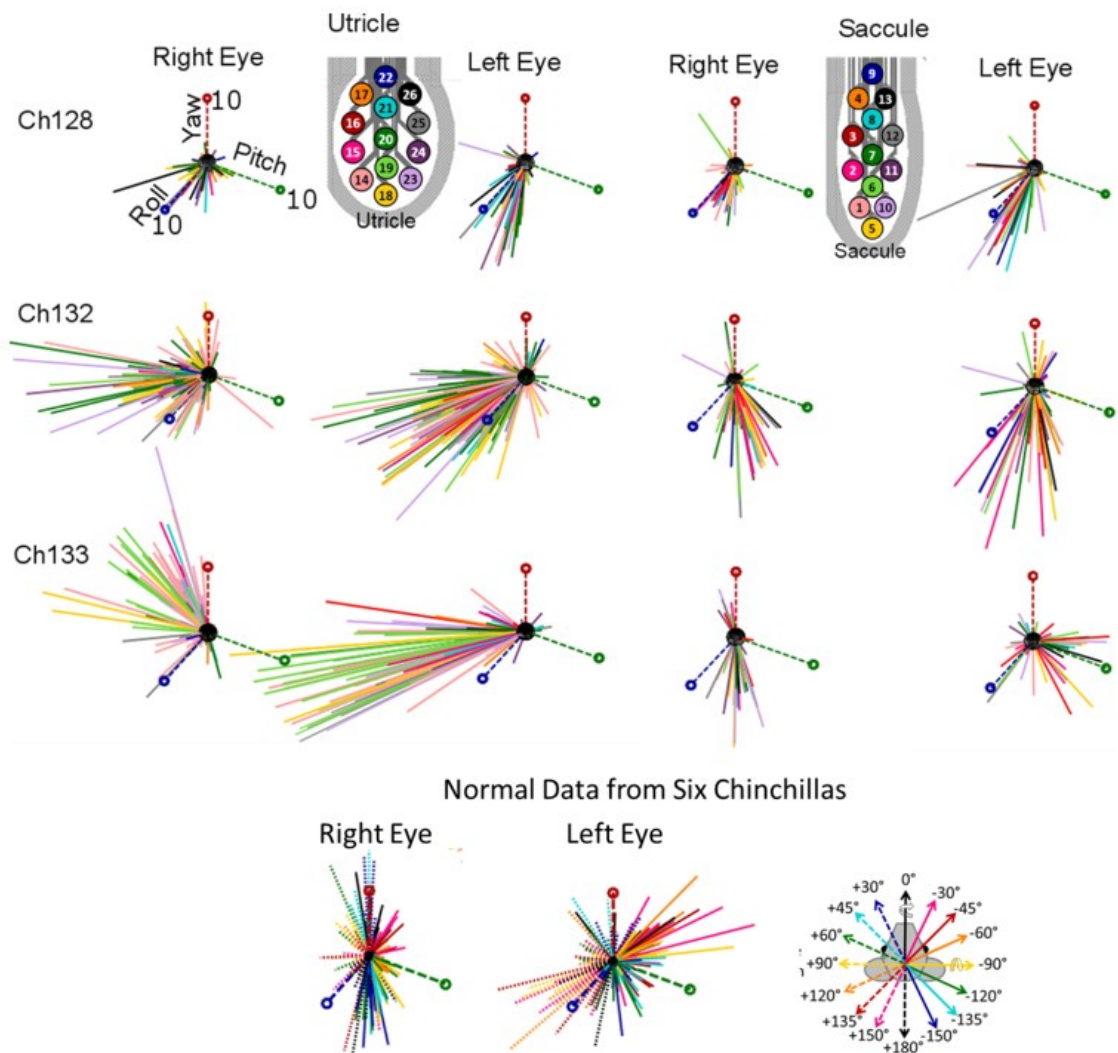


Figure 49. All results from utricle and saccule pulse train stimulation for the three chinchillas. Each line represents the axis of the final angular eye position in degrees and is colored based on the stimulating electrode used, as indicated in the color-coded utricle and saccule electrodes in the bottom right. Each plot contains the primary axes, Roll (+X), Pitch (+Y), and Yaw (+Z), which are all magnitude of 10° , as shown in the top left image. The last row shows final ocular counter-roll position recorded from six normal chinchillas during 20° from horizontal whole-body tilts about each of the axes in the legend, which follows the right-hand rule to indicate direction of tilt. By looking at all the non-normalized responses, certain patterns of encoded head tilts with the stimulation data begin to emerge. Using the utricular array, the responses trend toward the (+X,-Y) quadrant with a larger left eye magnitude compared to the right. When comparing to the normal data (collected from the Earth-horizontal axes shown in the bottom right), the utricular responses primarily follow the $+120^\circ$, $+135^\circ$, and $+150^\circ$ axes. Shifting to the saccular data, for Ch128, responses due to saccular stimulation follow similar direction as the utricle. However, for Ch132 and Ch133, a difference is seen between utricle and saccule responses. The left and right magnitudes are more symmetric and match the -120° , -135° , -150° , and $+180^\circ$ normal tilt axes (solid green, light blue, dark blue, and dashed black).

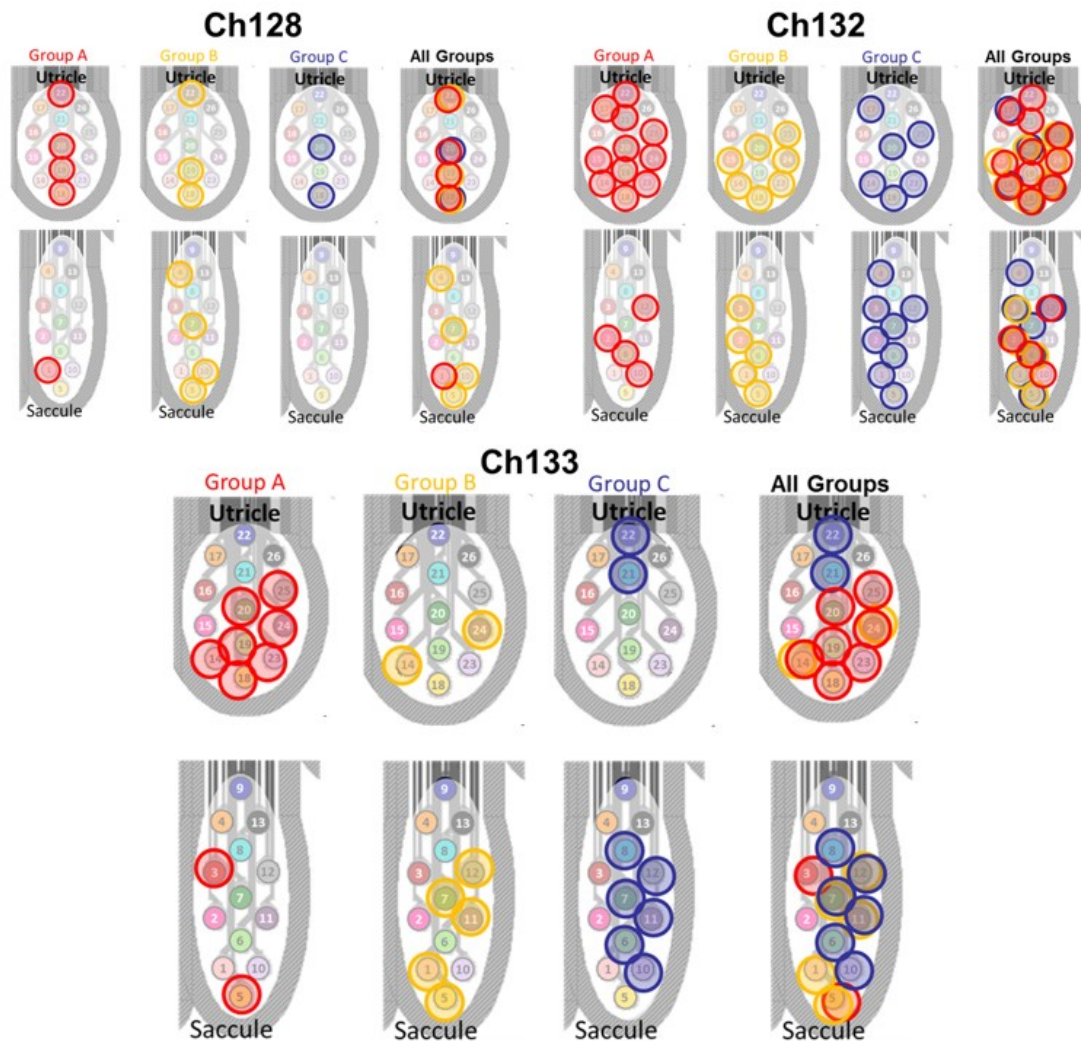


Figure 50. Spatial selectivity of utricle and saccule stimulation. To determine spatial selectivity, the direction of eye movements elicited from stimulation can be grouped based on the magnitude ratio between the right and left eyes. From the data collected from normal chinchillas, shown in section 3.3.2, the ratio of right/left eye magnitude gives an indication of the tilt axis in the following groups: **A)** left eye magnitude > right eye magnitude (ratio < 0.8) **B)** left and right eye magnitudes approximately equal ($0.8 \leq \text{ratio} \leq 1.2$), and **C)** right eye magnitude > left eye magnitude (ratio > 1.2). Each stimulation electrode used to elicit eye movements are circled and grouped based on the magnitude ratio of eye position between the right and left eye. Data shown are from all chinchillas during 300 pps pulse train of 40 sec duration, focusing on stimulation that elicited a change in angular eye position $> 2^\circ$ for both eyes. Focusing on Ch133 only, for the utricular electrodes, the majority of eye movements showed a ratio < 0.8 and were elicited more with the lower half of electrodes, circled in red. While only a few examples for Ch133 where the ratio ≈ 1 or ratio > 1.2, the examples for ratio > 1.2, cluster toward the top right. Additionally, for the saccule of Ch133, clusters of red and blue sit on opposite sides of the array. This indicates that some level of selectivity may be achievable with proper placement. However, a similar pattern was not seen with Ch128 and Ch132, as illustrated at the top of the figure.

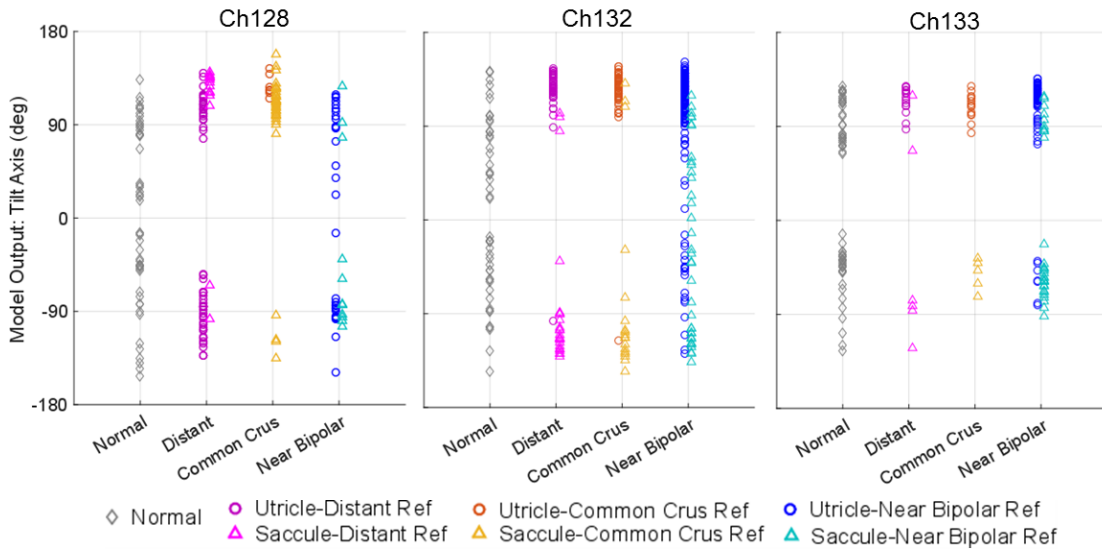


Figure 51. Model output to infer electrically-encoded tilt axis from electrically-evoked eye movements. Estimated ‘encoded tilt axis’ during stimulation on utricle (circles) and saccule (triangles) intended electrode contacts grouped by type of reference electrode. The normal eye movement output (gray diamonds) for each animal were collected before electrode implant. The model output was calculated based on the model discussed in section 3.3.5 and detailed in Table 7. The results suggest that for Ch132 and Ch133, utricle stimulation with distant or common crus reference electrodes encodes primarily tilts about axes from $+90^\circ$ to $+150^\circ$, where saccule stimulation with distant or common crus reference encodes primarily -90° to -150° axes. For Ch128, there is less distinction between these sets of model output between utricle and saccule. Using a near bipolar reference electrode, the range of encoded tilt angles better represents the normal range.

4.4 Discussion

The well-defined design, implementation, and experimental procedures that led to successful development of an MVP for stimulation of SCCs to restore aVOR [29,32] blazed a path for stimulation of the utricle and saccule to restore the sensation of GIA; however, the complex anatomy and physiology of the utricle and saccule present hurdles to achieving this goal. Due to the non-uniform polarity of hair cell orientation in the utricle and saccule, the approach for stimulation is less straightforward compared to that used for the SCCs. With the work presented here, we began to approach this challenge with a new prosthesis and electrode design for initial proof of concept utricle and saccule stimulation results and forge a path for continued iterative design and optimization toward restoration of GIA sensation.

The polyimide electrode arrays provided multiple contacts on each of the five end organs of the inner ear. The electrode material, polyimide, is a planar, very flexible carrier substrate that

allows manipulation into the canal fenestrations to access the utricle and saccule. However, the extreme flexibility and compliance of the polyimide and the planar design of electrode array made handling during surgery very challenging. Continued development of the arrays will focus on adding a silicone stiffener at key points along the electrode array to allow for easier manipulation of the electrode during the implantation procedure. The overall layout of the electrode contacts on the array provided a guide to implantation despite the inability to view the utricle and saccule during surgery, as documented in Figure 41B. By using the dimensions from an anatomical model of the chinchilla inner ear, we were able to trust the geometry of the electrode array to reach the target end organs. The post-mortem microCT scans of each chinchilla (Figure 43) indicate overall good placement of the SCC targeted electrode with variable placement of the utricle and saccule arrays. Due to the flexibility of the polyimide electrode shanks, it was more difficult to control the trajectory of the utricle and saccule electrodes, resulting in variability in placement. Based on these results, as this work moves into different species, a similar approach will be used for electrode array design based on anatomical 3D models but with modifications to the electrode array materials, see 2.3.3 for discussion of future improvements to electrode design.

In our exploration of electrically-evoked eye movements from stimulation of the utricle and saccule, we found that a constant-rate pulse train elicits a change in the angular eye position that was sustained throughout the duration of the constant-rate pulse train. The responses using the distant and common crus reference appear more like a normal ocular counter-roll response during a whole-body static tilt, as seen in Figure 31. During a normal ocular counter-roll, both the SCCs and otolith end organs play a role. The SCCs respond to the rotation at the beginning of a tilt and the otolith end organ respond from the prolonged change in GIA throughout the tilt. Based on the high-pass filter dynamics of the SCCs and the low-pass filter dynamics of the otolith end organs (when comparing eye position to head acceleration), it is possible that utricle and saccule stimulation using the *distant* and *common crus* references could also be activating the SCCs, giving the more immediate change in angular eye position (Figure 47). The delayed reaction and slower

rise time of eye movement using the *near bipolar* reference is comparable to that reported by Baarsma and Collewijn in normal rabbits during linear track accelerations [80]. The statistically significant slower rise time seen when stimulating in the utricle or saccule using a *near bipolar* reference suggests a more selective stimulation of the otolith end organs without activating SCCs. Moving toward a natural restoration of ocular counter-roll will require simultaneous but selective stimulation of the SCCs and selective otolith stimulation.

Outcomes of otolith stimulation, we found that as pulse amplitude and pulse rate were increased, the change in angular position grew while maintaining the same ocular counter-roll direction (Figure 45 and Figure 46), showing that the electrode combination gave repeatable eye movements over a short period of time (i.e. when delivered one after the other). However, the ocular counter-roll response relies on the starting location of the eye, and this effect can cause variation in the results when using the same stimulating and reference electrode pair. In some cases, over multiple days of experiments, one pair of electrodes would occasionally elicit an eye movement in a different direction than the “usual” encoded direction for that pair of electrodes, which caused the lack of one-to-one correspondence between eye movement and stimulation electrode in Ch128 and Ch132. Due to the overlap of the utricle and saccule electrodes in Ch128, it is not surprising that differences were not seen between utricle and saccule electrode stimulation. The results from investigating whether different electrodes systematically elicit different eye movements indicate a pattern within the utricular array for only Ch133 (Figure 50). With increased spatial selectivity of electrical stimulation, excitation at different locations across the maculae can better encode static tilts about a larger range of axes.

The data presented were all collected in otherwise normal animals, without use of gentamicin treatment to ablate hair cell function and induce vestibular loss. Therefore, stimulation could only be excitatory (increased pulse rate), since some spontaneous baseline neuronal firing was likely present in the implanted ear. Additionally, the contralateral ear was fully functioning and provided an opposing signal to the ‘foreign input’ of the prosthesis. Both of these facts play a role in our

findings. Most of the encoded tilt axes (azimuth from +X of 120° to 150° and -150° to -120°) all encode a tilt with the left ear down. By analogy to the way a unilaterally-implanted, SCC-stimulating MVP is run at a relatively high baseline pulse rate to facilitate encoding inhibitory head rotations after the subject's central nervous system has adapted to the artificial baseline, encoding static tilts in the opposite direction of those represented in Figure 49 using electrodes implanted only in the left labyrinth could be achieved but adapting the implanted animal to to a baseline stimulation rate from which pulse rates can be down-modulated. However, with the otolith end organs providing sensation of static changes in gravity, it is unknown how long it would take to adapt to a baseline rate, and thus a chronic stimulation set up is required. After adaptation, the change in pulse rate for pulse trains could better encode excitatory and inhibitory tilts and a greater range of encoded tilt axes could be achieved.

Future iterations of this work should try to define how many electrode contacts are actually needed based on the level of selectivity each can achieve. To answer this, we examined differences between utricle and saccule stimulation and differences based on which reference electrode was used. Both Ch132 and Ch133 elicited a different direction of the axis of angular eye position between utricle and saccule results, seen in Figure 49 and the model output of Figure 51. The larger range of encoded tilts seen when using a near bipolar reference electrode (Figure 51) suggests that multiple electrodes per end organ (to allow for near bipolar combinations across the maculae) are desirable, however, the different areas of selectivity in Ch133 (Figure 50) indicate that maybe only two pairs are required to replicate the results seen thus far. Additionally, the results could likely be replicated with two pairs per end organ, (one pair for encoded the 'red' eye movements, and one for the 'blue' as indicated in Figure 50) and after adapting to baseline and gaining the ability to excite and inhibit based on pulse rate, that number could possibly be further reduced (providing surgical placement is optimized). That being said, more electrodes may be desirable as the stimulation paradigm is optimized to more selectively activate parts of the otolith end organs and ensure accuracy given inconsistencies in surgical implantation. The prosthesis circuitry can

perform multipolar stimulation paradigms, [102] which could achieve a more controlled spread of current [115] and achieve a greater level of selectivity.

This work has focused on *eye movements* elicited by electrical stimulation targeting the utricle and saccule. However, the utricle and saccule also each play important roles in maintaining posture, balance, and stable gait. Although thorough gait analysis and postural testing in small animals is difficult, effects of otolith end organ stimulation can analyze changes in the head tilt that is often induced in animals with vestibular loss. This observatory metric offers a starting point for postural influences of otolith stimulation.

In conclusion, the concepts behind stimulation of the SCCs for restoration of the aVOR have been adapted to approach the new challenge of stimulating the utricle and saccule to restore the sensation of gravito-inertial acceleration. With the new prosthesis circuitry and electrode array, we replicated results using SCC stimulation and showed ocular counter-roll responses due to electrical stimulation of the utricle and saccule. The temporal dynamics of that response varied based on the reference electrode used, suggesting that a near bipolar reference electrode provides a more selective activation of the utricle and saccule, minimizing current spread to the SCCs. Additionally, the model gives a method to evaluate the encoded tilt axis based on the measured electrically-evoked eye movements. The model shows general differences between utricle and saccule stimulation, with the near bipolar configurations offering the possibility to begin to encode tilts about all possible axes in the Earth-horizontal plane. With these results as a foundation, continued optimization of stimulation paradigms for prosthetic utricle and saccule stimulation has the potential to restore sensation of GIA.

Chapter 5 Conclusions

5.1 Implications and Limitations

The research presented and discussed in this dissertation is one of the first to collect 3D binocular electrically-evoked eye movements elicited from animals with chronically implanted utricle and saccule electrode arrays. The technology developed in this dissertation provided a means to record small eye movements, deliver translational motion stimuli, and stimulate using new electrodes and new circuitry. These developments were key toward achieving the scientific goals of this work, and were instrumental in creating the system that will continue to be used for study of utricle and saccule stimulation.

Although the technology was successful, limitations were present due to equipment and system design. The 6DOF motion platform used to collect sinusoidal rotation, translation, and static tilt data was designed by the manufacturer with the intent to support a ~1000kg load and thus has limiting constraints on velocity and acceleration. These limitations made the already small eye movements elicited during translations even smaller due to the inability to translate at accelerations above 3 m/s^2 . We compensated for this by designing the low-noise scleral coil system, however, with a faster motion platform, eye movements would be more robust and a larger range of motion stimuli could be explored.

New electrode arrays offered a significant increase in the number of electrode contacts that could be used for utricle and saccule stimulation. With this increase, we were able to explore the level of specificity that can be achieved with stimulation of the maculae and discern the number of electrodes actually required for future designs. The extreme flexibility of the electrode arrays made surgical implantation difficult, and the final resting place of the electrode array was variable across animals. Future designs will build on these findings to create an electrode that can assist in achieving more repeatable surgical placement, and thus more robust results across animals.

Prosthesis circuitry developed in this dissertation used a microcontroller, low-power motion sensor, custom ASIC, and crosspoint switch. The microcontroller and motion sensor were chosen for their low-power consumption, which is important for future chronic stimulation studies. The custom ASIC was designed to have 16 independent current source and sink pairs so that complex stimulation patterns could be used to more selectively stimulate the maculae. The system architecture for the prosthesis is not limited to applications in vestibular research, but can serve as a general purpose stimulator. A side project completed during the duration of this thesis customized the microcontroller and ASIC circuitry to be used in a collaborating lab investigating cochlear stimulation representation in the cortex. The circuitry was successfully customized for cochlear stimulation application, see Appendix 6.1 for details.

Although the ASIC offers 16 independent stimulation channels, the crosspoint switch chosen to route these 16 channels to any of the 52 electrodes exhibited crosstalk when multiple neighboring channels were connected through the crosspoint array. For the purposes of the experiments presented in this dissertation, we were only actively using one electrode pair at a time, so we could eliminate this issue by only connecting two of the ASIC outputs to the two active channels. Future studies that aim to simultaneously stimulate on more than one end organ, will require a redesign of this crosspoint switch module.

The 3D normal binocular data characterized in this dissertation were used to create models to predict eye movements elicited from translations along axes in the horizontal plane and static tilts about axes in the horizontal plane. Similar models can be created for axes in the coronal and sagittal planes for future studies; these models are expected to show similar cosine dependence between eye movement and theta and phi of the translation axis. The translational VOR findings reported here corroborated other published work, with small amplitude eye movements showing compensatory behavior for the apparent tilt of the translation. The roll and pitch components of the ocular counter-roll responses from static tilts were compensatory for changes in gravity, while yaw component was not significant for encoding the change in gravity during tilts about Earth-

horizontal axes. A model comparing normal chinchillas' eye movement responses to tilt and translation showed no detectable difference between the *direction* of ocular response between eye movements elicited from each static whole-body tilt axis versus eye movements from a sinusoidal translation along the apparent tilt axis, however different magnitudes of eye movement were seen between the tilt versus translation data.

The purpose of characterizing the normal data went beyond gaining a scientific understanding of chinchilla eye movements. With the end goal of prosthetically stimulating the utricle and saccule to encode gravito-inertial acceleration, a model was created to predict the static tilt axis based on 3D binocular eye movements (created using a limited range of Earth-horizontal axes). This model proved useful for analyzing the encoded head tilts based on electrically-evoked eye movements but is currently limited to predict axis of electrically-encoded static tilt from normalized binocular ocular counter-roll. Continued modeling efforts of the normal data could produce more complex models with the potential to define a clear relationship between all eye movements elicited due to changes in gravito-inertial acceleration.

As one of the first ever experiments using electrical stimulation of the maculae using chronically implanted electrode arrays, these findings prove that first, we can recreate previous results with stimulation of the SCCs to restore sensation of rotational head movements. Long pulse trains of utricle and saccule stimulation elicit electrically-evoked eye movements indicative of ocular counter-roll during static tilts. These eye movements display temporal dynamics observed with whole body reorientation during static tilts in addition to those reported from long duration translations. Although we did not see well defined margins of spatial selectivity with the current electrode design, one chinchilla exhibited clusters of electrode contacts that tend to show preference to the direction of electrically-evoked eye movements.

While these results are promising toward restoration of the sensation of gravito-inertial acceleration, they are limited to state conclusive findings due to a small sample (3 animals) and variability in the placement of the utricle and saccule arrays. The findings show implications of

success toward extending the prosthesis and form the next round of key questions to be answered to move closer toward restoring sensation of gravito-inertial acceleration with stimulation of the utricle and saccule.

5.2 Future Directions

The encouraging results toward restoring sensation of gravito-inertial acceleration presented in this dissertation open many avenues for continued scientific research to continue to better optimize and understand the capabilities of macular stimulation. Continued experimentation in chinchillas can answer many important, still unknown questions and support the findings presented in this dissertation. Following the same experimental trajectory, without gentamicin treatment, experiments exploring SCC+otolith stimulation can better emulate a natural static tilt (with the initial angular rotation followed by the static reorientation). Additionally, superposition experiments using multiple pairs of electrodes, or multipolar configuration of stimulation, may help focus current to the desired activation area and provide a greater level of spatial selectivity and therefore encode a larger range of static tilt axes.

With bilateral gentamicin treatment, conflicting influences from the intact contralateral ear can be eliminated and several additional opportunities can be pursued including adaptation to baseline stimulation, chronic stimulation, and motion+stimulation. Since the otolith end organs are designed to sense static changes in gravity due to head reorientations, adaptation to a baseline rate could prove difficult and require technology development to make chronic stimulation possible. With adaptation to baseline, pulse rate modulation can encode both inhibitory and excitatory signals (versus without baseline adaptation, such as in the experiments in this dissertation, only excitatory stimulation is possible). It is likely that the encoded head tilts will better span all tilt axes in the horizontal plane, and not primarily those that bring left ear down with both inhibitory and excitatory stimulation. Motion+stimulation has previously shown more robust aVOR movements in monkeys

[31] due to sensory integration of proprioceptive cues of movement and thus is an interesting avenue to study in chinchillas.

Chronic stimulation also allows for exploration of otolith stimulation's influence on posture. With the utricle and saccule sensation of changes in gravity, it provides an important input to balance. Chinchillas exhibit a strong static head tilt after ototoxic injury due to gentamicin treatment (an indication of both SCC and otolith hypofunction). With chronic stimulation, the change in this static head tilt could be studied through time to diagnose time constants in the plasticity of these circuits to interpret electrical stimulation.

Following further optimization in chinchillas, this technology can be implemented to replicate these results in a non-human primate. With slight modifications to the electrode array, the prosthesis circuitry and software could easily progress for experiments in monkeys. Since monkeys, like humans, are frontal-eyed and have retinal foveae, the tVOR likely plays a more important role in monkeys than it does in chinchillas. Therefore, additional experimental paradigms using fixation on a point during motion+stimulation can be completed.

In summary, the technology developed as part of this dissertation offers a platform for many continued experiments to elucidate the capabilities of otolith stimulation. The chinchilla data presented is the first of its kind to explore 3D electrically-evoked eye movements and serves as the preliminary stepping stone for many more continued experiments to thoroughly implement otolith stimulation in chinchillas, monkeys, and eventually humans.

5.3 Conclusions

Research on stimulation of the three semicircular canals to restore the angular VOR progressed from chinchilla to non-human primates and is now finding success in humans. The work presented in this dissertation aimed to extend the application of the successful vestibular prosthesis to also stimulate the utricle and saccule to encode gravito-inertial acceleration and drive otolith-ocular reflexes. A new system was developed to achieve this goal, including a low-noise scleral coil

system for measuring eye movements, a six degree-of-freedom motion platform to provide rotational and translational motion stimuli, a new electrode array containing 50 electrode contacts for stimulation of the SCCs and otolith end organs, and new hardware, software, and firmware for the prosthesis. This new system achieves the goals of this dissertation and offers a tool for continued vestibular prosthesis experimentation in addition to other applications of neural stimulation beyond the vestibular system.

Extensive characterization of normal chinchilla 3D binocular eye movements during translations and static tilts enabled the creation of a model to predict head movements based on recorded binocular eye movements. This model proved to be valuable for interpreting encoded tilts from electrically-evoked eye movements from utricle and saccule stimulation. The temporal and spatial dynamics of electrically-evoked ocular counter-roll responses provide insight into the level of selectivity that can be achieved with otolith end organ stimulation. Results suggest the new system can achieve aVOR restoration and extend that paradigm to eliciting ocular counter-roll responses with appropriate temporal dynamics. Use of a near bipolar reference electrode is sufficient and possibly necessary to minimize current spread and obtain optimal selectivity. The model output showed a majority of the encoded head tilts bringing the left ear down with occasional eye movements suggesting an encoded tilt in the opposite direction. These results suggest that restoration of the sensation of gravito-inertial acceleration is possible using utricle and saccule stimulation.

Chapter 6 Appendix

6.1 Toward a General Purpose Stimulator: Cochlear Stimulation

The cochlear implant (CI) is one of the most successful neural prostheses, restoring auditory sensation to individuals with profound hearing loss through electrical stimulation of cochlear nerves. Study of cortical representation of CI stimulation is important to help guide the advancement of CI technology. Most commercial cochlear implants use biphasic, charge-balanced pulses delivered in monopolar configuration, which causes wide current spread in the cochlea. Single unit recording in the primary auditory cortex has shown limitations of neural activation by CI stimulation that one would normally see from pure tone acoustic stimuli [142–144].

In order to provide a customizable stimulator for this application and take advantage of the ASIC-NI's high compliance voltage and sixteen channel output, the prosthesis circuitry presented in section 2.4 was adapted for cochlear stimulation. For cochlear stimulation, firmware was customized to deliver multipolar pulses to provide a current steering paradigm for focusing electrical activation [145]. The microcontroller can also be programmed to replicate basic cochlear implant style of continuous interleaved sampling (CIS). The ASIC-NI provides greater ease in producing complex stimulus waveforms to study how current focusing and current steering paradigms may more closely simulate natural auditory processing in CI users. With knowledge of embedded microcontroller code development, the system can be successfully customized for stimulation on many electrodes in traditional (mono- or bipolar) pulse paradigms as well as more complex (multipolar) stimulation to explore current steering capabilities. This customization creates a general purpose stimulator for neural stimulation applications.

6.2 Normal Otolith-Ocular Reflex Model Parameters

	Predicted Value (y)	a	b	c	d	e	RMSE
Static Tilt Model Equation: $y=a*\cos(b*tiltAxis+c)+d$							
Static Tilt Figure 32	Magnitude Ratio	-0.71	1.94	114.5	1.33	n/a	0.81
	Right Eye X-Component	4.77	1.05	158.3	-0.30	n/a	2.06
	Right Eye Y-Component	3.61	1.03	121.5	-0.12	n/a	1.81
	Right Eye Z-Component	-1.62	0.99	100.1	0.01	n/a	2.20
	Left Eye X-Component	-4.39	0.99	26.5	-0.06	n/a	1.98
	Left Eye Y-Component	3.82	1.03	78.5	-0.04	n/a	2.22
	Left Eye Z-Component	1.00	1.14	26.7	0.03	n/a	2.53
Horizontal Plane Translation Model Equation: $y=a*TranslationAmplitude*\cos(b*tiltAxis+c)+d$							
Horizontal Plane Translation Figure 36	Magnitude Ratio	0.36	2.03	77.5	1.41	n/a	0.55
	Right Eye X-Component	0.79	1.01	64.3	0.005	n/a	0.66
	Right Eye Y-Component	0.57	1.0	15.9	0.0003	n/a	0.50
	Right Eye Z-Component	-0.41	0.99	54.6	0.001	n/a	0.61
	Left Eye X-Component	0.68	1.03	110.4	-0.03	n/a	0.58
	Left Eye Y-Component	0.46	1.0	-12.1	0.0	n/a	0.45
	Left Eye Z-Component	0.39	1.01	-69.5	0.008	n/a	0.74

Table 5. Model parameters to predict eye movements from tilt or translation axis. Model output for two different nonlinear mixed effect models created to predict a component of eye movement based on the fixed effect (input) of translation or tilt axis. Equations for each model are listed in the table. The model for the static tilt is detailed in section 3.3.2. The model for horizontal plane translations is detailed in section 3.3.3.

Combined Tilt-Translation Model Equation: $y = (a*\cos(b*TiltAxis+c) +d) + (e*TypeOfStimulus)$									
	Predicted Value (y)	a	b	c	d	e	RMSE	F-stat	P-value
Figure 39 Combined Tilt and Translation Model	Magnitude Ratio	-0.75	1.96	93.0	1.35	-4e-4	0.64	0.01	0.92
	Right Eye X-Component	-0.86	1.08	-20.36	-0.06	-4.2e-5	0.28	8.87e-5	0.99
	Right Eye Y-Component	-0.72	1.04	-77.34	-0.012	0.0003	0.25	0.01	0.94
	Right Eye Z-Component	0.39	1.02	-46.7	0.005	0.0003	0.34	0.03	0.87
	Left Eye X-Component	-0.83	1.01	19.8	-0.01	-3.6e-5	0.28	7.18e-5	0.99
	Left Eye Y-Component	0.75	0.98	92.1	0.003	-2.9e-5	0.23	5.46e-5	0.99
	Left Eye Z-Component	0.32	1.09	27.37	0.02	-3e-4	0.37	0.03	0.86

Table 6. Model parameters to predict axis of tilt/translation based on grouped OORs. Model output for a nonlinear mixed effect model created to predict a component of eye movement based on the fixed effect (input) of translation and tilt axis. The equations for the model is listed at the top of the table. The model is detailed in section 3.3.4.

Fit Parameter	Fixed Effect (independent variable)	Parameter Estimate	Standard Error	tStatistic	pValue
a	(Intercept)	16.74	5.59	3.0	0.003
b	magRatio	-8.91	3.46	-2.57	0.01
c	acosdNRX:sgnRY	0.13	0.034	3.91	1.1e-4
d	acosdNLX:sgnLY	0.74	0.034	21.71	1.6e-71

Table 7. Model parametersto predict tilt axis from binocular eye movements. Model parameters for the linear mixed effect model of the form: $y = a+(b*magRatio)+c*\text{sign}(\text{normRY})*(\arccos(\text{normRX})-180)+d*\text{sign}(\text{normLY})*\arccos(\text{normLX}-180)$, to predict the tilt axis using fixed effects (or input variables) of magRatio=ratio of right/left eye absolute magnitude of ocular counter-roll position , acosdNRX:sgnRY = sign(normalized pitch of right eye)*(arccos(normalized roll of right eye in degrees – 180)), acosdNLX:sgnLY = sign(normalized pitch of left eye) * arccos(normalized roll of left eye in degrees – 180)). Each fit parameter was found to be significant. Model results are plotted in Figure 40 and model creation is discussed in section 3.3.5.

6.3 Animal Data Files Included in Figures

Figure Number	Data Files Used
Figure 30. Normal chinchilla angular VOR.	29A: 20170418_113234_Ch132_Yaw-20dps-1hz-f3.coil 29B: 20170418_113607_Ch132_LARP-20dps-1hz-f9.coil 29C: 20170422_134627_Ch132_RALP-20dps-1hz-f9.coil 29D: All '-velSineFit' files for Yaw, LARP and RALP for the following animals and dates: 20160919-Ch125-normTVOR 20161107-Ch127-normTVOR 20161103-Ch128-normTVOR 20161107-Ch128-normTVOR 20161130-Ch128-normTVOR 20170203-Ch129-normTVOR 20170418-Ch132-normTVOR 20170508-Ch133-normTVOR
Figure 31. Example ocular counter-roll responses recorded during 20° from horizontal tilts.	LED:20161130_142416_Ch128_StaticTilt-Theta180-LED-20deg-40s.coil 150Deg: 20161130_124121_Ch128_StaticTilt-Theta150-20deg-40s.coil 120Deg: 20161130_141253_Ch128_StaticTilt-Theta120-20deg-40s.coil ND: 20161130_142706_Ch128_StaticTilt-Theta90-ND-20deg-40s.coil 60Deg:20161130_141127_Ch128_StaticTilt-Theta60-20deg-40s.coil 30Deg:20161130_141707_Ch128_StaticTilt-Theta30-20deg-40s.coil RED: 20161130_122223_Ch128_StaticTilt-Theta0-RED-20deg-40s.coil
Figure 32. Ocular counter-roll responses recorded from six chinchillas	All Static Tilt Data from follow Chinchillas/Dates: 20160919_Ch125 20161107_Ch127 20161107_Ch128 20161130_Ch128 20170203_Ch129 20170418_Ch132 20170422_Ch132

	20170508_Ch133 20170511_Ch133
Figure 33. Example binocular tVOR position and velocity traces during translations.	20150708_Ch104
Figure 34. Gain and phase of the chinchilla tVOR during lateral and surge translations.	All Lateral and Surge files from these chinchillas on these dates: 20161107-Ch127-normTVOR 20161107-Ch128-normTVOR 20161130-Ch128-normTVOR 20170203-Ch129-normTVOR 20170418-Ch132-normTVOR 20170422-Ch132-normTVOR 20170508-Ch133-normTVOR 20170511-Ch133-normTVOR
Figure 35. Comparison of monkey and chinchilla tVOR frequency response during lateral translation.	All Lateral files from these chinchillas on these dates: 20161107-Ch127-normTVOR 20161107-Ch128-normTVOR 20161130-Ch128-normTVOR 20170203-Ch129-normTVOR 20170418-Ch132-normTVOR 20170422-Ch132-normTVOR 20170508-Ch133-normTVOR 20170511-Ch133-normTVOR And Angelaki Paper Data extracted from Figure 5 of [129]
Figure 36. Translational VOR elicited during translations along axes in the <i>horizontal plane</i> .	All HZ Plane data from: 20160919_Ch125 20161107_Ch127 20161107_Ch128 20161130_Ch128 20170203_Ch129 20170418_Ch132 20170422_Ch132 20170508_Ch133 20170511_Ch133
Figure 37. Translational VOR elicited during translations along axes in the <i>coronal plane</i> .	All Coronal Plane data from: 20160919_Ch125 20161107_Ch127 20161107_Ch128 20161130_Ch128 20170203_Ch129 20170418_Ch132 20170422_Ch132 20170508_Ch133 20170511_Ch133
Figure 38. Translational VOR elicited during translations along axes in the <i>sagittal plane</i> .	All Sagittal Plane data from: 20160919_Ch125 20161107_Ch127

	20161107_Ch128 20161130_Ch128 20170203_Ch129 20170418_Ch132 20170422_Ch132 20170508_Ch133 20170511_Ch133
Figure 39. Comparison of tilt versus translation eye movement data.	HZ Plane Data from same as Figure 36 and Tilt Data from: 20161107_Ch127 20161107_Ch128 20161130_Ch128 20170203_Ch129 20170418_Ch132 20170422_Ch132 20170508_Ch133 20170511_Ch133
Figure 40. Model output to predict tilt axis using binocular eye movement data.	Same as Figure 39
Figure 43. Post-mortem microCT scans for each of the three implanted chinchillas	CT Scans: Ch128: R:\CT\CT Chinch\Ch128\2017-11-02-CT\2017-09-17_23-09-38\ImageJCropToUse\Substack_Ch128.hx Ch132: R:\CT\CT Chinch\Ch132\Substack Ch132 (780-1150).hx Ch133: R:\CT\CT Chinch\Ch133\Ch133_Substack.hx
Figure 44. Electrically-evoked aVOR from three chinchillas.	Ch128 Norm: 20161103-Ch128 20161107-Ch128 20161130-Ch128 Ch128 Stim: 20170121-Ch128 Ch132 Norm:20170418-Ch132 Ch132 Stim: 20170510-Ch132 20170511-Ch132 20170524-Ch132 20170530-Ch132 20170619-Ch132 Ch133 Norm:20170508-Ch133 Ch133 Stim: 20170527-Ch133 20170528-Ch133 20170530-Ch133 20170602-Ch133
Figure 45. Electrically-evoked ocular counter-roll with stimulation of increasing pulse amplitude.	20170628_122258_Ch133_StaticTilt-Utricle-Stim20-Ref15-VaryAmp-50uA.coil 20170628_122410_Ch133_StaticTilt-Utricle-Stim20-Ref15-VaryAmp-75uA.coil

	<p>20170628_122521_Ch133_StaticTilt-Utricle-Stim20-Ref15-VaryAmp-100uA.coil</p> <p>20170628_122632_Ch133_StaticTilt-Utricle-Stim20-Ref15-VaryAmp-125uA.coil</p> <p>20170628_122818_Ch133_StaticTilt-Utricle-Stim20-Ref15-VaryAmp-150uA.coil</p>
Figure 46. Electrically-evoked ocular counter-roll with stimulation of increasing pulse rate.	<p>20170619_112223_Ch133_StaticTilt-Utricle-Stim20-Ref19-VaryRate-50pps.coil</p> <p>20170619_112334_Ch133_StaticTilt-Utricle-Stim20-Ref19-VaryRate-75pps.coil</p> <p>20170619_112446_Ch133_StaticTilt-Utricle-Stim20-Ref19-VaryRate-100pps.coil</p> <p>20170619_112557_Ch133_StaticTilt-Utricle-Stim20-Ref19-VaryRate-150pps.coil</p> <p>20170619_112708_Ch133_StaticTilt-Utricle-Stim20-Ref19-VaryRate-175pps.coil</p> <p>20170619_112819_Ch133_StaticTilt-Utricle-Stim20-Ref19-VaryRate-200pps.coil</p> <p>20170619_112930_Ch133_StaticTilt-Utricle-Stim20-Ref19-VaryRate-250pps.coil</p> <p>20170619_113042_Ch133_StaticTilt-Utricle-Stim20-Ref19-VaryRate-300pps.coil</p>
Figure 47. Electrically-evoked ocular counter-roll using different reference electrodes.	<p>A 20170527_175406_Ch133_Static Baseline-LH-Stim28-Ref51-VaryRef-300pps.coil</p> <p>B 20170511_162106_Ch132_Static Baseline-LH-Stim28-Ref51-VaryRef-300pps.coil</p> <p>C 20161213_125324_Ch128_StaticBaseline-LH-Stim28-Ref52-TiltVaryPulseRate-200pps.coil</p> <p>D 20170119_131719_Ch128_StaticTilt-Saccule-Stim10-Ref51-VaryRef-300pps.coil</p> <p>E 20170119_131827_Ch128_StaticTilt-Saccule-Stim10-Ref52-VaryRef-300pps.coil</p> <p>F 20170119_131938_Ch128_StaticTilt-Saccule-Stim10-Ref5-VaryRef-300pps.coil</p> <p>G 20170502_134938_Ch132_StaticTilt-Utricle-Stim22-Ref26-VaryRef-300pps.coil</p>
Figure 48. Analysis of electrically-evoked ocular counter roll rise time grouped by reference type.	All Virtual Tilt (or constant rate pulse train) Files from:
Figure 49. All results from utricle and saccule pulse train stimulation for the three chinchillas.	<p>20161214-Ch128</p> <p>20161216-Ch128</p> <p>20170117-Ch128</p> <p>20170119-Ch128</p>

<p>Figure 51. Model output to infer electrically-encoded tilt axis from electrically-evoked eye movements.</p>	<p>20170504-Ch132 20170505-Ch132 20170508-Ch132 20170510-Ch132 20170511-Ch132 20170523-Ch132 20170530-Ch132 20170619-Ch132 20170705-Ch132</p> <p>20170527-Ch133 20170528-Ch133 20170530-Ch133 20170601-Ch133 20170602-Ch133 20170616-Ch133</p>
--	---

Table 8. Data files used for creation of figures with chinchilla data.

Chapter 7 References

- [1] Ward, B. K., Agrawal, Y., Hoffman, H. J., Carey, J. P., and Santina, C. C. Della, 2013, "Prevalence and Impact of Bilateral Vestibular Hypofunction: Results From the 2008 US National Health Interview Survey," *JAMA Otolaryngol. Neck Surg.*, **139**(8), pp. 803–810.
- [2] Sun, D. Q., Ward, B. K., Semenov, Y. R., Carey, J. P., and Della Santina, C. C., 2014, "Bilateral vestibular deficiency: quality of life and economic implications," *JAMA Otolaryngol. Head Neck Surg.*, **140**(6), pp. 527–34.
- [3] Carey, J. P., and Della Santina, C., 2005, "Principles of Applied Vestibular Physiology," *Cummings Otolaryngology-Head & Neck Surgery*, Mosby, Philadelphia, pp. 3115–3159.
- [4] Goldberg, J. M., Wilson, V. J., Cullen, K. E., Angelaki, D. E., Broussard, D. M., Buttner-Ennever, J., Fukushima, K., and Minor, L. B., 2012, "Physiology of the Vestibular Organs," *The Vestibular System: A Sixth Sense*, pp. 70–115.
- [5] Goldberg, J. M., Desmadryl, G., Baird, R. a, and Fernández, C., 1990, "The vestibular nerve of the chinchilla. IV. Discharge properties of utricular afferents.," *J. Neurophysiol.*, **63**(4), pp. 781–790.
- [6] Tabak, S., and Collewijn, H., 1994, "Human vestibulo-ocular responses to rapid , helmet-driven head movements," *Exp. Brain Res.*, **102**, pp. 367–378.
- [7] Goldberg, J. M., Wilson, V. J., Cullen, K. E., Angelaki, D. E., Broussard, D. M., Buttner-Ennever, J., Fukushima, K., and Minor, L. B., 2012, "The VOR," *The Vestibular System: A Sixth Sense*, pp. 249–278.
- [8] Guinand, N., Boselie, F., Guyot, J. P., and Kingma, H., 2012, "Quality of Life of Patients With Bilateral Vestibulopathy," *Ann. Otol. Rhinol. Laryngol.*, **121**(7), pp. 471–477.
- [9] Grunbauer, W. M., Dieterich, M., and Brandt, T., 1998, "Bilateral vestibular failure impairs visual motion perception even with the head still," *Neuroreport*, **9**(8), pp. 1807–1810.
- [10] Hegeman, J., Honegger, F., Kupper, M., and Allum, J. H. J., 2005, "The balance control of bilateral peripheral vestibular loss subjects and its improvement with auditory prosthetic feedback," *J. Vestib. Res.*, **15**(2), pp. 109–117.
- [11] Basta, D., Singbartl, F., Todt, I., Clarke, A., and Ernst, A., 2008, "Vestibular rehabilitation by auditory feedback in otolith disorders," *Gait Posture*, **28**(3), pp. 397–404.
- [12] Wall III, C., Oddsson, L. E., Horak, F. B., Wrisley, D. W., and Dozza, M., 2004, "Applications of vibrotactile display of body tilt for rehabilitation," *Annu. Int. Conf. IEEE Eng. Med. Biol. - Proc.*, **26 VII**, pp. 4763–4765.
- [13] Wall, C., and Kentala, E., 2005, "Control of sway using vibrotactile feedback of body tilt in patients with moderate and severe postural control deficits.," *J. Vestib. Res.*, **15**(5–6), pp. 313–325.

- [14] Tyler, M., Danilov, Y., and Bach-Y-Rita, P., 2003, "Closing an Open-Loop Control System: Vestibular Substitution through the Tongue," *J. Integr. Neurosci.*, **2**(2), p. 159.
- [15] Danilov, Y. P., Tyler, M. E., Skinner, K. L., and Bach-y-Rita, P., 2006, "Efficacy of electrotactile vestibular substitution in patients with bilateral vestibular and central balance loss," *Annu. Int. Conf. IEEE Eng. Med. Biol. - Proc.*, **17**, pp. 6605–6609.
- [16] Leigh, R. J., and Zee, D. S., 2006, *The Neurology of Eye Movements*, Oxford University Press.
- [17] Cohen, B., and Suzuki, J. I., 1963, "Eye Movements Induced by Ampullary Nerve Stimulation," *Am J Physiol*, **204**(2), pp. 347–351.
- [18] Cohen, B., Suzuki, J. I., and Bender, M. B., 1964, "Eye Movements from Semicircular Canal Nerve Stimulation in the Cat," *Ann. Otol. Rhinol. Laryngol.*, **73**(1), pp. 153–169.
- [19] Suzuki, J. I., Goto, K., Tokumasu, K., and Cohen, B., 1969, "Implantation of Electrodes near Individual Vestibular Nerve Branches in Mammals," *Ann. Otol. Rhinol. Laryngol.*, **78**(4), pp. 815–826.
- [20] Suzuki, J. I., and Cohen, B., 1964, "Head, Eye, Body and Limb Movements From Semicircular Canal Nerves.," *Exp. Neurol.*, **10**(5), pp. 393–405.
- [21] Suzuki, J. I., Cohen, B., and Bender, M. B., 1964, "Compensatory Eye Movements Induced By Vertical Semicircular Canal Stimulation.," *Exp. Neurol.*, **9**(2), pp. 137–160.
- [22] Fridman, G. Y., Davidovics, N. S., Dai, C., Migliaccio, A. A., and Della Santina, C. C., 2010, "Vestibulo-ocular reflex responses to a multichannel vestibular prosthesis incorporating a 3D coordinate transformation for correction of misalignment.," *JARO*, **11**(3), pp. 367–81.
- [23] Gong, W., and Merfeld, D. M., 2000, "Prototype Neural Semicircular Canal Prosthesis using Patterned Electrical Stimulation," *Ann. Biomed. Eng.*, **28**(5), pp. 572–581.
- [24] Gong, W., and Merfeld, D. M., 2002, "System design and performance of a unilateral horizontal semicircular canal prosthesis," *IEEE Trans. Biomed. Eng.*, **49**(2), pp. 175–181.
- [25] Gong, W., Haburcakova, C., and Merfeld, D. M., 2008, "Vestibulo-Ocular Responses Evoked Via Bilateral Electrical Stimulation of the Lateral Semicircular Canals," *IEEE Trans. Biomed. Eng.*, **55**(11), pp. 2608–2619.
- [26] Lewis, R. F., Haburcakova, C., Gong, W., Lee, D., and Merfeld, D., 2013, "Electrical Stimulation of Semicircular Canal Afferents Affects the Perception of Head Orientation," *J. Neurosci.*, **33**(22), pp. 9530–9535.
- [27] Haburcakova, C., Lewis, R. F., and Merfeld, D. M., 2012, "Frequency dependence of vestibuloocular reflex thresholds," *J. Neurophysiol.*, **107**, pp. 973–983.
- [28] Merfeld, D. M., and Lewis, R. F., 2012, "Replacing semicircular canal function with a

- vestibular implant,” *Otolaryngol. Head Neck Surg.*, **20**(5), pp. 386–392.
- [29] Della Santina, C. C., Migliaccio, A., and Patel, A. H., 2007, “A multichannel semicircular canal neural prosthesis using electrical stimulation to restore 3-D vestibular sensation,” *IEEE Trans. Biomed. Eng.*, **54**(6 Pt 1), pp. 1016–30.
- [30] Dai, C., Fridman, G. Y., Chiang, B., Davidovics, N. S., Melvin, T.-A., Cullen, K. E., and Della Santina, C. C., 2011, “Cross-axis adaptation improves 3D vestibulo-ocular reflex alignment during chronic stimulation via a head-mounted multichannel vestibular prosthesis,” *Exp. Brain Res.*, **210**(3–4), pp. 595–606.
- [31] Dai, C., Fridman, G. Y., Davidovics, N. S., Chiang, B., Ahn, J. H., and Della Santina, C. C., 2011, “Restoration of 3D vestibular sensation in rhesus monkeys using a multichannel vestibular prosthesis,” *Pathol. Inn. Ear*, **281**(1–2), pp. 74–83.
- [32] Chiang, B., Fridman, G. Y., Chenkai, D., Rahman, M. A., and Della Santina, C. C., 2011, “Design and performance of a multichannel vestibular prosthesis that restores semicircular canal sensation in rhesus monkey,” *IEEE Trans. Neural Syst. Rehabil. Eng.*, **19**(5), pp. 588–598.
- [33] Dai, C., Fridman, G. Y., Chiang, B., Rahman, M. A., Ahn, J. H., Davidovics, N. S., and Della Santina, C. C., 2013, “Directional plasticity rapidly improves 3D vestibulo-ocular reflex alignment in monkeys using a multichannel vestibular prosthesis,” *JARO*, **14**(6), pp. 863–77.
- [34] Dai, C., Fridman, G. Y., and Della Santina, C. C., 2011, “Effects of vestibular prosthesis electrode implantation and stimulation on hearing in rhesus monkeys,” *Hear. Res.*, **277**(1–2), pp. 204–210.
- [35] Phillips, J. O., Shepherd, S. J., Nowack, A. L., Ling, L., Bierer, S. M., Kaneko, C. R. S., Phillips, C. M. T., Nie, K., and Rubinstein, J. T., 2012, “Longitudinal performance of a vestibular prosthesis as assessed by electrically evoked compound action potential recording,” *Conf. Proc. ... Annu. Int. Conf. IEEE Eng. Med. Biol. Soc.*, **2012**, pp. 6128–31.
- [36] van de Berg, R., Guinand, N., Nguyen, T. a. K., Ranieri, M., Cavuscens, S., Guyot, J.-P., Stokroos, R., Kingma, H., and Perez-Fornos, A., 2015, “The vestibular implant: frequency-dependency of the electrically evoked vestibulo-ocular reflex in humans,” *Front. Syst. Neurosci.*, **8**, pp. 1–12.
- [37] Boutros, P. J., Rahman, M., Valentin, N. S., Schoo, D., Tan, G., Gimmon, Y., Chow, M., Hofner, A., Morillo, A., Marx, A., Deas, R., Marzo, A. De, Rodriguez, F., Strasser, S., Fridman, G. Y., Dai, C., Ward, B., Schubert, M., Bowditch, S., Jaeger, A., Carey, J. P., and Della Santina, C. C., “Continuous Restoration of the Human Vestibulo-Ocular Reflex via a Multichannel Vestibular Implant,” 2017 Neuromodulation Symp. Abstr. MNS-240. Minneapolis, MN, April 2017.
- [38] Migliaccio, A. a, Minor, L. B., and Della Santina, C. C., 2010, “Adaptation of the vestibulo-ocular reflex for forward-eyed foveate vision,” *J. Physiol.*, **588**(Pt 20), pp. 3855–3867.

- [39] Baird, R. A., Desmadryl, G., Fernández, C., and Goldberg, J. M., 1988, “The vestibular nerve of the chinchilla. II. Relation between afferent response properties and peripheral innervation patterns in the semicircular canals.,” *J. Neurophysiol.*, **60**(1), pp. 182–203.
- [40] Sadeghi, S. G., Minor, L. B., and Cullen, K. E., 2007, “Response of vestibular-nerve afferents to active and passive rotations under normal conditions and after unilateral labyrinthectomy.,” *J. Neurophysiol.*, **97**(2), pp. 1503–14.
- [41] Davidovics, N. S., Fridman, G. Y., Chiang, B., and Della Santina, C. C., 2011, “Effects of biphasic current pulse frequency, amplitude, duration, and interphase gap on eye movement responses to prosthetic electrical stimulation of the vestibular nerve.,” *IEEE Trans. Neural Syst. Rehabil. Eng.*, **19**(1), pp. 84–94.
- [42] Davidovics, N. S., Fridman, G. Y., and Della Santina, C. C., 2012, “Co-modulation of stimulus rate and current from elevated baselines expands head motion encoding range of the vestibular prosthesis.,” *Exp. Brain Res.*, **218**(3), pp. 389–400.
- [43] Sun, D. Q., Rahman, M. A., Fridman, G., Chenkai, D., Chiang, B., and Della Santina, C. C., 2011, “Chronic stimulation of the semicircular canals using a multichannel vestibular prosthesis: Effects on locomotion and angular vestibulo-ocular reflex in chinchillas,” *Engineering in Medicine and Biology Society*, pp. 3519–3523.
- [44] Davidovics, N. S., Rahman, M. a, Dai, C., Ahn, J., Fridman, G. Y., and Della Santina, C. C., 2013, “Multichannel vestibular prosthesis employing modulation of pulse rate and current with alignment precompensation elicits improved VOR performance in monkeys.,” *JARO*, **14**(2), pp. 233–48.
- [45] Valentin, N. S., Hageman, K. N., Dai, C., Santina, C. C. Della, and Fridman, G. Y., 2013, “Development of a Multichannel Vestibular Prosthesis Prototype by Modification of a Commercially Available Cochlear Implant,” *IEEE Trans. Neural Syst. Rehabil. Eng.*, **21**(5), pp. 830–839.
- [46] ClinicalTrials.gov, 2017, “Multichannel Vestibular Implant Early Feasibility Study,” *ClinicalTrials.gov* [Online]. Available: <https://clinicaltrials.gov/ct2/show/NCT02725463>.
- [47] Guyot, J.-P., Sigrist, A., Pelizzone, M., Feigl, G. C., and Kos, M. I., 2011, “Eye movements in response to electrical stimulation of the lateral and superior ampullary nerves,” *Ann. Otol. Rhinol. Laryngol.*, **120**(2), pp. 81–7.
- [48] Wall III, C., Kos, M. I., and Guyot, J.-P., 2007, “Eye movements in response to electric stimulation of the human posterior ampullary nerve.,” *Ann. Otol. Rhinol. Laryngol.*, **116**(5), pp. 369–74.
- [49] Suzuki, J. I., Tokumasu, K., and Goto, K., 1969, “Eye Movements from Single Utricular Nerve Stimulation in the Cat,” *Acta Otolaryngol.*, **68**, pp. 350–362.
- [50] Goto, F., Meng, H., Bai, R., Sato, H., Imagawa, M., Sasaki, M., and Uchino, Y., 2003, “Eye movements evoked by the selective stimulation of the utricular nerve in cats,” *Auris Nasus Larynx*, **30**, pp. 341–348.

- [51] Goto, F., Meng, H., Bai, R., Sato, H., Imagawa, M., Sasaki, M., and Uchino, Y., 2004, "Eye movements evoked by selective saccular nerve stimulation in cats," *Auris Nasus Larynx*, **31**, pp. 220–225.
- [52] Fluor, E., and Mellström, A., 1970, "Utriclar Stimulation and Oculomotor Reactions," *Laryngoscope*, **80**(11), pp. 1702–1711.
- [53] Fluor, E., and Mellström, A., 1970, "Saccular Stimulation and Oculomotor Reactions," *Laryngoscope*, **80**(11), pp. 1713–1721.
- [54] Fluor, E., and Mellström, A., 1971, "The otolith organs and their influence on oculomotor movements," *Exp. Neurol.*, **30**, pp. 139–147.
- [55] Curthoys, I. S., 1987, "Eye Movements Produced by Utriclar and Saccular Stimulation," *Aviat. Space. Environ. Med.*, **58**(9), pp. 192–197.
- [56] Ramos de Miguel, A., Gonzalez, J. C. F., and Macias, A. R., 2017, "Vestibular Response to Electrical Stimulation of the Otolith Organs. Implications in the Development of A Vestibular Implant for the Improvement of the Sensation of Gravitoinertial Accelerations," *J. Int. Adv. Otol.*, **13**(2), pp. 154–161.
- [57] Robinson, D. A., 1963, "A method of measuring eye movement using a scleral search coil in a magnetic field," *Ieee Trans. Biomed. Eng.*, **10**, pp. 137–145.
- [58] Mowrer, O. H., Ruch, T. C., and Miller, N. E., 1935, "The Corneo-Retinal Potential Difference as the Basis of the Galvanometric Method of Recording Eye Movements," *Am. J. Physiol. Content*, **114**(2), pp. 423–428.
- [59] Yee, R. D., Schiller, V. L., Lim, V., Baloh, F. G., Baloh, R. W., and Honrubia, V., 1985, "Velocities of Vertical Saccades with Different Eye Movement Recording Methods," *Invest. Ophthalmol. Vis. Sci.*, **26**, pp. 938–944.
- [60] Young, L. R., and Sheena, D., 1975, "Survey of eye movement recording methods," *Behav. Res. Methods Instrum.*, **7**(5), pp. 397–429.
- [61] Cornsweet, T. N., and Crane, H. D., 1973, "Accurate two-dimensional eye tracker using first and fourth Purkinje images," *J. Opt. Soc. Am.*, **63**(8), pp. 921–928.
- [62] Moore, S. T., Curthoys, I. S., and McCoy, S. G., 1991, "VTM - an image-processing system for measuring ocular torsion," *Comput. Methods Programs Biomed.*, **35**, pp. 219–230.
- [63] Stahl, J. S., Alphen, A. M. Van, and Zeeuw, C. I. De, 2000, "A comparison of video and magnetic search coil recordings of mouse eye movements," *J. Neurosci. Methods*, **99**, pp. 101–110.
- [64] Geest, J. N. Van Der, and Frens, M. A., 2002, "Recording eye movements with video-oculography and scleral search coils: a direct comparison of two methods," *J. Neurosci. Methods*, **114**, pp. 185–195.

- [65] Sakatani, T., and Isa, T., 2004, "PC-based high-speed video-oculography for measuring rapid eye movements in mice," *Neurosci. Res.*, **49**, pp. 123–131.
- [66] Migliaccio, A. A., Macdougall, H. G., Minor, L. B., and Della, C. C., 2005, "Inexpensive system for real-time 3-dimensional video-oculography using a fluorescent marker array," *J. Neurosci. Methods*, **143**, pp. 141–150.
- [67] Weber, K. P., Macdougall, H. G., Halmagyi, G. M., and Curthoys, I. S., 2009, "Impulsive Testing of Semicircular-Canal Function Using Video-oculography," *Ann. N. Y. Acad. Sci.*, **1164**, pp. 486–491.
- [68] Macdougall, H. G., Kiderman, A. D., Schroeder, J. H., Joos, T. C., Wuyts, F. L., and Moore, S. T., 2010, "Portable video oculography system."
- [69] Ong, J. K. Y., and Haslwanter, T., 2010, "Measuring torsional eye movements by tracking stable iris features," *J. Neurosci. Methods*, **192**(2), pp. 261–267.
- [70] van Alphen, B., Winkelman, B. H. J., and Frens, M. A., 2010, "Three-dimensional optokinetic eye movements in the C57BL/6J mouse," *Investig. Ophthalmol. Vis. Sci.*, **51**(1), pp. 623–630.
- [71] Kim, J., 2004, "A simple pupil-independent method for recording eye movements in rodents using video," *J. Neurosci. Methods*, **138**, pp. 165–171.
- [72] Collewijn, H., van der Mark, F., and Jansen, T. C., 1975, "Precise recording of human eye movements," *Vision Res.*, **15**, pp. 447–450.
- [73] Remmel, R. S., 1984, "An inexpensive eye movement monitor using the scleral search coil technique," *IEEE Trans. Biomed. Eng.*, **31**(4), pp. 388–390.
- [74] Kasper, H. J., Hess, B., and Dieringer, N., 1987, "A precise and inexpensive magnetic field search coil system for measuring eye and head movements in small laboratory animals," *J. Neurosci. Methods*, **19**, pp. 115–124.
- [75] "Primelec: Eye Tracking System CS681" [Online]. Available: <http://www.primelec.ch/cs681/cs681.htm>.
- [76] Kaneko, C. R. S., Rosenfeld, S., Fontaine, E., Markov, A., Phillips, J. O., and Yarno, J., 2010, "A preformed scleral search coil for measuring mouse eye movements," *J. Neurosci. Methods*, **193**(1), pp. 126–131.
- [77] Dickman, J. D., and Angelaki, D. E., 1999, "Three-dimensional organization of vestibular-related eye movements to off-vertical axis rotation and linear translation in pigeons," *Exp. Brain Res.*, **129**, pp. 391–400.
- [78] Angelaki, D. E., McHenry, M. Q., Dickman, J. D., and Perachio, A. A., 2000, "Primate translational vestibuloocular reflexes. III. Effects of bilateral labyrinthine electrical stimulation," *J. Neurophysiol.*, **83**, pp. 1662–1676.

- [79] Hess, B. J., and Dieringer, N., 1991, "Spatial organization of linear vestibuloocular reflexes of the rat: responses during horizontal and vertical linear acceleration.," *J. Neurophysiol.*, **66**(6), pp. 1805–1818.
- [80] Baarsma, E. A., and Collewyn, H., 1975, "Eye Movements Due to Linear Accelerations in the Rabbit," *J. Physiol.*, **245**, pp. 227–247.
- [81] Fuchs, A. F., and Robinson, D. A., 1966, "A method for measuring horizontal and vertical eye movement chronically in the monkey.," *J. Appl. Physiol.*, **21**(3), pp. 1068–1070.
- [82] Correia, M. J., Perachio, A. A., and Eden, A. R., 1985, "The monkey vertical vestibuloocular response: a frequency domain study.," *J. Neurophysiol.*, **54**(3), pp. 532–548.
- [83] Newlands, S. D., Ling, L., Phillips, J. O., Siebold, C., Duckert, L., and Fuchs, A. F., 1999, "Short- and long-term consequences of canal plugging on gaze shifts in the rhesus monkey. I. Effects on gaze stabilization.," *J. Neurophysiol.*, **81**(5), pp. 2119–2130.
- [84] Haslwanter, T., 1995, "Mathematics of three-dimensional eye rotations.," *Vision Res.*, **35**(12), pp. 1727–39.
- [85] Migliaccio, A. A., and Todd, M. J., 1999, "Real-time rotation vectors," *Australas. Phys. Eng. Sci. Med.*, **22**(2), pp. 73–80.
- [86] Kasper, H. J., Hess, B., and Dieringer, N., 1975, "Velocities of Vertical Saccades with Different Eye Movement Recording Methods," *J. Neurosci. Methods*, **26**(2), pp. 938–944.
- [87] Straumann, D., Zee, D. S., Solomon, D., Lasker, A. G., and Roberts, D. C., 1995, "Transient torsion during and after saccades," *Vision Res.*, **35**(23/24), pp. 3321–3334.
- [88] Eibenberger, K., Eibenberger, B., and Rucci, M., 2016, "Design , Simulation and Evaluation of Uniform Magnetic Field Systems for Head-Free Eye Movement Recordings with Scleral Search Coils," *Eng. Med. Biol. Soc. 2016 IEEE 38th Annu. Int. Conf.*, pp. 247–250.
- [89] Angelaki, D. E., and Hess, B. J., 1996, "Three-dimensional organization of otolith-ocular reflexes in rhesus monkeys. II. Inertial detection of angular velocity.," *J. Neurophysiol.*, **75**(6), pp. 2425–40.
- [90] Angelaki, D. E., and Hess, B. J., 1996, "Three-dimensional organization of otolith-ocular reflexes in rhesus monkeys. I. Linear acceleration responses during off-vertical axis rotation.," *J. Neurophysiol.*, **75**(6), pp. 2405–2424.
- [91] Furman, J. M., Schor, R. H., and Schumann, T. L., 1992, "Off-vertical axis rotation: a test of the otolith-ocular reflex," *Ann. Otol. Rhinol. Laryngol.*, **101**(8), pp. 643–650.
- [92] Darlot, C., Denise, P., Droulez, J., Cohen, B., and Berthoz, A., 1988, "Eye movements induced by off-vertical axis rotation (OVAR) at small angles of tilt," *Exp. Brain Res.*, **73**, pp. 91–105.

- [93] Merfeld, D. M., 1995, "Modeling human vestibular responses during eccentric rotation and off vertical axis rotation.," *Acta Otolaryngol. Suppl.*, **520 Pt 2**(November), pp. 354–359.
- [94] Hess, B. J., and Angelaki, D. E., 1999, "Oculomotor control of primary eye position discriminates between translation and tilt.," *J. Neurophysiol.*, **81**, pp. 394–398.
- [95] Merrill, D. R., Bikson, M., and Jefferys, J. G. R., 2005, "Electrical stimulation of excitable tissue: Design of efficacious and safe protocols," *J. Neurosci. Methods*, **141**, pp. 171–198.
- [96] Shannon, R. V., 1992, "A Model of Safe Levels for Electrical Stimulation," *IEEE Trans. Biomed. Eng.*, **39**(4), pp. 424–426.
- [97] Robblee, L. S., and Rose, T. L., 1990, "Electrochemical Guidelines for Selection of Protocols and Electrode Materials for Neural Stimulation," *Neural Prostheses: Fundamental Studies*, W.F. Agnew, and D.B. McCreery, eds., Prentice Hall, Englewood Cliffs, NJ, pp. 26–66.
- [98] Hayden, R., Sawyer, S., Frey, E., Mori, S., Migliaccio, A. a, and Della Santina, C. C., 2011, "Virtual labyrinth model of vestibular afferent excitation via implanted electrodes: validation and application to design of a multichannel vestibular prosthesis.," *Exp. Brain Res.*, **210**, pp. 623–40.
- [99] Desai, S. S., Zeh, C., and Lysakowski, A., 2005, "Comparative morphology of rodent vestibular periphery. I. Saccular and Utricular Maculae," *J. Neurophysiol.*, **93**, pp. 251–266.
- [100] Tooker, A., Tolosa, V., Shah, K. G., Sheth, H., Felix, S., Delima, T., and Pannu, S., 2012, "Optimization of multi-layer metal neural probe design," *Proc. Annu. Int. Conf. IEEE Eng. Med. Biol. Soc. EMBS*, pp. 5995–5998.
- [101] Hageman, K. N., Chow, M. R., Boutros, P. J., Roberts, D., Tooker, A., Lee, K., Felix, S., Pannu, S. S., and Della Santina, C. C., 2016, "Design of a Vestibular Prosthesis for Sensation of Gravitoinertial Acceleration," *ASME J. Med. Devices-Transactions*, **10**(3), pp. 10–11.
- [102] Hageman, K. N., Kalayjian, Z. K., Tejada, F., Chiang, B., Rahman, M. A., Fridman, G. Y., Dai, C., Pouliquen, P. O., Georgiou, J., Santina, C. C. Della, and Andreou, A. G., 2016, "A CMOS Neural Interface for a Multichannel Vestibular Prosthesis," *IEEE Trans. Biomed. Circuits Syst.*, **10**(2), pp. 269–79.
- [103] Fridman, G. Y., and Della Santina, C. C., 2012, "Progress Toward Development of a Multichannel Vestibular Prosthesis for Treatment of Bilateral Vestibular Deficiency," *Anat. Rec. Adv. Integr. Anat. Evol. Biol.*, **295**(11), pp. 2010–2029.
- [104] Töreyn, H., and Bhatti, P., 2013, "A field-programmable analog array development platform for vestibular prosthesis signal processing.," *IEEE Trans. Biomed. Circuits Syst.*, **7**(3), pp. 319–25.

- [105] Jiang, D., Demosthenous, A., Perkins, T., and Donaldson, N., 2010, "Stimulation Management for a Multichannel Vestibular Neural Prosthesis," *Control*, pp. 3481–3484.
- [106] Jiang, D., Demosthenous, A., Perkins, T. A., Liu, X., and Donaldson, N., 2011, "A Stimulator ASIC Featuring Versatile Management for Vestibular Prostheses," *IEEE Trans. Biomed. Circuits Syst.*, **5**(2), pp. 147–159.
- [107] Jiang, D., Cirmirakis, D., Demosthenous, A., and Member, S., 2014, "A Vestibular Prosthesis With Highly-Isolated Parallel Multichannel Stimulation," *IEEE Trans. Biomed. Circuits Syst.*, (**IEEEExplor**, pp. 1–14.
- [108] Constandinou, T. G., Georgiou, J., and Toumazou, C., 2009, "A neural implant ASIC for the restoration of balance in individuals with vestibular dysfunction," 2009 IEEE Int. Symp. Circuits Syst., pp. 641–644.
- [109] Della Santina, C. C., Andreou, A. G., Kalayjian, Z., Fridman, G. Y., Chiang, B., and Georgiou, J., 2014, "High-voltage CMOS neuroelectronic interface for a multichannel vestibular prosthesis."
- [110] Cochlear Corporation, 2014, "Cochlear Implants" [Online]. Available: <http://www.cochlear.com/wps/wcm/connect/us/home/treatment-options-for-hearing-loss/cochlear-implants/cochlear-implants>.
- [111] Advanced Bionics, 2013, "HiRes 90K Implant Family" [Online]. Available: http://www.advancedbionics.com/us/en/products/hires_90k_implant.html.
- [112] Med-El, 2014, "Med-El Cochlear Implants" [Online]. Available: <http://www.medel.com/us/cochlear-implants-maestro>.
- [113] Bosch, A., Steyaert, M., and Sansen, W., 2001, "An Accurate Statistical Yield Model for CMOS Current-Steering D/A Converters," *Analog Integr. Circuits Signal Process.*, **29**(3), pp. 173–180.
- [114] Constandinou, T. G., Georgiou, J., and Toumazou, C., 2008, "A Partial-Current-Steering Biphasic Stimulation Driver for Vestibular Prostheses," *Biomed. Circuits Syst. IEEE Trans.*, **2**(2), pp. 106–113.
- [115] Macherey, O., van Wieringen, A., Carlyon, R. P., Deeks, J. M., and Wouters, J., 2006, "Asymmetric pulses in cochlear implants: effects of pulse shape, polarity, and rate," *JARO*, **7**(3), pp. 253–66.
- [116] Migliaccio, A. A., Schubert, M. C., Jiradejvong, P., Lasker, D. M., Clendaniel, R., and Minor, L. B., 2004, "The three-dimensional vestibulo-ocular reflex evoked by high-acceleration rotations in the squirrel monkey," *Exp. Brain Res.*, **159**(4), pp. 443–6.
- [117] Dai, C., Ahn, J., Hageman, K. N., and Della Santina, C., 2014, "Effects of Unilateral Intratympanic Gentamicin on Vestibulo-Ocular Reflex Function in Rhesus Monkeys," ARO Mid-Winter Meeting.

- [118] Merfeld, D. M., Wangsong, G., Morrissey, J., Saginaw, M., Haburcakova, C., and Lewis, R. F., 2006, "Acclimation to Chronic Constant-Rate Peripheral Stimulation Provided by a Vestibular Prosthesis," *IEEE Trans.Biomed.Eng*, **53**(11), pp. 2362–2372.
- [119] Guyot, J. P., Sigrist, A., Pelizzone, M., and Lasker, A. G., 2011, "Adaptation to steady-state electrical stimulation of the vestibular system in humans," *Ann. Otol. Rhinol. Laryngol.*, **120**(3), pp. 143–149.
- [120] Invensense, 2014, "Invensense MPU-9250 Product Specification Sheet" [Online]. Available: <http://store.invensense.com/datasheets/invensense/MPU9250REV1.0.pdf>.
- [121] Ewald, J. R., 1892, "Physiologische Untersuchungen uber das Endorgan des Nervus Octavus," Bergmann, Wiesbaden, Germany.
- [122] Dai, C., Rahman, M., and Della Santina, C., 2013, "Bilateral Stimulation of the Vestibular Labyrinth in Rhesus Monkeys Using a Multichannel Vestibular Prosthesis," ARO Mid-Winter Meeting.
- [123] Ushio, M., Minor, L., Della Santina, C., and Lasker, D., 2011, "Unidirectional rotations produce asymmetric changes in horizontal VOR gain before and after unilateral labyrinthectomy in macaques," *Exp. Brain Res.*, **210**(3–4), pp. 651–660.
- [124] Dai, C., Lasker, D., Ahn, J. H., Rahman, M., Fridman, G., and Della Santina, C., 2012, "Repeated Unidirectional Rotations Reduce Vestibulo-Ocular Reflex Gain Asymmetry in Rhesus Monkeys Using a Unilateral Multichannel Vestibular Prosthesis," ARO Mid-Winter Meeting.
- [125] Fridman, G. Y., and Della Santina, C., 2013, "Safe Direct Current Stimulation to Expand Capabilities of Neural Prostheses," *IEEE Trans. Neural Syst. Rehabil. Eng.*, **21**(2), pp. 319–328.
- [126] Cohen, B., Maruta, J., and Raphan, T., 2001, "Orientation of the eyes to gravito-inertial acceleration.," *Ann. N. Y. Acad. Sci.*, **942**, pp. 241–258.
- [127] Maruta, J., Simpson, J. I., Raphan, T., and Cohen, B., 2001, "Orienting otolith-ocular reflexes in the rabbit during static and dynamic tilts and off-vertical axis rotation," *Vision Res.*, **41**, pp. 3255–3270.
- [128] Oommen, B. S., and Stahl, J. S., 2008, "Eye orientation during static tilts and its relationship to spontaneous head pitch in the laboratory mouse," *Brain Res.*, **1193**, pp. 57–66.
- [129] Angelaki, D. E., 1998, "Three-dimensional organization of otolith-ocular reflexes in rhesus monkeys. III. Responses to translation.," *J. Neurophysiol.*, **80**, pp. 680–695.
- [130] Paige, G. D., and Tomko, D. L., 1991, "Eye movement responses to linear head motion in the squirrel monkey. I. Basic characteristics.," *J. Neurophysiol.*, **65**(5), pp. 1170–1182.
- [131] Haslwanter, T., Straumann, D., Hess, B. J., and Henn, V., 1992, "Static roll and pitch in

- the monkey: shift and rotation of Listing's plane.," *Vision Res.*, **32**(7), pp. 1341–1348.
- [132] Collewijn, H., Van der Steen, J., Ferman, L., and Jansen, T. C., 1985, "Human ocular counterroll: assessment of static and dynamic properties from electromagnetic scleral coil recordings.," *Exp. Brain Res.*, **59**, pp. 185–196.
- [133] Paige, G. D., and Seidman, S. H., 1999, "Characteristics of the VOR in response to linear acceleration.," *Ann. N. Y. Acad. Sci.*, **871**, pp. 123–135.
- [134] Angelaki, D. E., McHenry, M. Q., Dickman, J. D., Newlands, S. D., and Hess, B. J., 1999, "Computation of inertial motion: neural strategies to resolve ambiguous otolith information.," *J. Neurosci.*, **19**(1), pp. 316–327.
- [135] Merfeld, D. M., 2005, "Vestibular Perception and Action Employ Qualitatively Different Mechanisms. II. VOR and Perceptual Responses During Combined Tilt& Translation.," *J. Neurophysiol.*, **94**(1), pp. 199–205.
- [136] Park, S., Gianna-Poulin, C., Black, F. O., Wood, S., and Merfeld, D. M., 2006, "Roll rotation cues influence roll tilt perception assayed using a somatosensory technique.," *J. Neurophysiol.*, **96**(1), pp. 486–491.
- [137] Hullar, T. E., and Williams, C. D., 2006, "Geometry of the semicircular canals of the chinchilla (*Chinchilla laniger*).," *Hear. Res.*, **213**(1–2), pp. 17–24.
- [138] Bolker, B. M., Brooks, M. E., Clark, C. J., Geange, S. W., Poulsen, J. R., Stevens, M. H. H., and White, J. S. S., 2009, "Generalized linear mixed models: a practical guide for ecology and evolution.," *Trends Ecol. Evol.*, **24**(3), pp. 127–135.
- [139] Schwarz, U., Busetini, C., and Miles, F. A., 1989, "Ocular Responses to Linear Motion are Inversely Proportional to Viewing Distance.," *Science* (80-.), **245**(4924), pp. 1394–1396.
- [140] Schwarz, U., and Miles, F. A., 1991, "Ocular Responses to Translation and Their Dependence on Viewing Distance.2. Motion of the Scene.," *J. Neurophysiol.*, **66**(3), pp. 865–878.
- [141] Walls, G., 1942, *The Vertebrate Eye and its Adaptive Radiation*, Hafner Publishing, New York.
- [142] Johnson, L. A., Della Santina, C. C., and Wang, X., 2012, "Temporal bone characterization and cochlear implant feasibility in the common marmoset (*Callithrix jacchus*).," *Hear. Res.*, **290**(1–2), pp. 37–44.
- [143] Johnson, L. A., Della Santina, C. C., and Wang, X., 2016, "Selective Neuronal Activation by Cochlear Implant Stimulation in Auditory Cortex of Awake Primate.," *J. Neurosci.*, **36**(49), pp. 12468–12484.
- [144] Johnson, L. A., Della Santina, C. C., and Wang, X., 2017, "Representations of Time-Varying Cochlear Implant Stimulation in Auditory Cortex of Awake Marmosets (

Callithrix jacchus),” J. Neurosci., **37**(29), pp. 7008–7022.

- [145] Lim, K., Hageman, K., Della Santina, C., and Wang, X., 2017, “Current Focusing Improves Auditory Cortical Responses to Intracochlear Electrical Stimulation in Awake Primates,” 2017 Conf. Implant. Audit. Prosthesis, Lake Tahoe, CA.

Curriculum Vitae

Kristin Nicole Hageman

Born May 11, 1989 in Kalamazoo, MI

Educational History

Ph.D.	2017	Biomedical Engineering	Johns Hopkins School of Medicine
		Mentor: Charles Della Santina, Ph.D., M.D.	
B.S.	2011	Biomedical Engineering	Case Western Reserve University

Other Professional Experience

Research Rotation 7/2011-12/2011

Lab of Dr. Nitish Thakor, Johns Hopkins School of Medicine

Undergraduate Researcher 10/2008-12/2009 and 9/2010-5/2011

Lab of Dr. Dominique Durand, Case Western Reserve University

Cooperative Education 1/2012-8/2010

Medtronic, Cardiac Rhythm Diseases Management Division, Mounds View, MN

Scholarships, fellowships, or other external funding

Case Alumni Association Scholarship (2009-2011)

Case Western Reserve University Presidential Scholarship (2007-2011)

Academic and other honors at Hopkins and elsewhere

April 2017 Neuromodulation Symposium Travel Award, Minneapolis, MN

April 2016 Second Place Poster Award (of ~100) at Neuromodulation Symposium, Minneapolis, MN

Feb 2016 Association for Research in Otolaryngology Mid-Winter Meeting Travel Award

Aug 2012 JHU Medical and Educations Perspectives Medical Design Competition Winner

Jan 2012 JHU Instrumentation Honors Project Competition Winner

Dec 2011 JHU Instrumentation Challenge Project Competition Winner

May 2011 Mark Bernstein Award, Case Western Reserve University

May 2011 J. Thomas Mortimer Cooperative Education Award, Case Western Reserve University

May 2010 Case Western Reserve University BME Scholarship Award

May 2009 Case Western Reserve University Medtronic Undergraduate Award for Distinction in BME

Peer-Reviewed Publications

Hageman, K.N., Chow, M.R., Boutros, P.J., Roberts, D., Tooker, A., Lee, K., Felix, S., Pannu, S.S., Della Santina, C. C. (2016) Design of a Vestibular Prosthesis for Sensation of Gravitoinertial Acceleration. *ASME Journal of Medical Devices*, vol.10, no.3.

Boutros, P.J., Valentin, N., **Hageman, K.N.**, Roberts, D., Dai, C., Della Santina, C.C. (2016) Temporal Discretization Errors Produce Minimal Effects on Vestibular Prosthesis Performance. *ASME Journal of Medical Devices*, vol.10, no.3.

Hageman, K.N.*, Kalayjian, Z.K.*, Tejada, F., Chiang, B., Rahman, M.A., Fridman, G.Y., Dai, C., Pouliquen, P., Georgiou, J., Della Santina, C.C., Andreou, A.G. (2016) A CMOS Neural Interface for a Multichannel Vestibular Prosthesis. *Biomedical Circuits and Systems, IEEE Transactions on*, vol.10, no.2, pp.269-79. (*co-first authorship)

Valentin, N.S., **Hageman, K.N.**, Dai C., Della Santina, C.C., Fridman, G.Y. (2013) Development of a Multichannel Vestibular Prosthesis Prototype by Modification of a Commercially Available Cochlear Implant. *Neural Systems and Rehabilitation Engineering, IEEE Transactions on*, vol.21, no.5, pp.830-9.

Presentations

Hageman, K.N. "Progress Toward a Vestibular Prosthesis to Restore Sensation of Gravitoinertial Acceleration." Med-El, Innsbruck, Austria, *Invited Speaker*, June 2017.

Hageman, K.N. "Progress Toward a Vestibular Prosthesis with Utricle and Saccule Stimulation." Johns Hopkins Center for Hearing and Balance Seminar, Baltimore, MD, *Invited Speaker*, June 2015.

Hageman, K.N., Della Santina, C.C. "Restoring the Sixth Sense in 3D: Progress and Challenges Toward a Multichannel Vestibular Prosthesis," BioMEMS Conference, Cleveland, OH, *Invited Speaker*, April 2013.

Posters

Lim, K.Y., **Hageman, K.**, Della Santina, C.C., Wang, X. (2017) Current Focusing Improves Auditory Cortical Responses to Intracochlear Electrical stimulation in Awake Primate. *2017 Conference on Implantable Auditory Prosthesis*, Lake Tahoe, CA, July 2017.

Hageman, K.N., Chow, M.R., Boutros, P.J., Roberts, D., Della Santina, C.C. (2017) Electrically-Evoked Eye Movements using a Vestibular Prosthesis Designed to Restore Sensation of Gravitoinertial Acceleration. *Neuromodulation Symposium 2017*, Minneapolis, MN, April 2017.

Hageman, K.N., Yuen Lim, K., Chow, M.R., Kalayjian, Z.K., Andreou, A.G., Wang, X., Della Santina, C.C. (2016) Versatile Stimulation Circuitry for Neural Applications: Use in Vestibular and Cochlear Stimulation. *North American Neuromodulation Society-Neural Interfaces Conference*, Baltimore, MD, June 2016.

Hageman, K.N., Chow, M.R., Boutros, P.J., Roberts, D., Tooker, A., Lee, K., Felix, S., Pannu, S.S., Della Santina, C.C. (2016) Design of a Vestibular Prosthesis for Sensation of Gravitoinertial Acceleration. *Design of Medical Devices Conference 2016 and Neuromodulation Symposium 2016*, Minneapolis, MN, April 2016.

Boutros, P.J., Valentin, N., **Hageman, K.N.**, Roberts, D., Dai, C., Della Santina, C.C. (2016) Temporal Discretization Errors Produce Minimal Effects on Vestibular Prosthesis Performance. *Design of Medical Devices Conference 2016 and Neuromodulation Symposium 2016*, Minneapolis, MN, April 2016.

Hageman, K.N., Chow, M.R., Roberts, D., Ren, P. Boutros, P.J., Dai, C., Della Santina, C.C. (2016) Characterization of Normal 3D Binocular Chinchilla Otolith-Ocular Reflexes as a Metric to Study Otolith Stimulation using a Multichannel Vestibular Prosthesis. *Association for Research in Otolaryngology Mid-Winter Meeting 2016*, San Diego, CA, February 2016.

Boutros, P.J., Valentin, N., Roberts, D., **Hageman, K.N.**, Dai, C., Della Santina, C.C. (2016) Temporal Discretization Inherent to Continuous Interleaved Sampling Stimulation Causes Negligible Effects on Vestibulo-Ocular Reflex Responses Elicited in Rhesus Monkeys. *Association for Research in Otolaryngology Mid-Winter Meeting 2016*, San Diego, CA, February 2016.

Dai, C., Ahn, J., Ren, P., **Hageman K.N.**, Rahman, M.A., Fridman, G., Della Santina, C.C. (2016) Longitudinal Efficacy and Impedance Change of Vestibular Prosthesis Electrodes. *Association for Research in Otolaryngology Mid-Winter Meeting 2016*, San Diego, CA, February 2016.

Boutros, P., **Hageman, K.N.**, Tooker, A., Lee, K., Felix, S., Dai, C., Pannu, S., Della Santina, C.C. (2015) High Density Micro-machined Polyimide Electrode Arrays for Vestibular Implants. *Association for Research in Otolaryngology Mid-Winter Meeting 2015*, Baltimore, MD, February 2015.

Dai, C., Wang, G., **Hageman, K.N.**, Chiang, C., Della Santina, C. (2015) Monopolar, Bipolar or Tripolar Stimulation Using a MVP in Restoring Vestibular Function in Rhesus. *Association for Research in Otolaryngology Mid-Winter Meeting 2013*, Baltimore, MD, February 2015.

Hageman, K.N., Kalayjian, Z., Rahman M.A., Chiang B., Tejada F., Fridman G.Y., Dai C., Andreou A.G., Della Santina C.C. (2014) System Integration of an Application Specific Integrated Circuit to Advance Toward a Fully Implantable Multichannel Vestibular Prosthesis. *Mid-Atlantic Micro/Nano Alliance Symposium*, Baltimore, MD, March 2014.

Dai, C., Ahn, J., **Hageman, K.N.**, and Della Santina, C.C. (2014) Effects of Unilateral Intratympanic Gentamicin on Vestibulo-Ocular Reflex Function in Rhesus Monkeys. *Association for Research in Otolaryngology Mid-Winter Meeting 2014*, San Diego, CA, February 2014.

Hageman K.N., Kalayjian Z., Rahman M.A., Chiang B., Tejada F., Fridman G.Y., Dai C., Andreou A.G., Della Santina C.C. (2013) System Integration of an Application Specific Integrated Circuit to Advance Toward a Fully Implantable Multichannel Vestibular Prosthesis. *Association for Research in Otolaryngology Mid-Winter Meeting 2013*, Baltimore, MD, February 2013.

Valentin, N.S., Dai, C., **Hageman, K.N.**, Ward, B., Ahn, J., Della Santina, C.C., Fridman, G.Y. (2012) Development of a Prototype Implantable Multichannel Vestibular Prosthesis for Humans via Modification of a Commercially Available Cochlear Implant. *Association for Research in Otolaryngology Mid-Winter Meeting 2012*, San Diego, CA, February 2012.

Service and Leadership

Johns Hopkins University, Graduate Women's Empowerment Network (2014 – 2017)

Executive Board Director (2015 – 2017)

Director of Liaisons (2014 – 2015)

Hampden Family Center Volunteer Math Tutor, Baltimore, MD (Oct 2015 – May 2016)
Johns Hopkins University Teaching Assistant
Freshmen Biomedical Models & Design (Fall 2014)
Graduate Models of the Neuron Course (Fall 2013)
Thread Mentoring Program, Baltimore, MD (Aug 2012 – April 2015)
Awarded Thread Mentoring Family of the Month (Aug 2014)
Awarded Thread Superstar Family of the Year (2013)
Awarded Thread Mentoring Family of the Month for Never Giving Up (March 2013)
Awarded Thread Mentor of the Month Award for Unwavering Humility (Jan 2013)
Case Western Reserve University Biomedical Engineering Career Development Committee
(2011)
Tau Beta Pi, Engineering Honors Society, Case Western Reserve University (2008 – 2011)
Corresponding Secretary (2010-2011)
Engineering Futures Event Chair (2009)
Alpha Eta Mu Beta, Biomedical Engineering Honors Society, Case Western Reserve
University (2009 – 2011)
Vice President (2010 – 2011)
Participant of Case Western Reserve University Emerging Leaders Program (2007 –2008)